

AN ABSTRACT OF THE THESIS OF

Andrew Heath Barnard for the degree of Doctor of Philosophy in Oceanography presented on December 18, 2000. Title: The Inherent Optical Properties of the Oceans: from Closure to Prediction.

Redacted for Privacy

Abstract approved: _____

Timothy J. Cowles

Precise in situ measurement of the spectral absorption and scattering coefficients in several regions has revealed patterns in the distribution of the inherent optical properties on spatial scales that were previously unobtainable. The precision of the measurements was found to be consistent and unbiased across a variety of oceanic regimes and are therefore useful for studies of radiative transfer. The spectral information obtained during this research was used to define fundamental relationships between the inherent optical properties and the apparent optical properties of the ocean.

A multiple band ratio algorithm based on the relationship between the absorption coefficient and the remote sensing reflectance was developed to provide a means to test the optical measurements for closure. A large database of synoptic measurements of the spectral absorption coefficient and the remote sensing reflectance was tested for closure using this algorithm and it was found that

radiative transfer works to within instrument accuracy. Furthermore, it was demonstrated that inversion to obtain the absorption coefficient is possible using this algorithm providing that the spectral dependence of the absorption coefficient can be accurately modeled.

A model based on the horizontal variability in the vertical structure of the backscattering to absorption ratio was developed to predict the amplitude of an internal wave using the spatial information in the remote sensing reflectance. The results from a combined aircraft and in situ measurement experiment showed that the predicted amplitudes of the internal wave were comparable to the depth fluctuations of the thermocline observed in the in situ temperature profiles.

In an effort to aid primary productivity experiments, an empirical model to predict the photosynthetically available radiation light levels from the absorption coefficient profiles at 490 nm was developed based on in situ data collected in the Gulf of California. The model was able to predict the depth of the one percent light level with a standard error of 4 m. This model provides a method to estimate the daytime light levels from nighttime absorption coefficient measurements at 490 nm.

The Inherent Optical Properties of the Oceans: from Closure to Prediction

by

Andrew Heath Barnard

A THESIS

submitted to

Oregon State University

in partial fulfillment of
the requirements for the
degree of

Doctor of Philosophy

Presented December 18, 2000
Commencement June 2001

Doctor of Philosophy thesis of Andrew Heath Barnard presented on December 18,
2000

APPROVED:

Redacted for Privacy

Major Professor, representing Oceanography

Redacted for Privacy

Dean of College of Oceanic and Atmospheric Sciences

Redacted for Privacy

Dean of Graduate School

I understand that my thesis will become part of the permanent collection of Oregon State University libraries. My signature below authorizes release of my thesis to any reader upon request.

Redacted for Privacy

Andrew H. Barnard, Author

ACKNOWLEDGMENTS

I thank Mark Abbott, Jack Barth, Tim Cowles, Jim Mueller, Jim Yoder, and Bruce Rettig for serving as my thesis committee members. Their guidance, patience, and support throughout this process continually strengthened my resolve to finish. Jim Mueller and Jim Yoder deserve extra recognition for spending their time and money to travel to Oregon to serve on my committee. I thank Tim Cowles for his extra time and effort spent in helping to refresh my knowledge of various aspects of oceanography. I am grateful to Irma Delson for all she has done to see me through this process.

The past and present members of the Optical Oceanography Group at Oregon State University deserve recognition for an immeasurable number of reasons. These people include Ron Zaneveld, Scott Pegau, Emmanuel Boss, Mike Twardowski, Sarah Searson, Francios Baratange, Sean Herring, and Kusiel Shifrin. The many spirited discussions over coffee or standing at the chalkboard were instrumental in expanding my knowledge of optical oceanography and in understanding the process of scientific research. I truly feel very fortunate to have been a part of such a productive and collaborative group.

I am indebted to Ron Zaneveld for providing me the opportunity to grow and develop as a research scientist. He has been an exceptional mentor, and above all, my most vocal and active supporter.

I would also like to thank the Bio-Optics Group, including Russ Desiderio, Chris Wingard, Malinda Sutor, and Nathan Potter for keeping my spirits up

throughout this process. Russ was always willing to serve as an excellent sounding board, and provided many useful comments on chapter two of this thesis. Ricardo Letelier and Jasmine Bartlett were always willing to lend me a hand.

I thank the various colleagues outside of Oregon State University who have continually offered their emotional and educational support, including Drs. Collin Roesler, Mary Jane Perry, Alan Weidemann, Barney Balch, Margaret Deksheniaks, Percy Donaghay, and Chuck Trees. I thank Casey Moore for giving me the opportunity to learn more about the engineering aspects of ocean optics.

I thank Lisa Eisner, Sam Laney, Claudia Mengelt for including me in the many study sessions in preparing for the written comprehensive exams, and for frequently letting me vent my frustrations. I thank Dylan and Naara Righi for their continual friendship and cheerful dispositions.

I thank the crew of the Research Vessels Seward Johnson, Knorr, Wecoma, and Melville, who made going to sea enjoyable and productive. I thank the Office of Naval Research Environmental Optics Program and the NASA Ocean Biology/Biogeochemistry Program for providing most of the funding for this research.

Most importantly I thank my wife, Lisal, without whom this thesis would have never been completed. Her patience, love, and willingness to see me through the difficult times were instrumental in completing this thesis. She is the light within me. To her I say thank you. We've finally made it to this journey's end. Your husband has come home.

CONTRIBUTION OF AUTHORS

Drs. J. Ronald Zaneveld and W. Scott Pegau were involved in the analysis and writing of the enclosed chapters. Drs. Emmanuel Boss and Jack Barth provided much of the physical oceanography background information contained in chapter four. Drs. James Mueller and Heidi Sosik contributed some of the radiometric data used in chapters three through five. Dr. Curtiss Davis provided the aircraft imagery and above water reflectance data used in chapter four. Geolocation of the aircraft imagery was contributed by W. Joseph Rhea.

TABLE OF CONTENTS

	<u>Page</u>
1. GENERAL INTRODUCTION	1
1.1 BACKGROUND AND DEFINITIONS	1
1.2 RESEARCH FOCUS	4
2. GLOBAL RELATIONSHIPS OF THE INHERENT OPTICAL PROPERTIES OF THE OCEANS	11
2.1 ABSTRACT	12
2.2 INTRODUCTION	13
2.3 FIELD METHODS AND DATA	16
2.4 RESULTS AND DISCUSSION	21
2.4.1 Chromophoric Dissolved Absorption Coefficient $a_g(\lambda)$	24
2.4.2 Particulate Absorption Coefficient $a_p(\lambda)$	27
2.4.3 Total Absorption Coefficient Without Water $a_{pg}(\lambda)$	34
2.4.4 Particulate Scattering Coefficient $b_p(\lambda)$	40
2.4.5 Beam Attenuation Coefficient $c_{pg}(\lambda)$	43
2.4.6 The CMO97 Data Set: Regional Differences	50
2.5 SUMMARY	53
2.6 REFERENCES	55
3. <i>IN SITU</i> DETERMINATION OF THE REMOTELY SENSED REFLECTANCE AND THE ABSORPTION COEFFICIENT: CLOSURE AND INVERSION	60
3.1 ABSTRACT	61
3.2 INTRODUCTION	61

TABLE OF CONTENTS (Continued)

	<u>Page</u>
3.3	63
THEORY AND APPROACH	
3.3.1 Remote-Sensing Reflectance R_{rs}	63
3.3.2 f/Q Considerations	64
3.3.3 Backscattering Component	66
3.3.4 Closure	71
3.3.5 Inversion	71
3.4	74
DATA AND MEASUREMENTS	
3.4.1 Data Sets	74
3.4.2 Remote-Sensing Reflectance	75
3.4.3 Inherent Optical Properties	76
3.4.4 Optical Weighting of Profiles	76
3.5	78
RESULTS	
3.5.1 <i>In situ</i> Measurement Closure: Constant b_{br3} Case	78
3.5.2 Variable b_{br3} Comparison	80
3.5.3 Inversion to Obtain the Absorption Coefficient	81
3.6	86
DISCUSSION AND CONCLUSIONS	
3.7	89
REFERENCES	
4.	
DETECTION AND CHARACTERIZATION OF INTERNAL WAVES IN A COASTAL ENVIRONMENT FROM HIGH SPATIAL RESOLUTION VISIBLE REMOTE SENSING IMAGERY	93
4.1 ABSTRACT	94
4.2 INTRODUCTION	95
4.3 EXPERIMENTAL SITE AND MEASUREMENTS	99
4.4 INITIAL OBSERVATIONS	102

TABLE OF CONTENTS (Continued)

	<u>Page</u>
4.5 REMOTE SENSING OF INTERNAL WAVES	108
4.6 MODEL PREDICTIONS OF INTERNAL WAVE CHARACTERISTICS	111
4.7 DISCUSSION	118
4.8 SUMMARY	123
4.9 REFERENCES	124
5. THE DETERMINATION OF PAR LEVELS FROM ABSORPTION COEFFICIENT PROFILES AT 490 nm	127
5.1 ABSTRACT	128
5.2 INTRODUCTION	128
5.3 METHODS	130
5.4 SEMI-ANALYTICAL MODEL AND RESULTS	132
5.5 DISCUSSION	146
5.6 REFERENCES	149
6. GENERAL CONCLUSIONS	151
BIBLIOGRAPHY	156

LIST OF FIGURES

<u>Figure</u>	<u>Page</u>
2.1 Dissolved absorption coefficient a_g measured at 488 nm versus the dissolved absorption coefficient measured at the six other wavelengths for the entire global data set.	25
2.2 Same as Figure 2.1, but for the particulate absorption coefficient a_p .	28
2.3 Spectrum of the slopes of the $a_p(\lambda)$ returned from the regressions versus $a_p(488 \text{ nm})$ from the global data set (thick line with asterisks), the lower magnitude data set (solid line with open circles), and the upper magnitude data set (solid line with solid circles) given in Tables 2.4 and 2.5.	31
2.4 Spectrum of the y intercepts of the $a_p(\lambda)$ returned from the regressions versus $a_p(488 \text{ nm})$ from the global data set (thick line with asterisks), the lower magnitude data set (solid line with open circles) and the upper magnitude data set (solid line with solid circles) given in Tables 2.4 and 2.5.	32
2.5 Same as Figure 2.1, but for the total absorption coefficient less water a_{pg} .	35
2.6 Spectrum of the slopes of the $a_{pg}(\lambda)$ returned from the regressions versus $a_{pg}(488 \text{ nm})$ from the global data set (thick line with asterisks), the lower magnitude data set (solid line with open circles), and the upper magnitude data set (solid line with solid circles) given in Tables 2.6 and 2.7.	37
2.7 Dissolved absorption coefficient at 488 nm versus the total absorption coefficient at 488 nm for the lower 86 % magnitude data set (blue) and the upper 14 % magnitude data set (green).	38
2.8 Spectrum of the y intercepts of the $a_{pg}(\lambda)$ returned from the regressions versus $a_{pg}(488 \text{ nm})$ from the global data set (thick line with asterisks), the lower magnitude data set (solid line with open circles), and the upper magnitude data set (solid line with solid circles) given in Tables 2.6 and 2.7.	39

LIST OF FIGURES (Continued)

<u>Figure</u>	<u>Page</u>
2.9 Same as Figure 2.1, but for the particulate scattering coefficient b_p .	41
2.10 Global data set slopes of $b_p(\lambda)$ from the least squares regressions plotted versus wavelength (thick line with asterisks).	42
2.11 Same as Figure 2.1, but for the beam attenuation coefficient less water c_{pg} .	44
2.12 Slopes of $c_{pg}(\lambda)$ returned from the least squares regressions versus $c_{pg}(488 \text{ nm})$ using the full data set (thick line with asterisks).	45
2.13 The y intercepts of $c_{pg}(\lambda)$ from the least squares regressions versus $c_{pg}(488 \text{ nm})$ using the full data set (thick line with asterisks).	46
3.1 Contour of the backscattering triple ratio b_{br3} as a function of the shape of the particle backscattering η and the water-to-particle backscattering ratio at 490 nm (b_{bw}/b_{bp}), computed with Eq. (3.9) and the wavelengths 443, 490, and 555 nm.	69
3.2 Triple ratio of the remote-sensing reflectance at 443, 490, and 555 nm determined from <i>in situ</i> radiometer measurements versus the triple ratio of the absorption coefficient at 443, 490, and 555 nm determined from <i>in situ</i> ac-9 measurements.	79
3.3 Optically weighted absorption coefficient at 490 nm versus the optically weighted absorption coefficient at 443 nm (filled diamonds) and 555 nm (asterisks) determined from ac-9 measurements.	82
3.4 Predicted absorption coefficient at 443 (panel A), 490 (panel B), and 555 nm (panel C) based on the remote-sensing reflectance triple ratio and the absorption relationships at 443 and 555 nm (see Fig. 3.3 and Equation 3.14) versus the <i>in situ</i> measured absorption coefficient at each of the respective wavelengths.	83

LIST OF FIGURES (Continued)

<u>Figure</u>		<u>Page</u>
4.1	Small inset: East Sound, Orcas Island, Washington, located between the Strait of Juan de Fuca and the Strait of Georgia. Main chart: Chart of East Sound with contours of bathymetry (m). The in situ sampling locations conducted on August 11, 1998 are shown as asterisks, labeled as stations A, B, and C. The locations of the bottom moored ADCP's are shown as plus symbols. The area of the aircraft imagery is shown as the rectangle.	100
4.2	The empirically calibrated values of water leaving radiance at the 490 nm (left panel) and the 700 nm (right panel) wavelengths as measured by the PHILLS radiometer over East Sound on August 11, 1998. Note the bright radiance lines that extend eastward, just to the south of the shallow sill in the imagery at the 490 nm wavelength. These bands are not discernable in the water leaving radiance at the 700 nm wavelength. Ships and islands within the sound have been masked as black patches.	103
4.3	Vertical profiles of temperature (left panel), salinity (middle panel), and density anomaly (right panel) in the upper 12 m at stations A (solid line), B (dashed line), and C (dot-dashed line) shown in figure 4.1. The subscripts denote which profile in each series is plotted (see figure 4.4) for stations B and C.	105
4.4	Profiles of temperature at stations B (left panel) and C (right panel) on August 11, 1998. The profiles are numbered in the order in which they were made.	107
4.5	The profiles of the absorption coefficient at 490 nm (left panel) and the backscattering to absorption ratio at 490 nm (right panel) at station B. The numbers indicate the order in which the profiles were made.	109

LIST OF FIGURES (Continued)

<u>Figure</u>	<u>Page</u>	
4.6	Locations of the three transects of the 490 nm water leaving radiance extracted from the aircraft imagery along which the internal wave amplitude was computed (x_2 locations). The x_1 locations for each line are shown as stars, and the x_3 locations are shown as ellipses with crosses. The solid line shows the location of the transect on the western side of the sound, the dashed line shows the location of the transect line in the central portion of the sound, and the location of the easternmost transect is shown as a thick solid line.	114
4.7	The water leaving radiance at 490 nm wavelength (solid lines) versus distance from the x_1 location is shown for the western (top panel), central (middle panel), and eastern (bottom panel) transect lines (see figure 4.6). Also plotted is the change in the depth of the pycnocline relative to the depth at the x_1 location using the model given in the text for each of the three transect lines (dashed line).	116
4.8	The water leaving radiance at 490 nm extracted along the most upstream bright reflecting line, versus distance from the western shore (solid line). Also plotted is the bathymetry along this line (thick line).	122
5.1	Sampling locations in the Gulf of California for the three cruises used in this study.	131
5.2	$\tau_{PAR}(z)$ versus $\tau_E(490, z)$ for the 30 profiles taken in the Gulf of California.	135
5.3a	Percent downwelling irradiance transmittance spectra from the surface to approximately 10 m for 30 profiles taken in the Gulf of California.	136
5.3b	Same as for figure 3a where the irradiance transmittance has been normalized by the 556 nm value.	137
5.4	Total absorption coefficient spectra averaged over the first 10 m for the 30 profiles taken in the Gulf of California.	138

LIST OF FIGURES (Continued)

<u>Figure</u>		<u>Page</u>
5.5	$\tau_E(490, z)$ versus $\tau_a(490, z)$ for the 30 profiles taken in the Gulf of California, with the linear regression shown.	142
5.6	Measured $\tau_{PAR}(z)$ determined from <i>in situ</i> radiance profiles versus the modeled $\tau_{PAR}(z)$ determined from the <i>in situ</i> absorption coefficient at 490 nm profiles for the 30 stations in the Gulf of California (see equations 5.10a and 5.10b), with the linear regression shown.	144
5.7	The 75, 50, 37, 20, 10, 5, 3 and 1 percent PAR light level depths estimated from <i>in situ</i> spectral irradiance profiles versus the corresponding depths estimated from the absorption optical depth model for the 30 profiles in the Gulf of California.	146

LIST OF TABLES

<u>Table</u>	<u>Page</u>
2.1 Global data set description.	20
2.2 Inherent Optical Property ranges within each individual cruise data set at 488 nm.	22
2.3 Regression results of $a_g(\lambda)$ versus $a_g(488 \text{ nm})$ using the entire global data set.	26
2.4 Regression results of $a_p(\lambda)$ versus $a_p(488 \text{ nm})$ using the entire global data set.	29
2.5 Regression results of $a_p(\lambda)$ versus $a_p(488 \text{ nm})$ using the lower and upper magnitude data sets.	30
2.6 Regression results of $a_{pg}(\lambda)$ versus $a_{pg}(488 \text{ nm})$ using the entire global data set.	35
2.7 Regression results of $a_{pg}(\lambda)$ versus $a_{pg}(488 \text{ nm})$ using the lower and upper magnitude data sets.	36
2.8 Regression results of $b_p(\lambda)$ versus $b_p(488 \text{ nm})$ using the entire global data set.	42
2.9 Regression results of $c_{pg}(\lambda)$ versus $c_{pg}(488 \text{ nm})$ using the entire global data set.	44
2.10 Two-way regression results of $c_{pg}(\lambda)$ versus $c_{pg}(488 \text{ nm})$ using $c_{pg}(488 \text{ nm})$ values less than 1.0 m^{-1} only and with the subtraction of the dissolved absorption values.	47
2.11 R^2 values returned from the linear regressions of the CMO97 data set.	51
3.1 Data set locations and dates consisting of 70 IOP and AOP profiles ^a .	75

LIST OF TABLES (Continued)

<u>Table</u>		<u>Page</u>
3.2	Regression results of the <i>in situ</i> measured and modeled absorption coefficients ^a .	84
5.1	Piecewise linear relationship between $\tau_{PAR}(z)$ and $\tau_E(490, z)$ reproduced from Zaneveld <i>et al.</i> (1993) and for the 30 stations taken in the Gulf of California divided into the "clear" and "green" water types defined in the text.	140
5.2	Percent PAR light level using the "clear" and "green" models (see equations 5.10a and 5.10b) from the integrated absorption coefficient at 490 nm profile. Also shown is the standard error using the models to predict the various percent PAR light level depths.	144

THE INHERENT OPTICAL PROPERTIES OF THE OCEANS: FROM CLOSURE TO PREDICTION

CHAPTER 1

GENERAL INTRODUCTION

1.1 BACKGROUND AND INTRODUCTION

A photon of light traveling within an aqueous medium only has two possible fates; it can be absorbed or it can be scattered. Thus to understand how light is propagated within an aqueous medium, we must know the absorption and scattering properties of the water and its dissolved and particulate constituents. Furthermore, we must also understand the spectral dependencies of the absorption and scattering properties of the water and its constituents in order to describe the spectral quality or color of the light. The absorption and scattering properties as a function of wavelength can be parameterized by considering the proportion of radiant flux lost from a beam normal to an infinitesimally thin layer of the medium due to the absorption and scattering processes. The absorption coefficient (a) and scattering coefficient (b) can then be derived by dividing each of these radiant flux losses by the thickness of the thin layer. The attenuation of the beam of radiant flux through the infinitesimally thin layer, called the beam attenuation coefficient

(c), can be derived as the summation of the absorption and scattering coefficients ($a + b = c$). The absorption, scattering, and beam attenuation coefficients are termed inherent optical properties (IOP) as their magnitudes are dependent only on the water and its constituents and not on the geometrical structure of the light field [Preisendorfer, 1976]. The apparent optical properties (AOP), such as radiance and irradiance levels (relative to surface levels), the diffuse attenuation coefficient, and reflectance, are defined as the optical properties that are dependent on the ambient light field.

The connection between the IOP and the AOP is through the equation of radiative transfer, which solves for the radiance distribution as a function of depth when the absorption and scattering properties of the seawater as well as the incident radiance distribution are known. For a plane parallel horizontally stratified medium, with no internal sources or inelastic scattering and a constant input of monochromatic unpolarized radiance, the equation of radiative transfer can be written as:

$$\cos \theta \frac{dL(z, \theta, \phi)}{dz} = -c(z)L(z, \theta, \phi) + \int_{4\pi} \beta(z, \theta, \phi; \theta', \phi') L(z, \theta', \phi') d\omega(\theta', \phi') \quad (1.1)$$

The term on the left-hand side of equation 1.1 describes the change in the radiance $L(z, \theta, \phi)$ with depth (z) along the path specified by the zenith θ , and azimuthal ϕ angles. The net change in radiance is due to the loss of radiance from the path via attenuation of the radiance along the path and the gain in radiance along the path via scattering of light from other directions (θ', ϕ'). The gain of radiance along the

path (θ, ϕ) via scattering from other angles (θ', ϕ') is determined by the volume scattering function $(\beta(z, \theta, \phi; \theta', \phi'))$ and by the radiance distribution. By manipulating equation 1, one can derive various connections between the IOP and the AOP.

Integration of equation 1.1 over all angles (4π)

$$\int_{4\pi} \cos\theta \frac{dL(z, \theta, \phi)}{dz} d\omega = - \int_{4\pi} c(z)L(z, \theta, \phi) d\omega + \int_{4\pi} \int_{4\pi} \beta(z, \theta, \phi; \theta', \phi') L(z, \theta', \phi') d\omega(\theta', \phi') d\omega \quad (1.2)$$

leads to Gershun's equation,

$$\frac{dE(z)}{dz} = -c(z)E_0(z) + b(z)E_0(z) = -a(z)E_0(z) \quad (1.3)$$

where E is the net plane irradiance, E_0 is the scalar irradiance, b is the total scattering coefficient and a is the total absorption coefficient. Dividing equation (1.3) by the net plane irradiance,

$$\frac{1}{E(z)} \frac{dE(z)}{dz} = -a(z) \frac{E_0(z)}{E(z)}$$

and taking

$$\frac{E(z)}{E_0(z)} = \bar{\mu}(z) \text{ and } -\frac{dE(z)}{E(z)dz} = K(z)$$

where $\bar{\mu}$ is the average cosine of the light field and K is the diffuse attenuation coefficient of the irradiance, leads to one of the more common connections between the AOP and the IOP, namely

$$K(z) = \frac{a(z)}{\bar{\mu}(z)}. \quad (1.4)$$

Another commonly used relationship between the IOP and AOP is the irradiance reflectance, $R(\lambda)$, defined as the upwelling irradiance (E_u) normalized by the downwelling irradiance (E_d) just below the surface [Prieendorfer, 1976]. The irradiance reflectance is related to the absorption and backscattering coefficients as defined by

$$R(\lambda) = \frac{E_u(\lambda)}{E_d(\lambda)} = f(\lambda) \frac{b_b(\lambda)}{a(\lambda)} \quad (1.5)$$

where f is the parameter relating irradiance reflectance to the ratio of the backscattering (b_b) and absorption coefficients [Morel, 1974]. However, as ocean color satellites remotely sense the upwelled radiance, this equation has subsequently been modified to look at the ratio of the upwelling radiance to the downwelling irradiance [Gordon et al., 1988]. This is most commonly known as the remote sensing reflectance;

$$R_{rs}(\lambda) = \frac{R(\lambda)}{Q(\lambda)} = \frac{L_u(\lambda)}{E_d(\lambda)} \cong \frac{f(\lambda) b_b(\lambda)}{Q(\lambda) a(\lambda)} \quad (1.6)$$

where Q is the ratio of the upwelling irradiance and the nadir radiance $E_u(\lambda)/L_u(\lambda)$. This thesis focuses on various aspects of the relationships between the IOP and the AOP.

1.2 RESEARCH FOCUS

Morel and Prieur's [1977] concluding sentence of their seminal paper examining the relationship between the irradiance reflectance and the IOP stated:

It would appear that attempts to refine this relationship at the price of tedious calculations of radiative transfer are less needed at present than is an increase in optical and oceanographic research aimed at better understanding the absorption and scattering properties of the materials present in the sea.

Undoubtedly, the field of optical oceanography has made significant advances towards gaining a more detailed understanding of the IOP since this time. This has been due in part to recent technological advancements that have spawned a new generation of instrumentation that can provide rapid, high spectral and spatial resolution optical measurements of the oceans that were previously not possible. However, we owe much of this success to the work of the pioneers of optical oceanography. Most modern questions in optical oceanography can be traced directly back to ideas posed by these pioneers. For example, in his treatise *Hydrologic Optics* [1976], Preisendorfer suggested that the three main avenues to pursue in the field of hydrologic optics were a) to establish the theoretical physical basis of the IOP, b) to establish empirically-based classifications of the natural hydrosols, and c) to develop computational programs to invert the radiometric observations to determine the IOP. Indeed, twenty-four years later, these avenues are still being pursued.

It has only been since 1994 that instrumentation for the in situ measurement of the spectral IOP has become commercially available. Before 1994, studies designed to examine the relationships between the IOP and the AOP were often

tedious, expensive, and limited in their spectral resolution. With the advent of this new instrumentation, the spectral IOP can now be measured on spatial and temporal scales similar to radiometric measurements allowing tests of closure to be performed. Closure is defined as the "simultaneous verification of a mathematical relationship and a set of parameters by means of the independent measurement of the parameters" [Zaneveld, 1994, p. 62]. The direct comparison of the radiometric and IOP measurements through relationships based on radiative transfer (e.g. Equations 1.4 and 1.6) provides a method to assess the performance of the instrumentation. Verification of independent radiometric and IOP measurements of the IOP and the radiometric these models to be tested for closure. The issue of closure of between the IOP and AOP is covered in chapter 3. It has also provided the opportunity to examine the limitations of these models based on the observed distributions of the IOP. Furthermore, forward models to predict the AOP can now be developed without having to make assumptions about the spectral relationships of the IOP.

The IOP data used in chapters two through five were collected using a Western Environmental Technology Laboratory (WET Labs) Inc. absorption and attenuation meter (ac-9). The ac-9 provides simultaneous measurements of the beam attenuation and absorption coefficient at nine wavelengths. The scattering coefficient can then estimated by subtraction ($b = c - a$). When the ac-9 is mounted on a free falling, slow descending physical/optical platform, it can provide approximately 0.1-0.2 m vertical resolution of the IOP. The optical platform and

the calibration, deployment, and post-processing of the ac-9 data are described in more detail in chapter two.

In an effort to take advantage of the rich set of measurements provided by this instrumentation, we incorporated the IOP data collected from a variety of oceanic and coastal regions into a large database. The focus of the work contained in chapter two utilizes this database to examine the spectral variability in the dissolved, particulate and total absorption coefficient, the particulate scattering coefficient, and the total beam attenuation coefficient over a wide variety of ocean regimes. In this analysis we found that there are fundamental, first order spectral relationships in the global distributions of the IOP. The results contained in this chapter provided a set of basis vectors describing the large-scale spectral relationships of the inherent optical properties that can be used in models that require a priori knowledge of the spectral dependencies of the IOP components. A second focus of this work was to show that the in situ measurements of the inherent optical properties made with an ac-9 meter are consistently unbiased when proper calibrations are routinely performed and thus are suitable for studies of radiative transfer.

An important test of the validity of the IOP measurements is through intercomparison with independently measured AOP. Studies such as these provide verification that the measurements are consistent in quantity and scale. Chapter three examines the issue of closure between the derived remote sensing reflectance and the measured absorption coefficient based on the approximation given in

equation (1.6). The goal of this work was to develop a method to test the AOP and IOP measurements for closure that is based on the fewest number of theoretical approximations possible. We developed a model to directly compare the measurements of absorption and remote sensing reflectance that minimizes the dependence of the backscattering coefficient and the angular nature of the underwater light field by using two ratios with three appropriately spaced wavelengths. We demonstrate closure between these disparate measurements and that radiative transfer works to within instrument accuracy.

An interesting outcome of this model development was that it provided a method to invert the remote sensing reflectance spectrum to obtain the spectral absorption coefficients provided the spectral dependencies of the absorption coefficient are known. By using similar linear functionalities of the spectral absorption coefficient as shown in chapter two, we showed that the model's ability to predict the absorption coefficient at 490 nm was more accurate than other empirically based inversion algorithms. As with most empirical or semi-analytical inversion algorithms based on the remotely sensed reflectance, the largest sources of error in the predictability of our model were due to the uncertainties in the spectral dependency of the absorption coefficient. Clearly, much more research on the causes of the spectral variability in the absorption coefficient is needed in order to improve these models.

The effects of horizontal variability in the vertical structure of the IOP on the spatial distribution of the remotely sensed reflectance are examined in chapter

four. The goal of this research was to develop a model that utilizes the spatial information contained in the remotely sensed reflectance imagery to characterize a subsurface physical/optical feature. Using the two-stream radiative transfer model given by *Zaneveld and Pegau* [1998], we showed that the amplitude of an internal wave could be predicted using remote sensing reflectance measurements at three different spatial locations. In contrast to the model developed by *Zaneveld and Pegau*, our model requires no a priori information as to the vertical structure of the backscattering to absorption coefficient ratio provided that the diffuse attenuation coefficient can be estimated from the remotely sensed imagery data.

High spatial resolution visible remote sensing imagery obtained over a shallow water coastal region, showed the appearance of several parallel lines of bright and dark contrast. In situ measurements collected during the period of image acquisition showed that the depth of the thermocline oscillated in the vicinity of these lines of contrast. The depth of the thermocline was correlated to the depth of a sharp optical boundary in the backscattering to absorption coefficient ratio. These vertical variations observed in the in situ observations and the proximity of these lines of contrast in relation to a partial sill suggested that an internal wave was the causal mechanism. We applied the spatial contrast model to the remote sensing imagery data to predict the amplitude of the internal wave. The predicted amplitude of the internal wave compared well with in situ observations. The results of the model demonstrated the utility in using the spatial information of the

remotely sensed imagery to provide a hydrodynamic interpretation of the internal wave spatial patterns.

The work in chapter five focused on developing a model to predict the daytime photosynthetically available radiation (PAR) light levels from a nighttime absorption coefficient profile at 490 nm for use with primary productivity experiments. In this work we examined the relationship between the optical depth of PAR and of the downwelling irradiance at 490 nm obtained during recent research cruises in the Gulf of California. Two water class types were identified in the irradiance transmittance and total absorption spectra, one with high absorption and low irradiance transmittance and one with low absorption and high irradiance transmittance. We chose to use a third-order polynomial model of the optical depth of the downwelling irradiance at 490 nm to predict the optical depth of PAR for each water type. By applying the mean value theorem to Gershun's equation, we derived an absorption optical depth at 490 nm profile that was used to predict the optical depth of irradiance at 490 nm. This relationship was found to be independent of water type and well correlated, demonstrating closure between the measurements. By substitution of these relationships into the third-order polynomial fits of PAR optical depth, we demonstrate that the depth of various PAR irradiance light levels can be predicted from a single profile of the absorption coefficient at 490 nm.

CHAPTER 2

GLOBAL RELATIONSHIPS OF THE INHERENT OPTICAL PROPERTIES OF
THE OCEANS

Andrew H. Barnard, W. Scott Pegau, and J. Ronald V. Zaneveld.

Published in *Journal of Geophysical Research*, 103, 24,955-24,968, October 15,
1998. Copyright by the American Geophysical Union.

2.1 ABSTRACT

We have collected data during eight separate research cruises from open ocean to estuarine oceanic environments. Inherent optical property data collected during these cruises were incorporated into a large database totaling 1914 vertical samples. The range of each inherent optical property within this database spans over two orders of magnitude. Using this database, we examine the spectral relationships of each of the inherent optical properties based on the measurements made at 488 nm. The results of this study show that there are dependencies in the individual inherent optical properties (IOP) spectra that are linearly related. The information from the regression models is used to explain the linear dependencies observed in the global data set. A separate data set collected from a recent cruise is used to compare regional relationships with the global. The implication of this research is that over a diversity of oceanic regimes, there are fundamental, first-order relationships in the individual IOP spectra. These relationships can provide an estimate of the individual IOP spectral relationships when no information about the IOP is available, as is often the case in ocean color remote sensing. More detailed models, however, may be necessary in order to more accurately predict the IOP spectral relationships on regional scales where the expected range of variability is small.

2.2 INTRODUCTION

The inherent optical properties (IOP), defined as those optical properties which are independent of the ambient light field [*Preisendorfer, 1976*], determine the magnitude and spectral signature of the light propagating through the water. The IOP are the absorption, scattering, and beam attenuation properties of the water and its dissolved and suspended materials. The apparent optical properties (AOP), such as radiance and irradiance levels (percent of surface values) and the diffuse attenuation coefficient are connected to the IOP via the equation of radiative transfer. Together with the backscattering coefficient, the absorption coefficient determines the diffuse reflectance of the ocean, which is used for remote sensing purposes. Phytoplankton, detritus, and dissolved matter all have different absorption and scattering characteristics that potentially allow one to infer their concentrations from the remotely sensed spectral radiance.

Various models have been proposed to estimate the IOP based on the AOP [*Prieur and Sathyendranath, 1981; Zaneveld, 1989; Gordon, 1991; Kirk, 1994; Lee et al., 1996*]. However, AOP measurements can only be made during the daylight hours and can be difficult to interpret owing to varying surface conditions, winds, ship reflections, and sky conditions. The AOP are very difficult to measure near the surface, where the influence on the remotely sensed radiance is the largest. Furthermore, discrimination of the particulate and dissolved fractions of the IOP cannot be inferred directly from the measurements of AOP.

The most common technique used to determine the absorption coefficient is by spectrophotometric analysis of filtrates of water samples. The absorption coefficient due to particulate and dissolved material is estimated by analyzing the fraction of the water sample retained on a filter pad (usually 0.2 μm) and the fraction that passes through the filter [Trüper and Yentsch, 1967; Mitchell and Kiefer, 1988a]. Pigment extraction techniques using organic solvents of the filter-pad sample have been used to separate the phytoplankton and detrital portions of the absorption coefficient [Kishino *et al.*, 1985]. While these analyses provide high spectral resolution, they typically only provide data from discrete portions of the water column. Furthermore, the determination of absolute values using these methods is still subject to debate owing to uncertainties caused by the filter and extraction technique [Mitchell and Kiefer, 1988b; Bricaud and Stramski, 1990; Mitchell, 1990].

The beam attenuation coefficient can be used to determine suspended particulate load [Pak *et al.*, 1988]. Most commonly, in situ measurements of the beam attenuation coefficient are made using broadband, single-wavelength transmissometers [Petzold and Austin, 1968; Voss 1992]. While these instruments do provide high vertical resolution estimates of beam attenuation, they are limited in the amount of spectral data they can provide during a single profile.

Recent advances in optical instrumentation have allowed for noninvasive measurement of the spectral absorption and beam attenuation coefficients (WET Labs Inc, ac-9 meter) of the oceans on vertical scales similar to traditional

conductivity-temperature-depth (CTD) measurements [*Moore et al.*, 1992; *Zaneveld et al.*, 1992; *Roesler and Zaneveld*, 1994; *Bricaud et al.*, 1995a]. Over the past 3 years, we have made spectral IOP measurements in six different areas during eight separate research cruises using this instrumentation. Our approach is to incorporate the data collected from these cruises into a large database to examine the spectral variability of each of the IOPs over large time and space scales. This data set is unique in that it contains spectral data on each of the IOP parameters and encompasses a wide variety of oceanic regimes.

It is the purpose of this study to examine the general spectral relationships of the IOP on a global basis. From a descriptive standpoint, this research represents one of the first studies to examine the large-scale distributions of the IOPs, measured simultaneously at various wavelengths. From an analytical standpoint, this research can provide information on the general spectral tendencies in each of the IOPs that span a diversity of oceanic regimes. It is the goal of this research to examine the causes of these spectral tendencies and how can they be used to obtain more information on the IOP variability. As the IOP data was collected during various cruises, a secondary issue to be addressed is the precision of the ac-9 measurements.

We present various models for the spectral relationships of each of the individual IOPs. As we will show, these relationships are quite strong when considering wide ranges of oceanic environments. However, the reader is cautioned that the results presented in this work may not be applicable to all

oceanic scales and environments. In fact, as we will show, these relationships can be quite different on local scales. More detailed models may be necessary in order to more accurately predict the IOP spectral relationships on regional scales. Furthermore, the relationships may change temporally depending on the magnitude of the values owing to differences in the composition of very clear waters compared with turbid waters.

2.3 FIELD METHODS AND DATA

We have assembled the slow descent rate optical platform (SlowDROP) to provide simultaneous hydrographical and optical measurements on vertical scales similar to traditional CTD measurements. The platform is free falling and slightly negatively buoyant, which eliminates the effects of ship motion. A typical instrument configuration on the platform includes two spectral absorption a and beam attenuation c coefficient (ac-9) meters and a CTD. Data from the instruments are integrated into a single stream using a WET Labs, Inc., data acquisition system (MODAPS). Platform descent rates are approximately $10\text{-}30\text{ cm s}^{-1}$, providing better than 10 cm vertical resolution of the water column. Typically, the entire water column (near surface to bottom) is profiled, except in cases where the bottom depth is greater than 150 m due to restrictions imposed by the length of the data cable.

Spectral absorption and beam attenuation coefficient measurements are made using WET Labs, Inc., ac-9 meters at nine wavelengths λ : 412, 440, 488, 510, 532, 555, 650, 676, and 715 nm. For the purpose of this paper, only a brief overview of the ac-9 calibration, deployment, and processing procedures implemented during each field experiment is given. For a detailed description of these procedures, the reader is referred to WET Labs., Inc. (www.wetlabs.com) and to *Twardowski et al.*, [1999]. The ac-9 meters are mounted vertically on the optics platform, with tubing extensions placed on the flow tube intake nozzles. Submersible pumps are attached to the outflow nozzle of each of the flow tubes, so that in situ water is drawn along the optical path. To insure that the in situ water measured by each ac-9 is sampled from the same depth, the intake tubes are positioned at the same vertical level on the platform and in very close horizontal proximity.

To avoid the possible effects of instrumentation drift, each ac-9 is normally field calibrated relative to a clean water standard once each sampling day. A Barnstead Nanopure[®] water system is used to produce the clean water calibration standard. When properly calibrated, the ac-9 has been shown to have an accuracy of $\sim 0.005 \text{ m}^{-1}$ [*Twardowski et al.*, 1999]. Postprocessing of the ac-9 data includes applying temperature and salinity corrections to the absorption and beam attenuation measurements following the methods described by *Pegau et al.* [1997]. The absorption measurements are further corrected for scattering errors to account for the portion of scattered light not measured by the detector [*Zaneveld et al.*,

1994; Moore *et al.*, 1996]. As the scattering correction of the absorption measurement utilizes the absorption and beam attenuation measurements at 715 nm, the IOP measurements at this wavelength are not included in this analysis.

Fractionation of the total absorption coefficient into dissolved and particulate portions is accomplished by utilizing two ac-9 meters. A 0.2 μm pore size filter is placed on the intake of the absorption tube of one of the ac-9 meters to provide a direct measurement of the absorption coefficient of chromophoric dissolved material $a_g(\lambda)$. In some instances, occasional problems created by the filter necessitated adjustment of the a_g spectrum by referencing the dissolved absorption profiles to the value measured at 676 nm. The dissolved absorption measurements at 676 nm are therefore not included in this study. The second ac-9 is operated unfiltered, providing a direct measurement of the absorption and beam attenuation coefficients due to particulate plus dissolved materials, $a_{pg}(\lambda)$, and $c_{pg}(\lambda)$, respectively. As the ac-9 meters provide measurements of absorption and attenuation coefficients in reference to pure water, we have chosen to denote the absorption and attenuation in these terms. They are equivalent to the total absorption or beam attenuation coefficient minus the contribution by water.

The particulate absorption fraction $a_p(\lambda)$, which contains contributions by detrital, phytoplankton, and sedimentary material, is estimated by subtraction of the filtered absorption measurements from the unfiltered measurements.

$$a_p(\lambda) = a_{pg}(\lambda) - a_g(\lambda)$$

The scattering coefficient for particles, $b_p(\lambda)$, is derived by subtraction of the absorption coefficient from the beam attenuation coefficient, assuming Rayleigh scattering of dissolved materials is negligible compared to that of particulate matter.

$$b_p(\lambda) = c_{pg}(\lambda) - a_{pg}(\lambda)$$

Over the past 3 years, we have collected IOP profiles using the SlowDROP system during eight research cruises located in six separate geographical regions. A description of the locations and dates of these cruises is given in Table 2.1. The IOP data from these cruises encompass a wide variety of oceanic regimes ranging from the equatorial Pacific to eutrophic coastal and estuarine waters. While all of the IOP data were collected in the northern hemisphere, we consider it to be global in the sense of the dynamic range observed in each IOP. In these terms, we consider the data set to be global in magnitude range, not necessarily in a spatial sense. The reader will also note that the global data set does not contain waters that would be considered to be purely “blue” (i.e. where the IOPs are strongly dependent on the characteristics of the water itself).

Over 1,000 profiles of the IOP have been collected during these cruises, at an average vertical resolution of approximately 0.2 m. Thus, the total number of depth samples collected for each of the IOP's is well over 200,000 at each wavelength. In order to reduce the number of data points to a manageable level, representative profiles of the IOP were selected from each of the individual cruise data sets and were vertically binned by selecting the median value in each depth interval. Data from each of the cruises were pooled into a global data set resulting

Table 2.1. Global data set description.

<i>Location</i>	<i>Data set ID</i>	<i>Dates</i>	<i>Approximate</i>		<i>No. profiles</i>	<i>No. samples</i>
			<i>Lat., N</i>	<i>Lon., W</i>		
Near coastal, CA	OCE95	Oct. 1995	33.22	117.44	8	200
Gulf of California	GOC95	Dec. 1995	28.00	112.50	11	436
Equatorial Pacific	ZF96	Apr.-May 1996	01.00	165.00	9	235
East Sound, WA	ES96	May-June 1996	48.65	122.89	12	340
North Atlantic Shelf	CMO96	Aug.-Sept. 1996	40.30	70.30	10	306
Chesapeake Bay	COPE96	Sept. 1996	36.80	75.83	17	203
Gulf of California	GOC96	Nov. 1996	27.80	111.50	12	249
North Atlantic Shelf	CMO97	Apr.-May 1997	40.30	70.30	10	632

Experiment abbreviations are as follows: OCE95, Oceanside, California, 1995; GOC95, Gulf of California, 1995; ZF96, Zonal Flux (equatorial Pacific), 1996; ES96, East Sound (Puget Sound), Washington, 1996; CMO96, Coastal Mixing and Optics (North Atlantic Shelf), 1996; COPE96, Chesapeake Bay Outflow Experiment (Maryland), 1996; GOC96, Gulf of California, 1996; CMO97, Coastal Mixing and Optics (North Atlantic Shelf), 1997. Total numbers of profiles and samples for the 1995-1996 data set are 77 and 1914, respectively.

in 1914 depth-binned samples for each of the IOP parameters described above at each of the respective wavelengths. As we are interested in examining the spectral relationships of each of the IOPs on a global scale, no effort has been made to exclude any water type or composition. Furthermore, no effort has been made to examine the relationships based on vertical structure. All portions of the water column were incorporated, including the bottom nepheloid layer, if present in shallow water casts.

2.4 RESULTS AND DISCUSSION

The spectral relationships of each of the IOP are examined in the following sections. As the results will show, the spectral dependency of each of the IOP can be described based on simple linear regressions. Although not included in this presentation, the spectral dependence was also examined using log-transformed data. While the log transformation models provide for more equal weighting of all data points, they are, however, more difficult to interpret and require a zero intercept. In most cases examined, only a slight improvement in the spectral IOP relationship models using a log transformation was found. Because linear models do not require a zero intercept, they can provide an estimate of the possible biases in the IOP measurements. Since one of the goals of this research is to examine the precision of the ac-9 measurements, the choice was therefore made to use the simpler linear models.

The spectral relationships are examined using the estimates of the individual IOP parameter at the 488 nm wavelength as the independent variable x and the measurements at each of the other wavelengths as the dependent variable y .

$$y(\lambda) = \beta x(488 \text{ nm}) + m$$

The β term is the slope, and the m term is the y intercept. The uncertainties in the model are assumed to be random and equivalent to the accuracy of the ac-9 measurements ($\pm 0.005 \text{ m}^{-1}$). Inaccurate calibrations or meter performance, however, may cause systematic biases in the measurements. The y intercepts

returned from the model regressions greater than the ac-9 measurement accuracy are assumed to be caused by calibrational and/or instrumental errors (i.e., biases). We therefore assume that the uncertainty in the model is equivalent to the accuracy of the ac-9 measurements ($\pm 0.005 \text{ m}^{-1}$).

Orthogonal least squares regressions are used to derive the linear models of individual IOP parameters in order to minimize the errors in both the 488 nm estimate and the estimate at other wavelengths. The choice of using the 488 nm wavelength as the independent x variable was made for a number of reasons. First, both the particulate and dissolved materials affect the optical properties at 488 nm, which allows this wavelength to be included in inversions of all parameters. Second, for remote sensing purposes, 488 nm is a wavelength at which reflectance is commonly measured. Third, the 488 nm band is near the center of the wavelength range of the ac-9 measurements, which minimizes errors that could be caused by using too large a wavelength interval. The standard error of the slope and y intercept as computed for each of the regressions in the following sections. As these values were always computed to be less than the uncertainty in the ac-9-meter ($\sim 0.005 \text{ m}^{-1}$), these values are not shown.

The magnitude of each of the optical parameters at 488 nm included in the global data set varies over approximately two orders of magnitude (Table 2.2). Note that individual cruise data sets do not exhibit the same range of variability as observed in the global data set. For the data obtained, only 14% of the total number of observations are in the upper order of magnitude of each IOP parameter data set.

Table 2.2. Inherent Optical Property ranges within each individual cruise data set at 488 nm.

Data Set	a_{pg}	a_g	a_p	c_{pg}	b_p
OCE95	0.009-0.318	0.003-0.038	0.006-0.297	0.159-1.925	0.146-1.696
GOC95	0.023-0.096	0.017-0.030	0.001-0.070	0.043-0.507	0.016-0.411
ZF96	0.008-0.028	0.004-0.011	0.000-0.019	0.026-0.157	0.016-0.131
ES96	0.137-1.543	0.059-0.125	0.070-1.476	0.478-8.079	0.283-6.595
CMO96	0.027-0.209	0.018-0.040	0.003-0.171	0.114-1.876	0.064-1.705
COPE96	0.092-0.523	0.052-0.159	0.019-0.367	0.412-3.373	0.318-3.116
GOC97	0.032-0.257	0.018-0.036	0.001-0.226	0.052-1.489	0.018-1.241
Global	0.008-1.543	0.003-0.159	0.000-1.476	0.026-8.079	0.016-6.595
CMO97	0.051-0.107	0.020-0.036	0.018-0.080	0.179-0.551	0.125-0.475

Values are m^{-1} .

In order to examine the influence of magnitude on the spectral IOP relationships, we provide results from the entire global data set and from two reduced data sets. The first reduced data set contains 14% of the total observations and encompasses approximately the upper order of magnitude of the IOP values in the global data set. The second reduced data set, which contains approximately the lower order of the IOP magnitude, includes 86% of the observations in the global data set (that is, most of the data are from relatively less turbid water). Finally, comparisons are made between the relationships resolved from the global data set and an IOP data set (CMO97) collected during a recent field experiment in order to indicate how variable the relationships are at local or regional scales.

2.4.1 Chromophoric Dissolved Absorption Coefficient $a_g(\lambda)$

The a_g at each of the ac-9 measured wavelengths are plotted versus $a_g(488 \text{ nm})$ in Figure 2.1. The results of the regressions, given in Table 2.3, show the spectral relationships at each of the wavelengths to be strongly linear, with r^2 values greater than 0.94 with the exception of the 650 nm band. The magnitude of $a_g(650 \text{ nm})$ is typically less than 0.01 m^{-1} , very near the accuracy of the ac-9 meter. Thus the low percentage of variability explained by the model of the absorption by dissolved materials at 650 nm is due to the decreased signal-to-noise ratio at this wavelength. At each wavelength, the y intercept is less than the measurement accuracy of the ac-9 meter indicating that they are not significantly different from zero and are thus unbiased.

The spectrum of absorption by dissolved organic material has often been assumed to decrease exponentially with wavelength [*Bricaud et al.*, 1981; *Carder et al.*, 1989; *Roesler et al.*, 1989]. Over the UV and visible wavelengths, the spectrum of the absorption by dissolved organic material has been modeled with the general exponential function

$$a_g(\lambda_i) = a_g(\lambda_r) \beta_{gi}$$

where $\beta_{gi} = \exp[-S(\lambda_i - \lambda_r)]$, $a_g(\lambda_r)$ is the dissolved absorption at a reference wavelength and S is the spectral slope of the absorption by dissolved materials.

The spectral slope has been estimated for various water types and has been found to be weakly variable in the global ocean environment [*Bricaud et al.*, 1981; *Carder et*

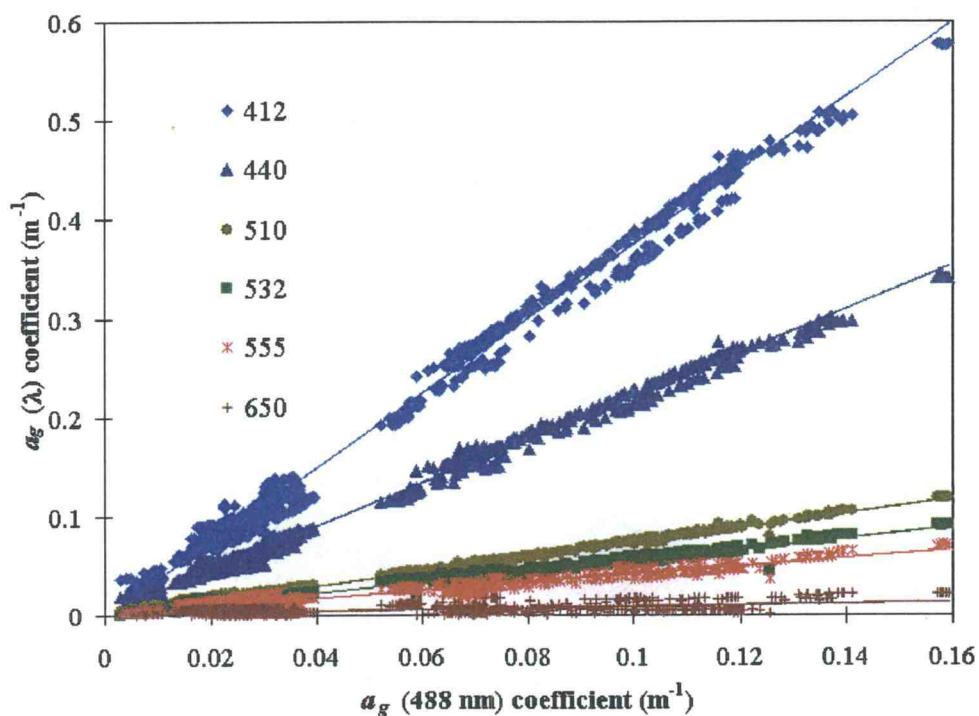


Figure 2.1. Dissolved absorption coefficient a_g measured at 488 nm versus the dissolved absorption coefficient measured at the six other wavelengths for the entire global data set. The linear regression fits at each wavelength (see Table 2.3) are shown as lines in the corresponding color.

al., 1991; Roesler *et al.*, 1989; Blough *et al.*, 1993; Hoge *et al.*, 1993]. In typical oceanic environments, the spectral slope varies from 0.014 to 0.018 nm^{-1} , depending on location [see Roesler *et al.*, 1989].

The average spectral slope S was determined for the global data set using two methods. First, the slopes from the regressions of $a_g(\lambda)$ versus $a_g(488 \text{ nm})$, shown in Table 2.3, were fit to the exponential model shown above using the absorption by dissolved materials at 488 nm as the reference wavelength. This

Table 2.3. Regression results of $a_g(\lambda)$ vs. $a_g(488 \text{ nm})$ using the entire global data set.

Wavelength λ , nm	Slope	y Intercept	Coefficient of Variation r^2
412	3.756	-0.001	0.993
440	2.200	0.002	0.995
488	1.000
510	0.745	-0.001	0.993
532	0.564	-0.001	0.983
555	0.414	0.000	0.947
650	0.076	0.001	0.355

Number of samples in the global data set is 1914.

method resulted in a spectral slope of $S = 0.016 \text{ nm}^{-1}$, with an $r^2 = 0.99$. In the second method, the spectral slope S was determined using the exponential model at each vertically binned sample using $a_g(488 \text{ nm})$ as the reference wavelength. The ensemble spectral slope mean was computed by taking the average of sample spectral slopes over all of the depth bin samples. The mean slope over all profiles was $S = 0.015 \text{ nm}^{-1}$, with a standard deviation of ± 0.003 . The good agreement between the two methods (within 0.001 nm^{-1}) suggests that the spectral shape of the absorption by dissolved organic matter is accurately modeled using the simple linear relationships resolved from the global data set. Furthermore, these results suggest that the absorption by dissolved materials can be accurately estimated using the exponential form shown above, using the absorption measured at 488 nm as the reference wavelength and a spectral slope $S = 0.015 \text{ nm}^{-1}$.

Similar results in the spectral relationships were found using the lower and upper order of magnitude data sets, suggesting that the spectral shape of the absorption by dissolved materials is independent of the magnitude of the total absorption. As the global data set used in this study encompasses a variety of oceanic environments and a wide range of a_g values, we conclude that simple linear models can be used to accurately predict the spectrum of the absorption by dissolved organic matter for most oceanic environments.

2.4.2 Particulate Absorption Coefficient $a_p(\lambda)$

The a_p values from the global data set at each wavelength versus the a_p (488 nm) are shown in Figure 2.2. The absorption coefficient due to particulate matter was derived from two ac-9 measurements; the uncertainty of each is assumed to be random and equal to 0.005 m^{-1} . Thus the uncertainty in the particulate absorption model due to calibration and instrument errors is assumed to be 0.007 m^{-1} . The percentage of variability explained is greater than 95% for each of the wavelengths (Table 2.4). In general, the lowest r^2 values and largest y intercepts are in the blue and red portions of the spectrum. In the blue wavelengths, the shape of the absorption spectrum is strongly dependent on the concentration of detritus and the chlorophyll pigment structure of phytoplankton [Morrow *et al.*, 1989; Bricaud and Stramski, 1990; Bricaud *et al.*, 1995b]. It is therefore not surprising that the 412 nm band shows the lowest r^2 value, where variability in the proportion of detrital to

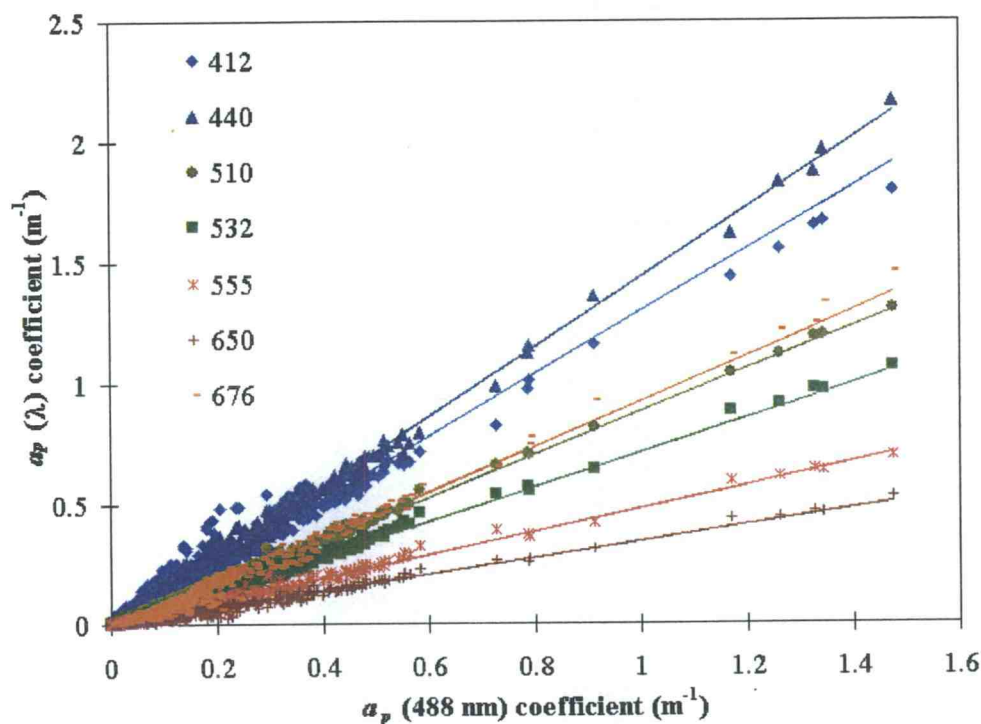


Figure 2.2. Same as Figure 2.1, but for the particulate absorption coefficient a_p . See Table 2.4 for the linear regression statistics.

pigmented absorbing matter is expected to be the greatest. In the red portion of the spectrum, differences in the absorption spectra of detritus and phytoplankton, variability in the shape of the secondary maximum of chlorophyll pigments, and variations in the blue to red absorption ratios cause the lowered r^2 values and the increased y intercepts.

We noted that 14% of the particulate absorption values at 488 nm in the global data set are in the upper 90% of the data range, $0.142 \leq a_p(488) \leq 1.476 \text{ m}^{-1}$. In order to elucidate the influence of these high values on the regressions, we

Table 2.4. Regression results of $a_p(\lambda)$ versus $a_p(488 \text{ nm})$ using the entire global data set.

λ , nm	Slope	y Intercept	Coefficient of Variation r^2
412	1.287	0.009	0.965
440	1.434	0.003	0.995
488	1.000
510	0.886	-0.003	0.996
532	0.718	-0.004	0.991
555	0.482	-0.001	0.981
650	0.345	-0.001	0.967
676	0.937	-0.012	0.977

Number of samples in the global data set is 1914.

divided the a_p data into lower and upper order of magnitude data sets based on the a_p value at 488 nm. The lower order of magnitude data set includes a_p values of less than 0.142 m^{-1} at 488 nm, and the upper order of magnitude data set contains a_p values greater than 0.142 m^{-1} at 488 nm. The regression results using these reduced data sets are shown in Table 2.5. In the lower order of magnitude data set, the r^2 regression values are smaller compared to the upper order of magnitude values. However, the y intercepts returned from the regressions on the lower order magnitude data set are smaller than the upper order of magnitude y intercepts.

Recall that our definition of the absorption coefficient due to particulate matter includes pigmented (phytoplankton) and nonpigmented particulate material (i.e., detritus and sediments). The absorption by detrital material has been shown to decrease exponentially with increasing wavelength, similar to that of dissolved materials [Roesler *et al.*, 1989; Bricaud and Stramski, 1990; Hoepffner and

Table 2.5. Regression results of $a_p(\lambda)$ versus $a_p(488 \text{ nm})$ using the lower and upper magnitude data sets.

λ , nm	Lower 86% Magnitude Data Set			Upper 14% Magnitude Data Set		
	Slope	y Intercept	r^2	Slope	y Intercept	r^2
412	1.578	-0.002	0.871	1.260	0.012	0.944
440	1.486	0.001	0.972	1.432	0.003	0.991
488	1.000	1.000
510	0.830	-0.001	0.981	0.902	-0.008	0.995
532	0.644	-0.001	0.951	0.744	-0.014	0.989
555	0.437	0.001	0.885	0.496	-0.006	0.973
650	0.301	0.001	0.795	0.363	-0.008	0.958
676	0.740	-0.003	0.895	1.007	-0.038	0.972

Sathyendranath, 1993]. The slope of the detrital absorption spectrum, which is generally lower than that of the dissolved absorption spectrum, has a typical value of $-0.011 \pm 0.002 \text{ nm}^{-1}$ [*Roesler, et al.*, 1989]. While the global data set does not provide any information as to the proportions of detrital and phytoplankton absorption, we utilize the results of the regressions of the two reduced data sets to explain the spectral relationships observed in the particulate absorption coefficient.

In the upper range of the a_p values ($\geq 0.142 \text{ m}^{-1}$), we hypothesize that the detrital fraction is very small or insignificant in comparison to the absorption by phytoplankton. The shape of the particulate absorption spectrum, as determined from the slopes of the regressions on the upper magnitude data set, is similar to a typical phytoplankton absorption spectrum (Figure 2.3), with absorption peaks near the chlorophyll absorption wavelengths (440 and 676 nm). Notice that the 412/488 nm spectral ratio is lower than the 440/488 nm ratio (Table 2.5), indicating that the

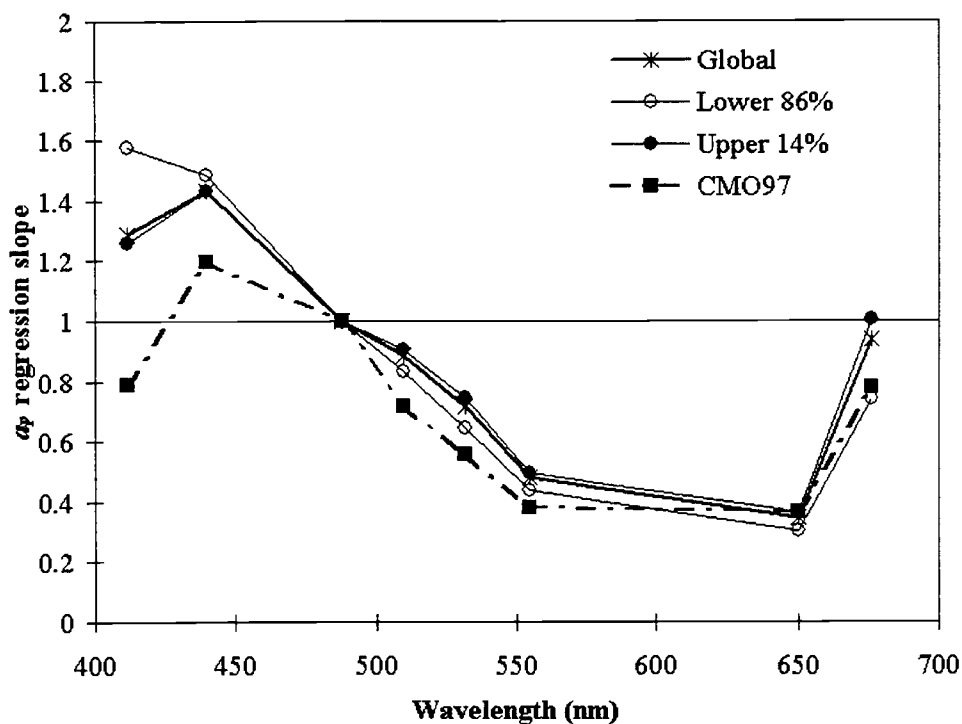


Figure 2.3. The spectrum of the slopes of the $a_p(\lambda)$ returned from the regressions versus $a_p(488 \text{ nm})$ from the global data set (thick line with asterisks), the lower magnitude data set (solid line with open circles) and the upper magnitude data set (solid line with filled circles) given in Tables 4 and 5. Also shown is the spectrum of the $a_p(\lambda)$ slopes (hatched line with filled squares) returned from regressions of the CMO97 data set only.

absorption by detrital matter, which increases exponentially with decreasing wavelength, is small or insignificant in the upper order of magnitude subset. A plot of the y intercepts of the particulate absorption regressions of the upper order magnitude data set shows that the largest offsets from zero occur at 412, 532, and 676 nm (Figure 2.4). Using absorption spectra obtained from 14 cultures of phytoplankton species, *Roesler et al.* [1989] showed that the largest variance in the

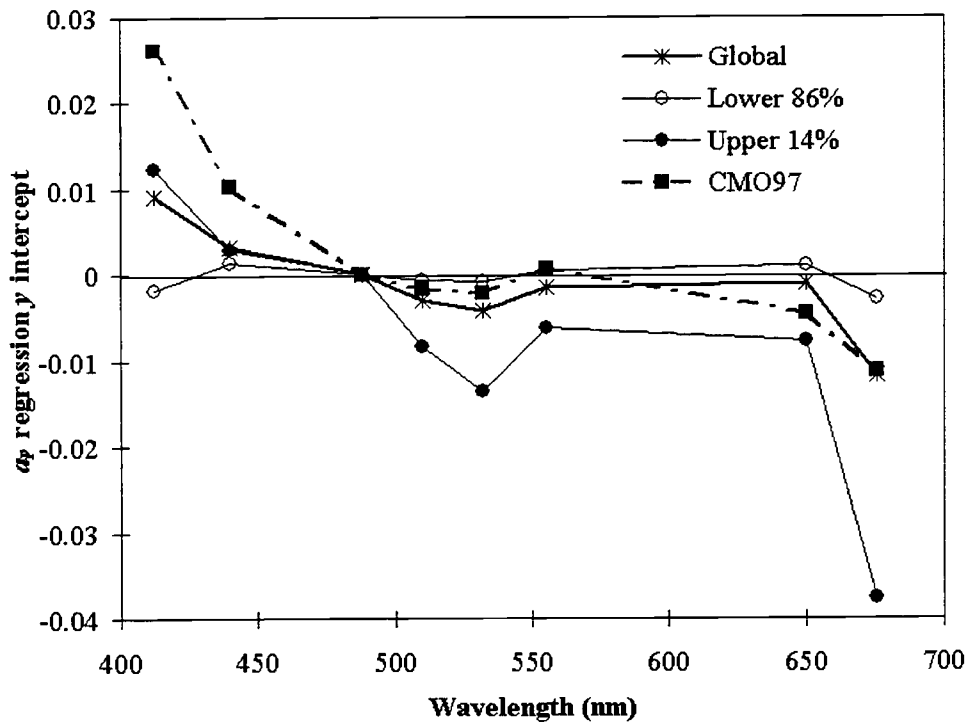


Figure 2.4. The spectrum of the y intercepts of the $a_p(\lambda)$ returned from the regressions versus $a_p(488 \text{ nm})$ from the global data set (thick line with asterisks), the lower magnitude data set (solid line with open circles) and the upper magnitude data set (solid line with filled circles) given in Tables 4 and 5. Also shown is the spectrum of the $a_p(\lambda)$ y intercepts (hatched line with filled squares) returned from regressions of the CMO97 data only.

phytoplankton absorption spectra occurred near the 532 and 676 nm wavelengths. Thus the large biases observed at these wavelengths in the upper order magnitude data set correspond well to the expected variance due to varying pigment composition and packaging by phytoplankton. The absorption by detrital matter, which is highest in the blue wavelengths, may be large enough to influence the regression at 412 nm.

In the lower ranges of the a_p values ($< 0.142 \text{ m}^{-1}$), we hypothesize that the contribution of the absorption by detrital material is a significant proportion of the particulate absorption coefficient. Notice that the spectral slope at 412 nm is greater than the slope at 440 nm in the lower order magnitude regressions (Figure 2.3), consistent with the hypothesis of the increased detrital absorbing fraction. Also note that the lower order magnitude spectral slope is lower than the slope from the global data set at 676 nm. As the detrital absorption spectrum follows an exponential form, the absorption at 676 nm is expected to be very small or near zero, and thus the particulate absorption at 676 nm is due mainly to phytoplankton chlorophyll a pigments. However, at 488 nm the particulate absorption coefficient is influenced by both the detrital and phytoplankton fractions. Thus the 676/488 nm spectral ratio is reduced owing to the fact that detritus absorbs more strongly at 488 nm than at 676 nm. A plot of the y intercepts returned from the lower magnitude particulate absorption data set shows that there are no significant biases (i.e. $< 0.007 \text{ m}^{-1}$). However, note that the r^2 values are greatly reduced as compared to the r^2 values returned from the regression of the global and upper order magnitude data sets. *Bricaud and Stramski [1990]* found that the contribution of detrital matter to the total absorption at 440 nm varied between 12 to 82 % in the Sargasso Sea and from 5 to 42 % in the Peruvian upwelling system. We hypothesize that the noncovarying fractions of detrital and phytoplankton absorption increase the scatter in the spectral ratio relationships, thus lowering the r^2 values. Also note that the regressions of the particulate absorption are highly

influenced by the a_p values greater than 0.142 m^{-1} , as indicated by the similar spectral shapes of the global and upper order magnitude data sets (Figure 2.3). This is most likely due to the fact that the range of the a_p values in the upper order magnitude data set (1.334 m^{-1}) is much greater than the range of values in the lower order magnitude data set (0.142 m^{-1}).

2.4.3 Total Absorption Coefficient Without Water $a_{pg}(\lambda)$

The spectral total absorption coefficient, excluding the contribution by water, for the global data set are plotted versus the value measured at 488 nm in Figure 2.5. The slopes, y intercepts, and the r^2 regression values are shown in Table 2.6. The spectral relationships of the total absorption coefficients are shown to be linear, with r^2 values ranging from 0.932 at 412 nm to 0.997 at 510 nm. Note, however, that with the exception of the 555 and 650 nm bands, the absolute value of the y intercepts are greater than the uncertainty due to the ac-9 measurements ($\sim 0.005 \text{ m}^{-1}$). The causes of these y intercepts are examined in a similar manner as the a_p data.

The total absorption data was separated into a lower order magnitude data set, with a_{pg} values at 488 nm less than 0.225 m^{-1} (86% of the total) and an upper order magnitude data where $0.225 \leq a_{pg}(488 \text{ nm}) \leq 1.55 \text{ m}^{-1}$ (14 % of the total). Statistics from the regressions of these two reduced data sets are presented in Table

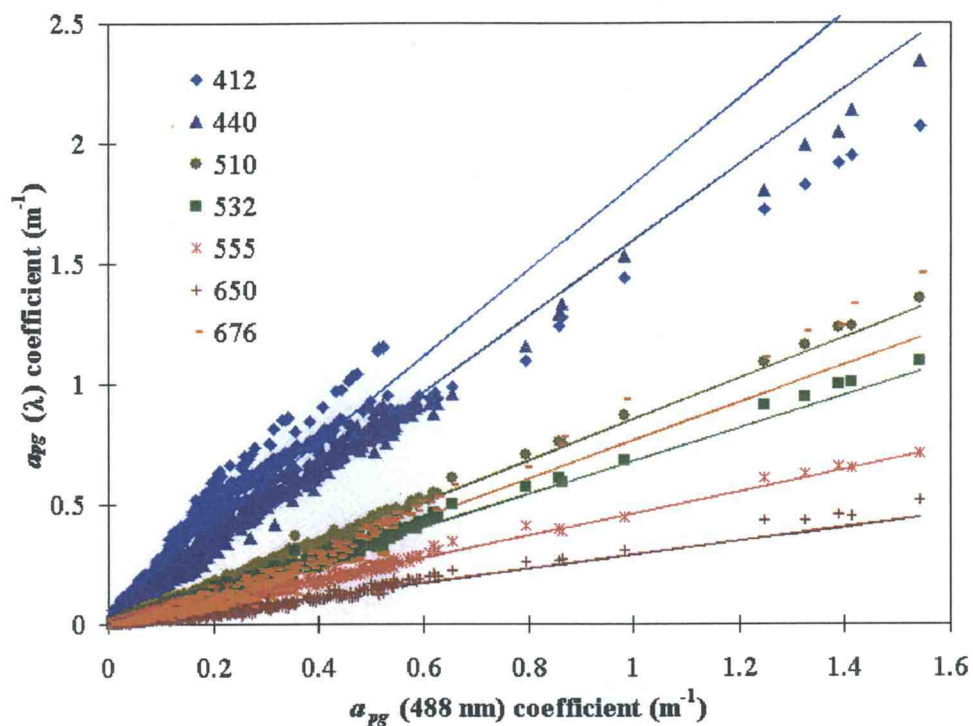


Figure 2.5. Same as Figure 2.1, but for the total absorption coefficient less water a_{pg} . See Table 2.6 for the linear regression statistics.

Table 2.6. Regression results of $a_{pg}(\lambda)$ versus $a_{pg}(488 \text{ nm})$ using the entire global data set.

λ , nm	Slope	y Intercept	Coefficient of Variation r^2
412	1.781	0.048	0.929
440	1.578	0.019	0.990
488	1.000
510	0.859	-0.006	0.997
532	0.687	-0.008	0.992
555	0.462	-0.002	0.984
650	0.292	-0.004	0.942
676	0.795	-0.030	0.940

Number of samples in the global data set is 1914.

2.7. The r^2 values from the lower order magnitude regressions are smaller than the global values and are also less than the upper order magnitude regression values,

Table 2.7. Regression results of $a_{pg}(\lambda)$ versus $a_{pg}(488 \text{ nm})$ using the lower and upper magnitude data sets.

λ , nm	Lower 86% Magnitude Data Set			Upper 14% Magnitude Data Set		
	Slope	y Intercept	r^2	Slope	y Intercept	r^2
412	2.432	0.002	0.913	1.245	0.257	0.884
440	1.756	0.005	0.976	1.430	0.081	0.986
488	1.000	1.000
510	0.808	-0.002	0.991	0.900	-0.024	0.995
532	0.631	-0.003	0.977	0.743	-0.032	0.988
555	0.435	0.001	0.931	0.486	-0.012	0.975
650	0.227	0.001	0.737	0.359	-0.034	0.961
676	0.511	-0.008	0.845	1.033	-0.139	0.969

with the exception of the 412 nm band. The lower order magnitude regression slopes are larger than the global and upper order magnitude regression slopes at wavelengths less than 488 nm, and smaller at wavelengths greater than 488 nm. However, the y intercepts from the lower order magnitude regressions are not significantly different from zero, with the possible exception of the 676 nm wavelength.

The spectrum of the lower order magnitude regression slopes has a definite exponential shape over the 412 to 650 nm wavelengths, suggesting that dissolved fraction is a significant component of the total absorption coefficient (Figure 2.6). This can be seen further in a plot of particulate and dissolved absorption fractions at

488 nm versus the total absorption coefficient at 488 nm (Figure 2.7). At a_{pg} values less than 0.225 m^{-1} , the dissolved and particulate fractions are similar in magnitude, indicating that the a_{pg} spectral shape is due to both the dissolved and particulate

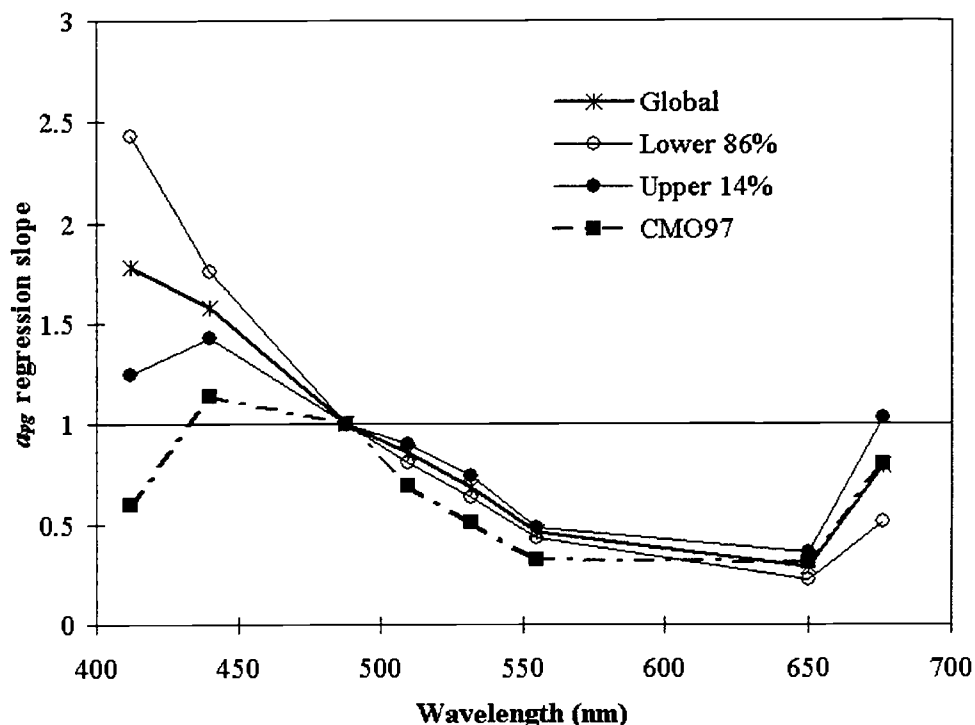


Figure 2.6. The spectrum of the slopes of the $a_{pg}(\lambda)$ returned from the regressions versus $a_{pg}(488 \text{ nm})$ from the global data set (thick line with asterisks), the lower magnitude data set (solid line with open circles) and the upper magnitude data set (solid line with filled circles) given in Tables 6 and 7. Also shown is the spectrum of the $a_{pg}(\lambda)$ slopes (hatched line with filled squares) returned from regressions of the CMO97 data set only.

absorption fractions. The lower r^2 values are due to the reduced magnitude range and the noncovariance of the dissolved and particulate fractions, similar to the

detrital and phytoplankton absorption noncovariance at the lower particulate absorption range.

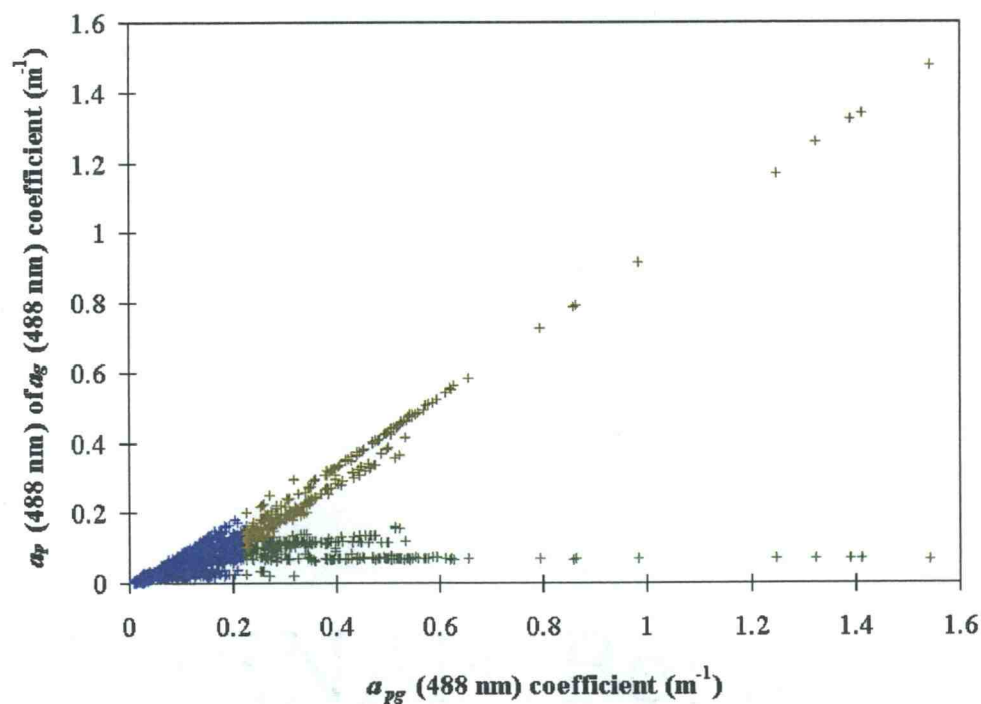


Figure 2.7. Dissolved absorption coefficient at 488 nm versus the total absorption coefficient at 488 nm for the lower 86% magnitude data set (blue) and the upper 14% magnitude data set (green). Also plotted is the particulate absorption coefficient at 488 nm versus the total absorption coefficient at 488 nm for the lower 86% magnitude data set (cyan) and the upper 14% magnitude data set (olive green).

The slopes of the a_{pg} regressions of the upper order magnitude data set are similar to the a_p regression slopes of the upper order magnitude data set (Figures 2.3 and 2.6), suggesting that the absorption by phytoplankton dominates the spectral relationships at a_{pg} values greater than 0.225 m^{-1} at 488 nm. Note,

however, that there is a significant offset from zero in the a_{pg} y intercepts of the upper order magnitude data set as shown in Figure 2.8. Recall that the y intercepts of the a_p regressions of the upper order magnitude data were also offset from zero, owing primarily to varying pigment composition and packaging of phytoplankton. However, the absolute value of these offsets is much less than the absolute value of

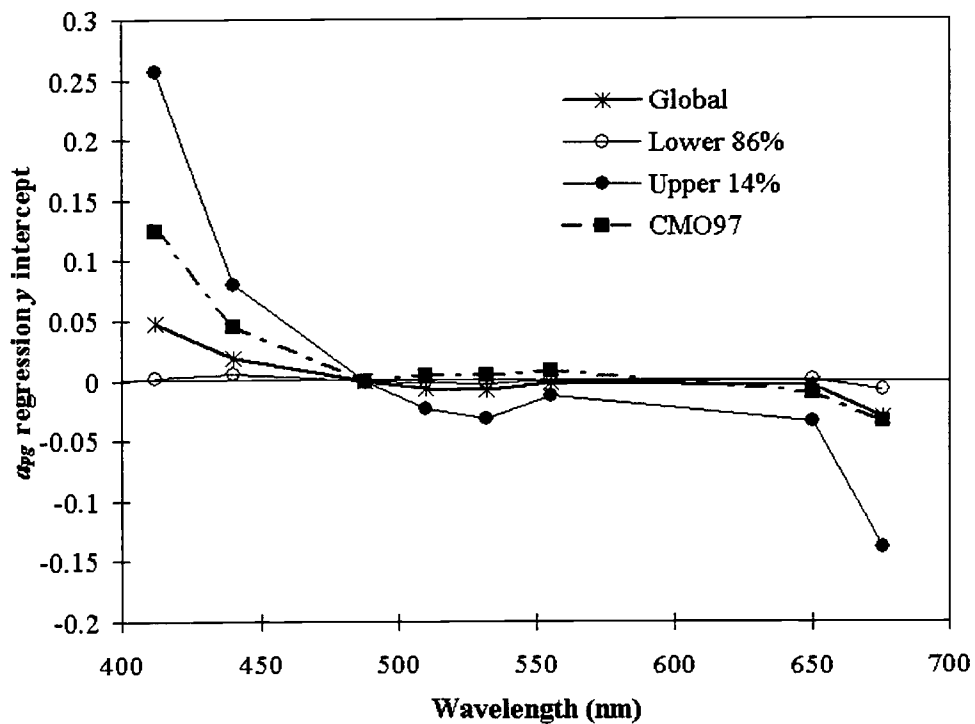


Figure 2.8. The spectrum of the y intercepts of the $a_{pg}(\lambda)$ returned from the regressions versus $a_{pg}(488 \text{ nm})$ from the global data set (thick line with asterisks), the lower magnitude data set (solid line with open circles) and the upper magnitude data set (solid line with filled circles) given in Tables 6 and 7. Also shown is the spectrum of the $a_{pg}(\lambda)$ y intercepts (hatched line with filled squares) returned from regressions of the CMO97 data set only.

the a_{pg} offsets of the upper order magnitude data set, especially in the blue wavelengths. Thus these offsets cannot be entirely due to varying phytoplankton pigment structure.

Figure 2.7 shows that for a_{pg} values at 488 nm greater than 0.225 m^{-1} , the a_g at 488 nm is relatively constant. Thus increases in the a_{pg} at 488 nm greater than 0.225 m^{-1} are due primarily to increases in a_p . If the dissolved and particulate matter do not covary but, instead, the dissolved matter concentrations are constant or independent of the particulate absorption, the y offsets would indicate the background concentrations of a_g .

Finally, note that the a_{pg} spectrum of the global data set lies in between the spectra of the lower and upper order magnitude data sets (Figure 2.6). This implies that the global relationships of the a_{pg} are not as heavily influenced by the upper order magnitude range as in the case of the absorption by particulate matter and may represent a more realistic relationship as observed in the oceans.

2.4.4 Particulate Scattering Coefficient $b_p(\lambda)$

The spectral scattering coefficient is plotted versus scattering at 488 nm in Figure 2.9, with the statistics of the regressions shown in Table 2.8. Previous measurements of the spectral scattering coefficient are almost nonexistent. The scattering coefficient is often modeled as a power-law relationship with wavelength λ^{-n} [Gordon *et al.*, 1988; Sathyendranath, *et al.* 1989; Lee *et al.*, 1994]. Because of

anomalous dispersion, we expect that in phytoplankton-dominated absorption waters, the scattering coefficient will have a spectral shape that is similar to the inverse of the particulate absorption [Zaneveld and Kitchen, 1995]. We find that the spectrum of the scattering coefficient is nearly flat (Figure 2.10), with $n = -0.1$ when fit to a power law function. It does retain a wavelength dependence that is similar to the inverse of the absorption spectrum, although the magnitude of the slopes is much lower (Figure 2.10). Similar spectral relationships were found for

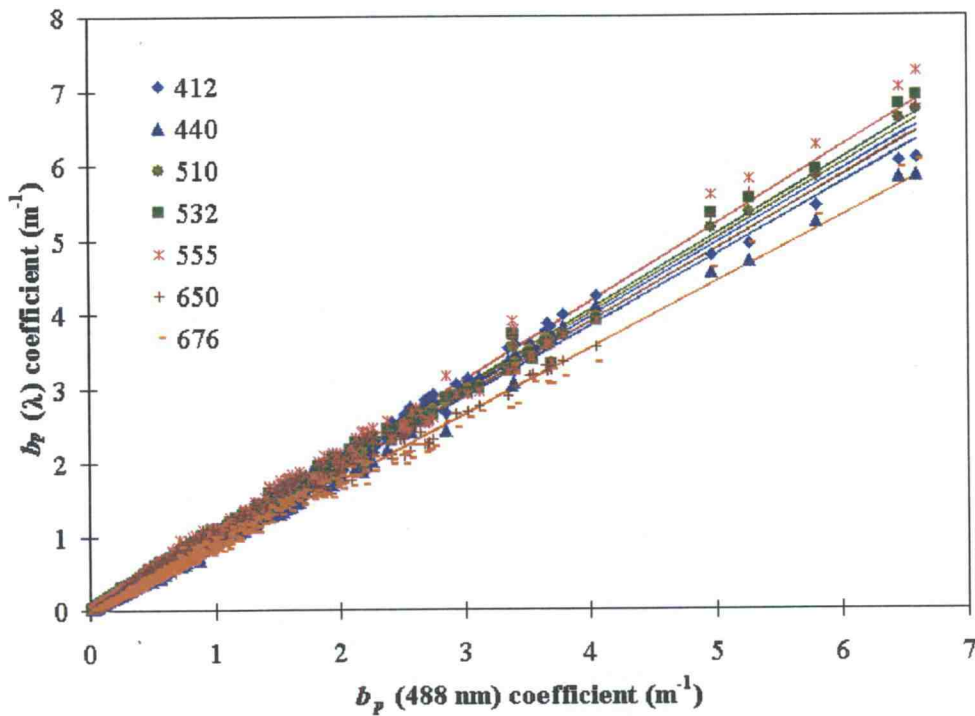


Figure 2.9. Same as Figure 2.1, but for the particulate scattering coefficient b_p .

Table 2.8. Regression results of $b_p(\lambda)$ versus $b_p(488 \text{ nm})$ using the entire global data set.

λ , nm	Slope	y Intercept	Coefficient of Variation r^2
412	0.986	0.009	0.996
440	0.957	0.006	0.995
488	1.000
510	1.002	0.000	0.999
532	1.013	-0.004	0.997
555	1.042	-0.010	0.993
650	0.978	-0.016	0.987
676	0.886	-0.011	0.994

Number of samples in the global data set is 1914.

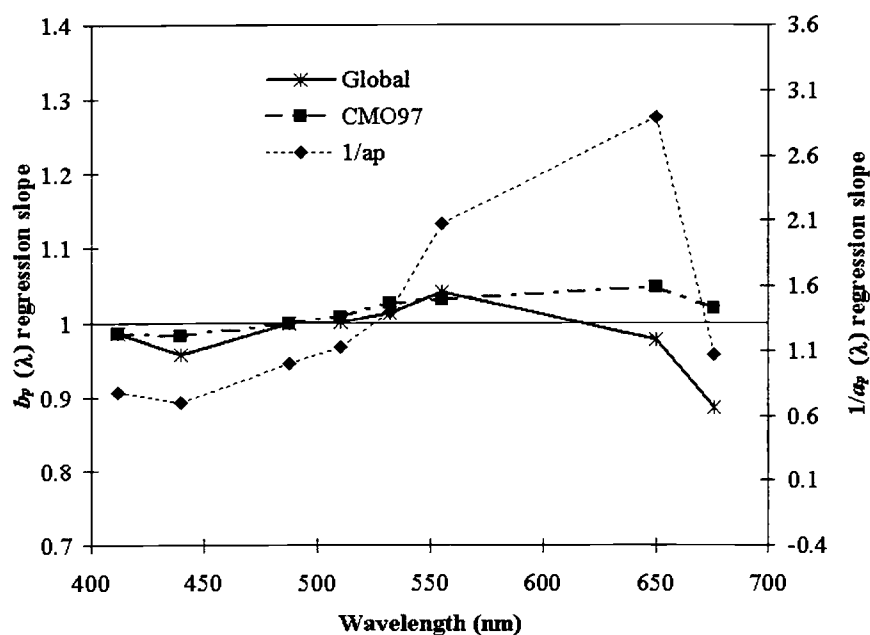


Figure 2.10. Global data set slopes of $b_p(\lambda)$ from the least squares regressions plotted versus wavelength (thick line with asterisks). The inverse of the particulate absorption regressions slope (dashed line with solid diamonds) is plotted for comparison. Also shown is the spectrum of the $b_p(\lambda)$ slopes (hatched line with solid squares) returned from regressions of the CMO97 data set only.

the global and both lower and upper particulate scattering data sets which implies that absorbing particles dominate the data collected at these scattering levels. The non-zero y intercepts seen in the absorption coefficient is repeated in the analysis of the scattering coefficient. We hypothesize that the presence of a background level of detrital particles may cause the offset observed in the scattering coefficient.

2.4.5 Beam Attenuation Coefficient $c_{pg}(\lambda)$

Figure 2.11 illustrates the spectral relationship of $c_{pg}(\lambda)$ versus $c_{pg}(488 \text{ nm})$ for the entire global data set, with the regression statistics listed in Table 2.9. The data shows a strong linear spectral relationship in beam attenuation, with the lowest r^2 value of 0.989 at 412 nm. The y intercepts of the regressions are nonzero and much larger than the uncertainty due to the accuracy in the ac-9 measurements.

A similar study by *Voss* [1992] examined the spectral dependency of the beam attenuation coefficient as measured using various beam transmissometers. The slopes and y intercepts from the study by *Voss* [1992] and the present study plotted in Figures 2.12 and 2.13, respectively, for comparison. Although the *Voss* [1992] study used wavelengths that are slightly different from ours, the following general comparisons can be made. At 440 nm, the slopes are in good agreement (Figure 2.12). However, moving into the green and red portion of the spectrum, the slopes given by *Voss* are lower than those obtained in this study. Furthermore, the apparent increase in slope at 550 nm is not seen in the regressions using our global

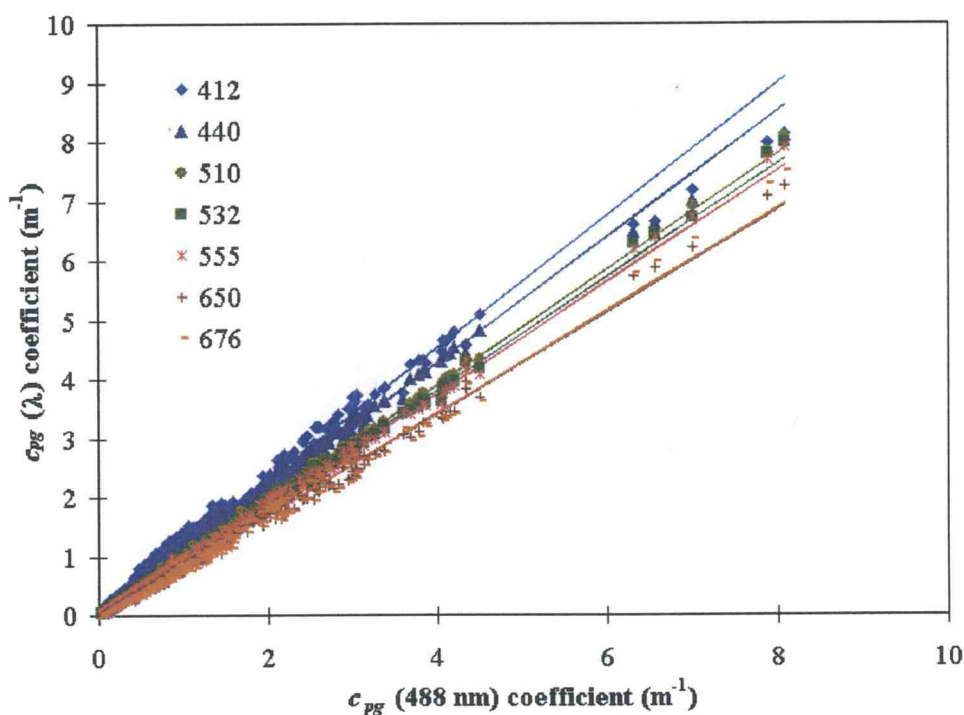


Figure 2.11. Same as Figure 2.1, but for the beam attenuation coefficient less water c_{pg} . See Table 2.8 for the linear regression statistics.

Table 2.9. Regression results of $c_{pg}(\lambda)$ versus $c_{pg}(488 \text{ nm})$ using the entire global data set.

λ , nm	Slope	y Intercept	Coefficient of Variation r^2
412	1.115	0.076	0.989
440	1.059	0.039	0.997
488	1.000
510	0.977	-0.008	0.999
532	0.957	-0.017	0.999
555	0.943	-0.023	0.998
650	0.862	-0.034	0.995
676	0.866	-0.040	0.993

Number of samples in the global data set is 1914.

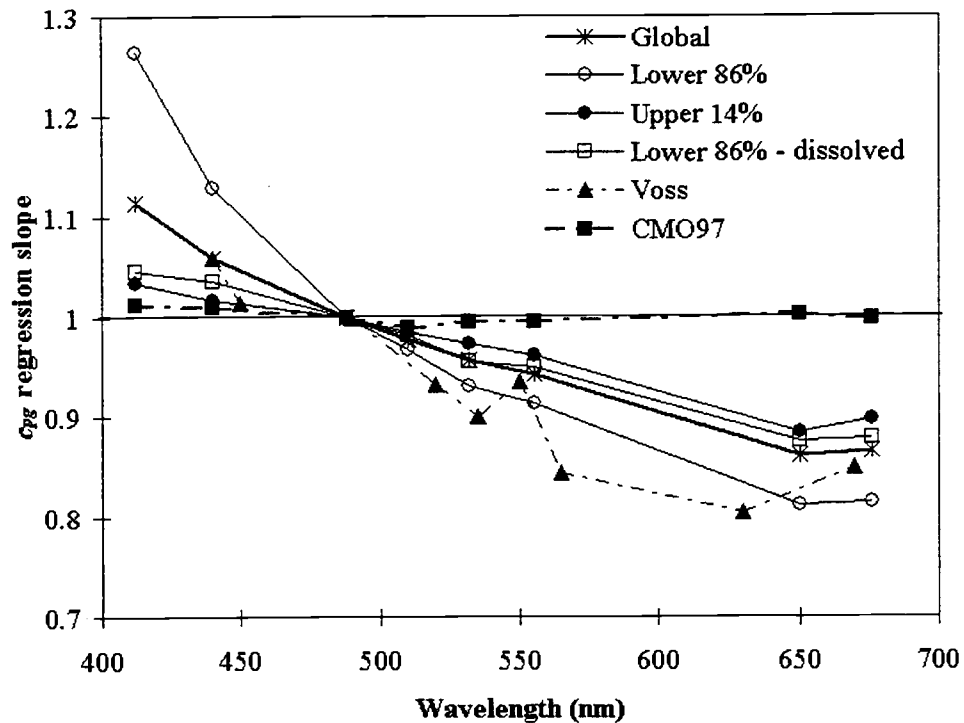


Figure 2.12. Slopes of $c_{pg}(\lambda)$ returned from the least squares regressions versus $c_{pg}(488 \text{ nm})$ using the full data set (thick line with asterisks). Also shown are the slopes from the lower magnitude data set (solid line with open circles) and the upper magnitude data set (solid line with solid circles). For comparison, the slopes given by Voss [1992] are plotted (hatched line with solid triangles). The slopes from the regressions using the lower magnitude data set ($c_{pg}(488 \text{ nm}) < 1.0 \text{ m}^{-1}$) with the dissolved absorption subtracted are also plotted (solid line with open squares). The spectrum of the $c_{pg}(\lambda)$ slopes (hatched line with solid squares) returned from regressions of the CMO97 data set only are also shown.

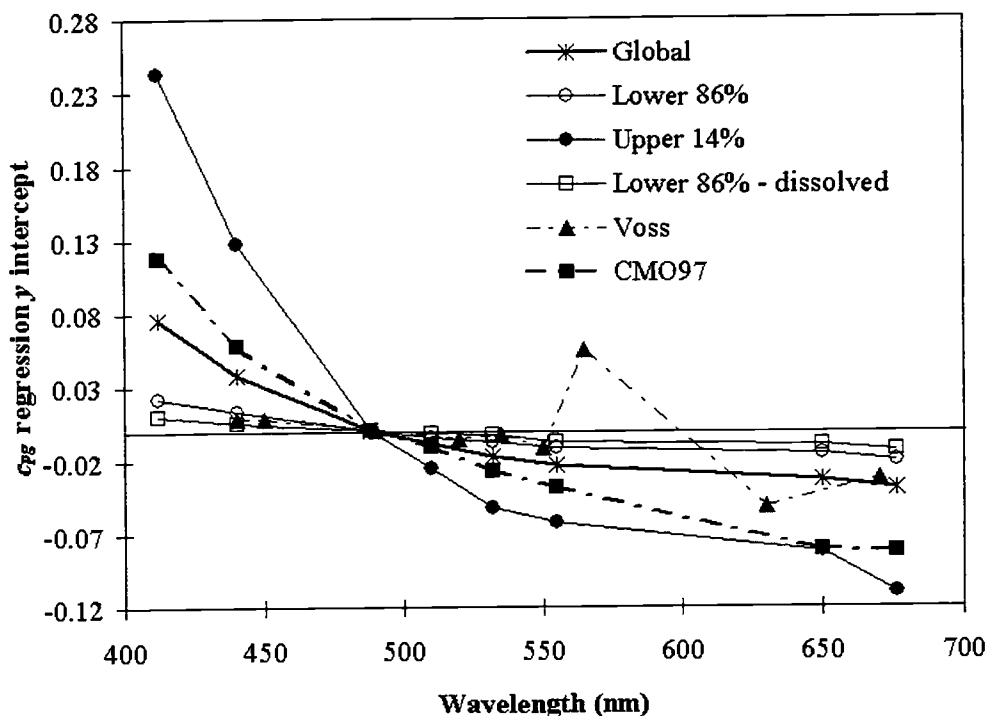


Figure 2.13. The y intercepts of $c_{pg}(\lambda)$ returned from the least squares regressions versus $c_{pg}(488 \text{ nm})$ using the full data set (thick line with asterisks). Also shown are the y intercepts from the lower magnitude data set (solid line with open circles) and the upper magnitude data set (solid line with solid circles). For comparison, the y intercepts given by Voss [1992] are plotted (hatched line with solid triangles). The y intercepts from the regressions using the lower magnitude data set ($c_{pg}(488 \text{ nm}) < 1.0 \text{ m}^{-1}$) with the dissolved absorption subtracted are also plotted (solid line with open squares). The spectrum of the $c_{pg}(\lambda)$ y intercepts (hatched line with solid squares) returned from regressions of the CMO97 data set only are also shown.

data set. The y intercepts computed in Voss's regressions are also nonzero, which he attributes to calibration and beam attenuation by water measurement errors.

It should be noted that the range of the beam attenuation coefficients used in the study by Voss [1992] is much smaller than that of the global data set. Although the exact ranges are not given, the majority of the beam attenuation measurements at 490 nm used by Voss are less than 1.0 m^{-1} . Restricting our data set to values less than 1.0 m^{-1} at 488 nm reduces the size of the global data set by 14% (N=1646).

The results of the regressions using the reduced data set are shown in Table 2.10.

Table 2.10. Two-way regression results of $c_{pg}(\lambda)$ versus $c_{pg}(488 \text{ nm})$ using $c_{pg}(488 \text{ nm})$ values less than 1.0 m^{-1} only and with the subtraction of the dissolved absorption values.

λ , nm	Slope $c_{pg} < 1.0$	y Intercept	r^2	Slope $c_{pg} - a_g$	y Intercept	r^2
412	1.268	0.023	0.975	1.045	0.011	0.994
440	1.128	0.013	0.992	1.036	0.005	0.997
488	1.000	1.000
510	0.967	-0.004	0.998	0.981	-0.001	0.998
532	0.93	-0.007	0.998	0.956	-0.003	0.997
555	0.913	-0.012	0.996	0.949	-0.007	0.995
650	0.811	-0.016	0.992	0.875	-0.010	0.990
676	0.814	-0.020	0.990	0.878	-0.014	0.988

Number of samples is 1646 or 86% of the total.

The effect of excluding the higher beam attenuation values increases the slope in the blue while decreasing the slope in the red and green wavelengths (Figure 2.12).

The slopes in the red and green portion of the spectrum and the y intercept values are close to those reported by Voss [1992]. Although the y offsets are reduced, they

are still greater than would be expected, given the expected accuracy of the measurements (0.005 m^{-1}).

A possible source of these offsets may be due to background concentrations of absorbing or scattering (i.e. detrital and/or dissolved organic) material which does not covary with particle concentrations. The spectral shape of the y intercepts shows a strong exponential decrease with wavelength (Figure 2.13). We found the exponential slope of the y offsets to be 0.009, slightly lower than the expected shapes of the detrital and dissolved absorption spectra. This indicates that the nonzero intercepts may be related to the detrital and/or dissolved absorption coefficient. If the absorption by detrital and/or dissolved materials did not covary with the absorption by particulate matter, but instead, they were constant or independent of the particulate absorption, the y offsets would indicate the background concentrations of detrital and dissolved absorption.

Voss [1992] concludes from his data set that the dissolved matter appears to covary with the particles. We show this is true up to certain concentrations (see Figure 2.7). Thus, for a given region, there is some upper maximum in dissolved absorption, past which the dissolved absorption remains approximately constant, irrespective of the particle concentration. The opposite case is also true. In clear waters, it is possible for the particulate attenuation to approach zero, leaving the attenuation coefficient strongly dependent on the absorption by the dissolved materials. In other words, the dynamic range of the absorption due to dissolved materials is much less than that due to particles, as already indicated in Table 2.2.

These factors determine the nonzero intercepts in the regressions of the total attenuation coefficient; that is, the background dissolved absorption coefficients drive the high end of the regression down and the low end up. These results imply that the spectral shape of the beam attenuation coefficient is dependent on the relative concentrations of the dissolved and particulate fractions, similar to the results presented for the total absorption coefficient.

After removing the contribution of the dissolved component absorption to the beam attenuation coefficient, the y intercepts were closer to zero (Table 2.10). The small offset that remains is spectrally dependent with a linear shape that increases towards shorter wavelengths (Figure 2.13). After removal of the dissolved component, the offset in the y intercept values was only weakly dependent on the range of the beam attenuation values included in the calculation. Although many of the y intercept values are within the uncertainty of the ac-9 measurements, the regular shape of the offset leads us to believe that much of the remaining offset is due to factors other than calibration of the instrumentation. We postulate that the remaining offset in the y intercepts is partially caused by a background level of attenuation that is associated with the scattering and absorption by detritus.

For c_{pg} values greater than 1.0 m^{-1} , the spectrum of the regression slopes is much more flatter than the spectrum of the global slopes (Figure 2.12). As was shown for the upper order of magnitude range of the a_{pg} data, the spectrum of the regression slopes is similar to the typical phytoplankton absorption spectrum

(Figure 2.6). In section 2.4.4, we showed that the spectrum of the b_p regression slopes is similar to the inverse of the spectrum of the a_p regression slopes (Figure 2.10). We therefore conclude that at c_{pg} values greater than 1.0 m^{-1} , the particulate scattering and the absorption by phytoplankton cause the flattening of the spectrum of the c_{pg} regression slopes. Note, however, that the y intercepts from the regressions of c_{pg} values greater than 1.0 m^{-1} are similar in shape and magnitude to those returned from the regressions of the upper magnitude range of a_{pg} data (Figure 2.8). As with the a_{pg} , the background levels of the absorption by dissolved organic materials may cause the y offsets in the regressions at c_{pg} greater than 1.0 m^{-1} .

2.4.6 The CMO97 Data Set: Regional Differences

In analyses similar to the global data set, linear models were used to examine the spectral relationships of a subset of IOP data collected from a cruise in April-May 1997 over the North Atlantic Shelf (CMO97). This data set is independent in time (9 months later than the CMO96 cruise data) but was collected from the same site as the CMO96 site, which was used in deriving the global relationships. While thus not a fully independent data set, it can give insight into the degree to which local or regional IOP relationships differ from the global. It may also indicate which of the IOPs are more predictable or consistent on a global basis. Note that the range of each of the IOP values at 488 nm is much less than the

global and is also reduced from the CMO96 data set (Table 2.2). We have omitted spectral data plots (i.e., Figure 2.1) for the CMO97 data in order to conserve space. The r^2 values from each of the IOP regressions are given in Table 2.11.

Information on the slopes and y intercepts are discussed below.

Results from the regressions of the a_g data from the CMO97 data were, in general, comparable to the global data set. The exponential spectral slope S was estimated to be 0.014, slightly lower than the slope determined from the global a_g data set (0.015 to 0.016). Note however, that the r^2 values are greatly reduced from the global data set regressions. As was the case with the other IOP parameters, this is due to the much narrower range of concentrations at each wavelength in the CMO97 data set as compared to the global data set.

Table 2.11. R^2 values returned from the linear regressions of the CMO97 data set.

λ , nm	c_{pg}	a_{pg}	a_g	a_p	b_p
412	0.960	0.191	0.266	0.455	0.976
440	0.983	0.801	0.446	0.784	0.977
510	0.989	0.756	0.591	0.760	0.978
532	0.986	0.683	0.465	0.740	0.971
555	0.980	0.504	0.359	0.565	0.958
650	0.954	0.676	0.052	0.730	0.928
676	0.947	0.761	...	0.797	0.944

Regressions of the a_p and a_{pg} show similar trends in comparison with the global data set regressions. The slopes are lower at all wavelengths, with the

exception of 650 nm where they are approximately the same as the global slope (Figures 2.3 and 2.6). The y intercepts from the a_p and a_{pg} regressions of the CMO97 data set are comparable to the global data set at wavelengths greater than 488 nm (Figures 2.4 and 2.8). The y intercepts less than 488 nm are larger than the global data set, especially at 412. Also note that r^2 values from the CMO97 absorption regressions are the lowest at these wavelengths. The shape of the spectrum is also varied from the global, with a much steeper increase from 412 to 440 nm. Thus using the linear models derived from the global data set to predict the spectral absorption of the CMO97 data set would lead to an overestimate of the absorption at all wavelengths.

The spectral shape of the CMO97 b_p regression slopes is nearly flat, similar to the shape of the global data set regression slopes (Figure 2.10). The greatest differences between the global and CMO97 b_p regressions are at 650 and 676 nm, with the CMO97 data set showing higher slopes and the largest reduction in r^2 values. In the case of the b_p data, using the global models of b_p to predict the spectral values of the CMO97, would lead to an underestimate of the b_p at 650 and 676 nm.

The spectrum of the c_{pg} regression slopes is nearly flat for the CMO97 data set (Figure 2.12). In comparison with the global data set, the regression slopes are lower at wavelengths less than 488 nm and greater at wavelengths greater than 488 nm. The largest differences between the global and CMO97 data set regressions are at 650 and 676 nm, with the CMO97 slopes being larger and the r^2 values

greatly reduced. The biases (y intercepts) are also larger for the CMO97 data set spectrally (Figure 2.13). Using the global models to predict the c_{pg} spectrum would therefore overestimate the values at wavelengths less than 488 nm, and underestimate the values at wavelengths greater than 488 nm.

2.5 SUMMARY

We have produced a large data set of IOP from data collected from a wide variety of oceanic and coastal environments. It should be stressed that the results from this study not only span various water types but also cover the entire water column. One of the most significant results of this study is that when considering a diversity of oceanic and coastal environments, there are global relationships in the IOP spectra that are strikingly linear. These global relationships can be explained by noting that if the dynamic range is large, the deviation from a linear relationship can be relatively large without significantly affecting the overall variance. For a local data set, when the dynamic range is small, deviations from the global linear trend do not have to be large to significantly affect the variance on these regional scales. While these global relationships are extremely useful in providing large time and space estimates of the IOP relationships, they may or may not be valid in predicting local scale IOP variability. In comparison with a regional data set with a smaller dynamic range (CMO97), the IOP relationships were considerably different from the global, especially in the case of the beam attenuation coefficient. Thus,

using the global models to predict the spectral IOP at the local or regional scale may lead to inaccurate estimates of the IOP spectral shape and magnitude.

The main conclusion of this research is that over a diversity of oceanic regimes, there are fundamental first-order relationships in the individual IOP spectra. This is logical from the standpoint that the constituents of the ocean; water, particles (including detrital and pigmented material), and dissolved organic matter, combine to determine the IOP spectral relationships. While the relative proportions of each of these constituents may vary from region to region, the variability in the spectral relationships of these constituents is much smaller than the dynamic range of the IOP concentrations observed over the global oceans.

The importance of the results from this study has various implications for use in deriving ocean color remote sensing algorithms. The linear global relationships of this study define a set of IOP basis vectors which can be used in these remote sensing inversion models that require some a priori information of the absorption spectra [*Morel*, 1988; *Carder et al.*, 1991; *Roesler and Perry*, 1995; *Hoge and Lyon*, 1996]. Prediction of the spectrum of IOP variables given absorption, attenuation or scattering at a single wavelength with a given degree of accuracy can provide a wealth of information based on inversions of the remotely sensed radiance. However, on regional spatial scales, the spectral IOP relationships may differ greatly from the global. It is these local or regional scale deviations that contain the information about the local physical/biological environments.

From an instrumental standpoint, the results of this study indicate that the ac-9 measurements are, in general, precise over a large magnitude range of IOP values. In each of the spectral IOP relationships, the biases (as indicated by the value of the y intercept) were nearly equivalent to the estimated accuracy of the ac-9 measurements. The largest biases observed were located at the endpoints of the measured spectrum (412 and 676 nm) and may be due, in part, to the large wavelength separation from the regression wavelength (488 nm). Other causes of these biases were proposed, such as non-covarying detrital and dissolved fractions. These effects are amplified, as noted in the regional data set comparison (CMO97), when the dynamic range of the IOP values is decreased.

2.6 REFERENCES

- Blough, N. V., O. C. Zafiriou, and J. Bonilla, Optical absorption spectra of waters from the Orinoco River outflow: Terrestrial input of colored organic matter to the Caribbean, *J. Geophys. Res.*, 98, 2271-2278, 1993.
- Bricaud, A., and D. Stramski, Spectral absorption coefficients of living phytoplankton and nonalgal biogenous matter: A comparison between the Peru upwelling area and the Sargasso Sea, *Limnol. Oceanogr.*, 33, 562-582, 1990.
- Bricaud, A., A. Morel, and L. Prieur, Absorption by dissolved organic matter of the sea (yellow substance) in the UV and visible domains, *Limnol. Oceanogr.*, 26, 43-53, 1981.
- Bricaud, A., C. Roesler, and J. R. V. Zaneveld, *In situ* methods for measuring the inherent optical properties of ocean waters, *Limnol. Oceanogr.*, 40, 393-410, 1995a.

- Bricaud, A., M. Babin, A. Morel, and H. Claustre, Variability in the chlorophyll-specific absorption coefficients of natural phytoplankton: Analysis and parameterization, *J. Geophys. Res.*, 100, 13,321-13,332, 1995b.
- Carder, K. L., G. R. Harvey, and P. B. Ortner, Marine humic and fulvic acids: Their effects on remote sensing of ocean chlorophyll, *Limnol. Oceanogr.*, 34, 68-81, 1989.
- Carder, K. L., S. K. Hawes, K. S. Baker, R. C. Smith, R. G. Steward, and B. G. Mitchell, Reflectance model for quantifying chlorophyll *a* in the presence of productivity degradation products, *J. Geophys. Res.*, 96, 20,599-20,611, 1991.
- Gordon, H. R., Absorption and scattering estimates from irradiance measurements: Monte Carlo simulations, *Limnol. Oceanogr.*, 36, 769-777, 1991.
- Gordon, H. R., O. B. Brown, R. H. Evans, J. W. Brown, R. C. Smith, K. S. Baker, and D. K. Clark, A semianalytic radiance model of ocean color, *J. Geophys. Res.*, 93, 10,909-10,924, 1988.
- Hoepffner, N., and S. Sathyendranath, Determination of the major groups of phytoplankton pigments from the absorption spectra of total particulate matter, *J. Geophys. Res.*, 98, 22,789-22,803, 1993.
- Hoge, F. E. and P. E. Lyon, Satellite retrieval of inherent optical properties by linear matrix inversion of oceanic radiance models: An analysis of model and radiance measurement errors, *J. Geophys. Res.*, 101, 16,631-16,648, 1996.
- Hoge, F. E., A. Vodacek, and N. V. Blough, Inherent optical properties of the ocean: Retrieval of the absorption coefficient of chromophoric dissolved organic matter from fluorescence measurements, *Limnol. Oceanogr.*, 38, 1394-1402, 1993.
- Kirk, J. T. O., Estimation of the absorption and the scattering coefficients of natural waters by use of the underwater irradiance measurements, *Appl. Opt.*, 33, 3276-3278, 1994.
- Kishino, M., M. Takahashi, N. Okami, and S. Ichimura, Estimation of the spectral absorption coefficients of phytoplankton in the sea, *Bull. Mar. Sci.*, 37, 634-642, 1985.

- Lee, Z. P., K. L. Carder, S. K. Hawes, R. G. Steward, T. G. Peacock, and C. O. Davis, Model for the interpretation of hyperspectral remote-sensing reflectance, *Appl. Opt.*, 33, 5721-5732, 1994.
- Lee, Z. P., K. L. Carder, T. G. Peacock, C. O. Davis, and J. L. Mueller, Method to derive ocean absorption coefficients from remote-sensing reflectance, *Appl. Opt.*, 35, 453-462, 1996.
- Mitchell, B. G., Algorithms for determining the absorption coefficient of aquatic particulates using quantitative filter technique (QFT), Ocean Optics 10, *Proc. SPIE Int. Soc. Opt. Eng.*, 1302, 137-148, 1990.
- Mitchell, B. G. and D. A. Kiefer, Chlorophyll *a* specific absorption and fluorescence excitation spectra for light limited phytoplankton, *Deep Sea Res., Part A*, 35, 639-664, 1988a.
- Mitchell, B. G. and D. A. Kiefer, Variability in pigment specific particulate fluorescence and absorption spectra in the northeastern Pacific Ocean, *Deep Sea Res., Part A*, 35, 665-689, 1988b.
- Moore, C., J. R. V. Zaneveld, and J. C. Kitchen, Preliminary results from an *in situ* spectral absorption meter, Ocean Optics 11, *Proc. SPIE Int. Soc. Opt. Eng.*, 1750, 330-337, 1992.
- Moore, C., E. J. Bruce, W. S. Pegau, and A. D. Weidemann, WET Labs ac-9: Field calibration protocol, deployment techniques, data processing, and design improvements, Ocean Optics 13, *Proc. SPIE Int. Soc. Opt. Eng.*, 2963, 725-730, 1996.
- Morel, A., Optical modeling of the upper ocean in relation to its biogenous matter content (case I waters), *J. Geophys. Res.*, 93, 10,749-10,768, 1988.
- Morrow, J. H., W. S. Chamberlin, and D. A. Kiefer, A two-component description of spectral absorption by marine particles, *Limnol. Oceanogr.*, 34, 1500-1509, 1989.
- Pak, H., D. A. Kiefer, and J. C. Kitchen, Meridional variations in the concentration of chlorophyll and micro-particles in the North Pacific Ocean, *Deep-Sea Res., Part A*, 35, 1151-1171, 1988.
- Pegau, W. S., D. Gray, and J. R. V. Zaneveld, Absorption of visible and near-infrared light in water: the dependence on temperature and salinity, *Appl. Opt.*, 36, 6035-6046, 1997.

- Petzold, T. and R. Austin, An underwater transmissometer for ocean survey work, in Underwater photo-optical instrument applications, *Proc. SPIE Int. Soc. Eng.*, 12, 133-137, 1968.
- Preisendorfer, R. W., *Hydrologic Optics*, vol. 6, U.S. Department of Commer., Washington, D. C., 1976.
- Prieur, L., and S. Sathyendranath, An optical classification of coastal and oceanic waters based on the specific absorption curves of phytoplankton pigments, dissolved organic matter, and other particulate materials, *Limnol. Oceanogr.*, 26, 671-687, 1981.
- Roesler, C. S. and M. J. Perry, In situ phytoplankton absorption, fluorescence emission, and particulate backscattering spectra determined from reflectance, *J. Geophys. Res.*, 100, 13,279-13,294, 1995.
- Roesler, C. S. and J. R. V. Zaneveld, High resolution vertical profiles of spectral absorption, attenuation, and scattering coefficients in highly stratified waters, *Ocean Optics 12, Proc. SPIE Int. Soc. Opt. Eng.*, 2258, 309-318, 1994.
- Roesler, C. S., M. J. Perry, and K. L. Carder, Modeling *in situ* phytoplankton absorption from total absorption spectra in productive inland marine waters, *Limnol. Oceanogr.*, 34, 1510-1523, 1989.
- Sathyendranath, S., L. Lazzara, and L. Prieur, Variations in the spectral values of the specific absorption of phytoplankton, *Limnol. Oceanogr.*, 32, 403-415, 1989.
- Trüper, H. G. and C. S. Yentsch, Use of glass fiber filters for the rapid preparation of *in vivo* absorption spectra of photosynthetic bacteria, *J. Bacteriol.*, 94, 1255-1256, 1967.
- Twardowski, M. S., J. M. Sullivan, P. L. Donaghay, and J. R. V. Zaneveld, Quantification of the micro- to finescale *in situ* chromophoric DOM absorption and total absorption in coastal waters with an ac-9, *J. Atmo. Ocean. Tech.*, 16, 691-707, 1999.
- Voss, K. J., A spectral model of the beam attenuation coefficient in the ocean and coastal areas, *Limnol. Oceanogr.*, 37, 501-509, 1992.

- Zaneveld, J. R. V., An asymptotic closure theory for irradiance in the sea and its inversion to obtain the inherent optical properties, *Limnol. Oceanogr.*, 34, 1442-1452, 1989.
- Zaneveld, J. R. V., and J. C. Kitchen, The variation in the inherent optical properties of phytoplankton near an absorption peak as determined by various models of cell structure, *J. Geophys. Res.*, 100, 13,309-13,320, 1995.
- Zaneveld, J. R. V., J. C. Kitchen, A. Bricaud, and C. Moore, Analysis of *in situ* spectral absorption meter data, Ocean Optics 11, *Proc. SPIE Int. Soc. Opt. Eng.*, 1750, 180-186, 1992.
- Zaneveld, J. R. V., J. C. Kitchen, and C. C. Moore, Scattering error correction of reflecting tube absorption meters, Ocean Optics 13, *Proc. SPIE Int. Soc. Opt. Eng.*, 2258, 44-55, 1994.

CHAPTER 3

IN SITU DETERMINATION OF THE REMOTELY SENSED REFLECTANCE
AND THE ABSORPTION COEFFICIENT: CLOSURE AND INVERSION

Andrew H. Barnard, J. Ronald V. Zaneveld, and W. Scott Pegau.

Published in *Applied Optics*, 38, 5108-5117, August 20, 1999. Copyright by the
Optical Society of America.

3.1 ABSTRACT

We tested closure between *in situ* radiometric and absorption coefficient measurements by using a nearly backscattering-independent remote-sensing reflectance model that employs the remote-sensing reflectance at three wavelengths. We show that only a small error is introduced into the closure model when the proper functional relationships of f/Q and the backscattering is taken to be a constant when using the sea-viewing wide field-of-view sensor wavelengths 443, 490, and 555 nm. A method of inverting the model to obtain the absorption coefficient by use of simple linear spectral relationships of the absorption coefficient is provided. The results of the model show that the independent measurements of reflectance and absorption obtain closure with a high degree of accuracy.

3.2 INTRODUCTION

The proliferation of advanced noninvasive instruments for the measurement of the in-water apparent and inherent optical properties of the oceans has increased over the past ten years. The intercomparison of these *in situ* measurements is important in the determination of optical closure and the scale problem [Pegau *et al.*, 1995a and b]. Resolution of these issues provides assurance that the small-scale inherent optical properties (IOP's) determined with flow-through devices can

be used in radiative transfer schemes to determine the apparent optical properties (AOP's) which are determined from daylight observations. In this paper we describe a method to test in-water measurements of remote-sensing reflectance and absorption for closure based on radiative transfer.

In recent years there has been a focused effort to derive new methods for the determination of the IOP's of the oceans from ocean color satellite measurements [Roesler and Perry, 1995; Lee *et al.*, 1996; Garver and Siegel, 1997]. This effort has been driven in part by an increased ability to measure the in-water optical properties more accurately and effectively, allowing for more-detailed studies of the optical property relationships. Correspondingly, there has been an increase in the development of ocean color satellites, with new ocean color sensors planned in the future in addition to the sea-viewing wide field-of-view sensor (SeaWiFS), which is currently operational. Thus we are now in a position where we are able to validate inversion using *in situ* data and satellite estimates. A key component to this validation is the issue of closure between the in-water measurements of reflectance and the IOP's.

However, most remote-sensing reflectance algorithms must make assumptions about the angular dependency of the underwater light field and the backscattering component, as these parameters are not easily measured or currently well understood. It is the purpose of this research to derive a model that greatly minimizes the influence of these parameters. We show that, by using two ratios with three different wavelengths of the remote-sensing reflectance, the influence of

the spectral dependency of the backscattering coefficient and the angular dependence of the underwater light field is greatly reduced. The ability of three-band reflectance ratios to remove the angular dependency of the water-leaving radiance was originally noted by *Campbell and Esaias* [1983]. In this study we extend the results of their study to show utilizing reflectance ratios at three wavelengths also minimizes the spectral dependence of the backscattering coefficient.

3.3 THEORY AND APPROACH

3.3.1 Remote-Sensing Reflectance R_{rs}

The connection between the IOP's and the AOP's is through the equation of radiative transfer, which solves for the radiance distribution as a function of depth when the absorption and scattering properties of the seawater as well as the incident radiance distribution are known. The irradiance reflectance $R(\lambda)$, defined as the upwelling irradiance (E_u) normalized by the downwelling irradiance (E_d) just below the surface, is related to the absorption and backscattering coefficients as defined by *Preisendorfer* [1976]:

$$R(\lambda) = \frac{E_u(\lambda)}{E_d(\lambda)} = f(\lambda) \frac{b_b(\lambda)}{a(\lambda)} \quad (3.1)$$

where f is the parameter relating irradiance reflectance to the ratio of the backscattering b_b and absorption a coefficients radiance. However, as ocean color

satellites remotely sense the upwelled radiance, Equation (3.1) subsequently has been modified to look at the ratio of the upwelling radiance to the downwelling irradiance. This is most commonly known as the remote-sensing reflectance [Gordon *et al.*, 1988; Morel and Gentili, 1993] and is defined as

$$R_{rs}(\lambda) \equiv \frac{R(\lambda)}{Q(\lambda)} = \frac{L_u(\lambda)}{E_d(\lambda)} \approx \frac{f(\lambda) b_b(\lambda)}{Q(\lambda) a(\lambda)}, \quad (3.2)$$

where Q is the ratio of the upwelling irradiance and the nadir radiance.

Much discussion has been involved in determining the f/Q ratio, which depends on the shape of the upwelling light field and the volume-scattering function [Morel *et al.*, 1995; Morel and Gentili, 1996; Zaneveld, 1982]. Rather than having to approximate the value of this ratio, we want to formulate an expression for the remote-sensing reflectance, which depends solely on the IOP's of the water column.

3.3.2 f/Q Considerations

The f parameter, which depends on the shape of the light field and the volume-scattering function, is typically assumed to be equal to 0.33, although it has been shown to exhibit a total range of 0.25-0.55 for most oceanic environments [Morel and Gentili, 1993]. The Q factor, which is an indicator of the shape of the upwelling light field, can vary over an order of magnitude, with Q equal to π for a totally diffuse radiance distribution [Morel and Gentili, 1993]. However, Morel and Gentili [1993] found that f/Q is well behaved spectrally, with much of the

variation in f canceled by the fluctuation in Q . *Zaneveld* [1995] has also shown that the f parameter is directly proportional to Q , and that unless there is significant multiple scattering, the dependence of L_w/E_d on Q is weak over most remote-sensing angles. These observations can be used to derive a function that significantly reduces the contribution of the f/Q ratio.

By utilizing two ratios of R_{rs} at three wavelengths, we can derive the following equation:

$$R_{rs3}(\lambda_1, \lambda_2, \lambda_3) = \frac{R_{rs}(\lambda_1)/R_{rs}(\lambda_2)}{R_{rs}(\lambda_2)/R_{rs}(\lambda_3)} \cong \frac{\frac{f}{Q}(\lambda_1)\frac{f}{Q}(\lambda_3)\frac{b_b}{a}(\lambda_1)\frac{b_b}{a}(\lambda_3)}{\left[\frac{f}{Q}(\lambda_2)\right]^2\left[\frac{b_b}{a}(\lambda_2)\right]^2}. \quad (3.3)$$

Based on Monte Carlo simulations for nadir radiance, solar zenith angle of 30.0° , and a chlorophyll concentration of 0.1 mg m^{-3} , *Morel and Gentili* [1993] computed the f/Q values to be approximately 0.089, 0.088, and 0.0875 for the wavelengths 443, 490, and 555 nm (see their Figure 5). The triple ratio of the f/Q parameter by use of these wavelengths is approximately 1.006. Thus, if the spectral behavior of f/Q is linear or nearly so, and the center wavelength (λ_2) is nearly equally spaced between the other two, one can show that only a small error is induced by assuming that the triple ratio of f/Q is equal to one. Given the Q -like behavior of f , and the weak wavelength dependence of f/Q , we assume the f/Q triple ratio in Equation (3.3) to be a constant equal to one, reducing Equation (3.3) to

$$R_{rs3}(\lambda_1, \lambda_2, \lambda_3) = \frac{R_{rs}(\lambda_1)}{R_{rs}(\lambda_2)} \bigg/ \frac{R_{rs}(\lambda_2)}{R_{rs}(\lambda_3)} \cong \frac{\frac{b_b(\lambda_1)b_b(\lambda_3)}{a}}{\left[\frac{b_b(\lambda_2)}{a}\right]^2}. \quad (3.4)$$

If we assume that the remotely sensed portion of the water column is homogeneous, i.e. that the IOP's are homogeneously distributed over the remote-sensing depth, we can separate the backscattering and absorption components such that

$$R_{rs3}(\lambda_1, \lambda_2, \lambda_3) = \frac{R_{rs}(\lambda_1)}{R_{rs}(\lambda_2)} \bigg/ \frac{R_{rs}(\lambda_2)}{R_{rs}(\lambda_3)} \cong \frac{b_b(\lambda_1)b_b(\lambda_3)}{b_b^2(\lambda_2)} \frac{a^2(\lambda_2)}{a(\lambda_1)a(\lambda_3)}. \quad (3.5)$$

We now have derived an equation for a remotely sensed reflectance parameter R_{rs3} purely in terms of the backscattering and the absorption coefficients by assuming a weak spectral dependence of f/Q and a homogeneous vertical distribution of the IOP's over the remote-sensing depth.

3.3.3 Backscattering Component

The scattering parameter that is relevant to the remotely sensed radiance is not simply the backscattering coefficient, but rather a weighted integral of the volume-scattering function in the backward direction [*Gordon et al*, 1988; *Zaneveld*, 1995]. This function cannot be measured easily at present. Furthermore the angular distribution of the backscattering coefficient is not well known at this time. Thus it is of interest to derive an equation for the remote-sensing reflectance that is nearly independent of the backscattering coefficient. In the text below we

examine the spectral dependence of the backscattering triple ratio. For simplification in what follows we set

$$b_{br3} = b_{br3}(\lambda_1, \lambda_2, \lambda_3) = \frac{b_b(\lambda_1)b_b(\lambda_3)}{b_b^2(\lambda_2)}. \quad (3.6)$$

The backscattering coefficient depends on the water and its particulate components, such that

$$b_b(\lambda) = b_{bw}(\lambda) + b_{bp}(\lambda), \quad (3.7)$$

where b_{bw} is the backscattering coefficient of water and b_{bp} is the backscattering coefficient of particles. The backscattering coefficient of water has a $\lambda^{-4.32}$ spectral dependence [Morel, 1974], whereas a $\lambda^{-\eta}$ spectral dependence is typically assumed for the backscattering by particles [Morel and Prieur, 1977; Smith and Baker, 1981; Bricaud et al., 1983; Ahn et al., 1992; Stramski and Kiefer, 1991]. Thus

$$b_{bw}(\lambda) = b_{bw}(\lambda_r) \left(\frac{\lambda}{\lambda_r} \right)^{-4.32}, \quad b_{bp}(\lambda) = b_{bp}(\lambda_r) \left(\frac{\lambda}{\lambda_r} \right)^{-\eta}, \quad (3.8)$$

where λ_r is a reference wavelength. Substituting Equations (3.8) into Equation (3.6), and taking λ_2 as the reference wavelength, we can rewrite the triple backscattering ratio in the following manner:

$$b_{br3} = \frac{\left[b_{bw}(\lambda_2) \left(\frac{\lambda_1}{\lambda_2} \right)^{-4.32} + b_{bp}(\lambda_2) \left(\frac{\lambda_1}{\lambda_2} \right)^{-\eta} \right] \left[b_{bw}(\lambda_2) \left(\frac{\lambda_3}{\lambda_2} \right)^{-4.32} + b_{bp}(\lambda_2) \left(\frac{\lambda_3}{\lambda_2} \right)^{-\eta} \right]}{\left[b_{bw}(\lambda_2) + b_{bp}(\lambda_2) \right]^2}. \quad (3.9)$$

For simplification in what follows we set $b_{bw} = b_{bw}(\lambda_2)$, and $b_{bp} = b_{bp}(\lambda_2)$ as the wavelength dependence has been eliminated. Equation (3.9) can then be reduced to

$$b_{br3} = \frac{\left(\frac{b_{bw}}{b_{bp}}\right)^2 \left(\frac{\lambda_1 \lambda_3}{\lambda_2^2}\right)^{-4.32} + \frac{b_{bw}}{b_{bp}} \left[\left(\frac{\lambda_1}{\lambda_2}\right)^{-4.32} \left(\frac{\lambda_3}{\lambda_2}\right)^{-\eta} + \left(\frac{\lambda_1}{\lambda_2}\right)^{-\eta} \left(\frac{\lambda_3}{\lambda_2}\right)^{-4.32} \right] + \left(\frac{\lambda_1 \lambda_3}{\lambda_2^2}\right)^{-\eta}}{\left(\frac{b_{bw}}{b_{bp}} + 1\right)^2}. \quad (3.10)$$

Equation (3.10) can be evaluated for typical oceanic situations, where b_b ranges from particle-dominated backscattering to water dominated, $0 \leq b_{bw}/b_{bp} \leq 2.5$, and where the spectral scattering dependency varies from $0 \leq \eta \leq 2$.

In practice, the choice of λ_1 , λ_2 , and λ_3 depends on the wavelengths that are available on *in situ* and satellite sensors. For the purposes of this paper we will examine the 443-, 490-, and 555-nm wavelengths, as *in situ* reflectance and IOP's are commonly measured at these wavelengths and are also available on the SeaWiFS ocean color satellite. Figure 3.1 shows the dependence of b_{br3} on η and b_{bw}/b_{bp} calculated with $\lambda_1 = 443$, $\lambda_2 = 490$, and $\lambda_3 = 555$ nm in Equation (3.10). The value of b_{br3} ranges from 0.93 to 1.02, with the greatest variation in b_{br3} with η occurring when the backscattering by particles is greater than the water backscattering (i.e., $b_{bw}/b_{bp} < 1.0$). When one chooses a constant value for b_{br3} nominally equal to 0.975, an error of maximally 4.5% is made for most realistic ocean water types. This error is well within the typical error bars for the *in situ* determination of remote-sensing reflectance and the absorption coefficient. It can thus be seen that for all practical purposes, b_{br3} can be considered to be a constant when the 443-, 490-, and 555-nm wavelengths are considered. Note that in the

formulation of the backscattering triple ratio, no additional assumptions were made as to the type or size distribution of the particles. As one can readily see from

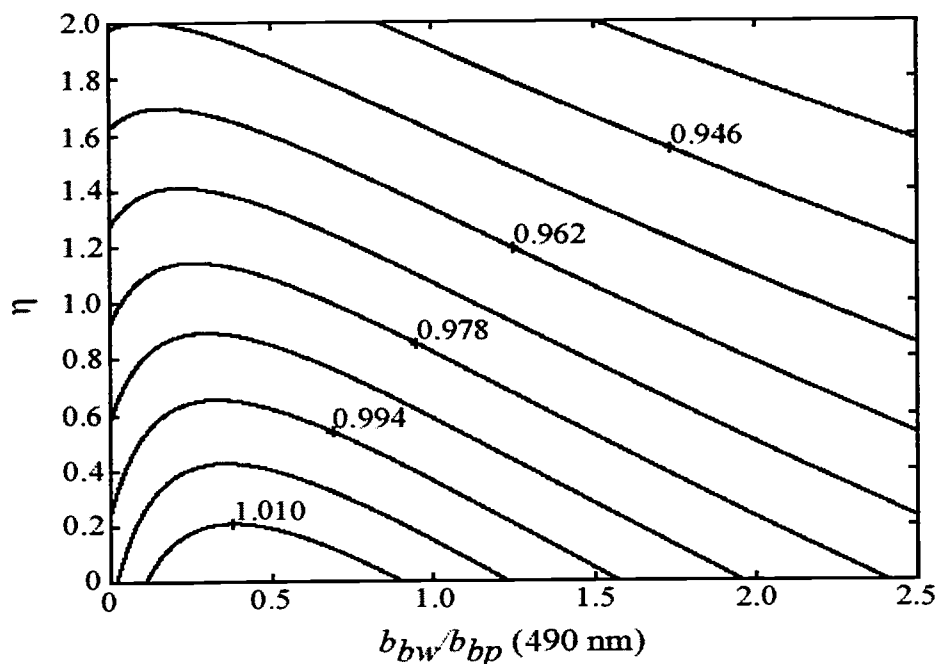


Figure 3.1. Contour of the backscattering triple ratio b_{br3} as a function of the shape of the particle backscattering η and the water-to-particle backscattering ratio at 490 nm (b_{bw}/b_{bp}), computed with Eq. (3.9) and the wavelengths 443, 490, and 555 nm.

Figure 3.1, fluctuations in the backscattering coefficient that are due to variations in the spectral shape and magnitude are greatly reduced in the triple ratio expression.

The value of b_{br3} in Equation (3.10) could be computed with *in situ* measurements of the backscattering coefficient. However, such devices are only

recently being developed [Maffione and Dana, 1997]. To evaluate the accuracy of the above simplifications, we computed the value of b_{br3} by modeling the backscattering coefficient based on the in-water profiles of the particulate scattering coefficient b_p . We modeled the profiles of total backscattering at each wavelength as

$$b_b(\lambda, z) = b_{bp}(\lambda, z) + b_{bw}(\lambda) \cong \tilde{b}_b b_p(\lambda, z) + 0.5b_w(\lambda), \quad (3.11)$$

where \tilde{b}_b is the probability of the particle backscattering and b_w is the scattering coefficient for pure water. The value of the \tilde{b}_b parameter has been modeled by others based on various assumptions. In a model by Morel [1988] for case I waters, \tilde{b}_b decreased logarithmically from 2.2% in low-chlorophyll, oligotrophic waters to 0.2% in high-chlorophyll, eutrophic waters. In a similar model by Gordon *et al.* [1988], the particle backscattering probability varied from 2% in low-chlorophyll waters to 0.5% in high-chlorophyll waters. Ahn *et al.* [1992], using monocultures of algae, indicated that the spectral dependence of the backscattering probability is a function of cell size and pigmentation of the individual species and, for the species they studied, was always less than 0.5%. As the data set used in this study is typically somewhere between oligotrophic to eutrophic oceanic environments (see Section 3.4), we chose a value of $\tilde{b}_b = 1\%$. Although we expect that the spectral dependence of \tilde{b}_b will depend on algal concentration and size distribution, to a first approximation we assume that there is no spectral dependence over the wavelength range used in this study. Thus in this method we assume a spectral

dependence and, to some extent, a particle type and size distribution by choosing a constant \tilde{b}_b value.

3.3.4 Closure

Substituting the above formulations of the backscattering component b_{br3} we can now replace Equation (3.5) by

$$R_{rs3}(\lambda_1, \lambda_2, \lambda_3) \cong b_{br3} \frac{a^2(\lambda_2)}{a(\lambda_1)a(\lambda_3)}. \quad (3.12)$$

Given nearly simultaneous profiles of the upwelling radiance, downwelling irradiance, and the total absorption, relation (3.12) can be tested for closure with the above assumptions. This model thus allows for the direct comparison (and prediction) of a radiometric quantity R_{rs3} with an IOP, the absorption triple ratio. Testing the equivalency of these expressions is the major purpose of this paper.

3.3.5 Inversion

Clearly if relation (3.12) is correct to within acceptable limits, and b_{br3} is set to a constant, the remote-sensing reflectance spectrum can be used to determine the triple ratio of the absorption coefficient. If for a given region or time period there exist functional relationships between the absorption at these three wavelengths, so that $a(\lambda_1) = f_1[a(\lambda_2)]$ and $a(\lambda_3) = f_3[a(\lambda_2)]$, we can then set

$$R_{rs3}(\lambda_1, \lambda_2, \lambda_3) \cong b_{br3} \frac{a^2(\lambda_2)}{f_1[a(\lambda_2)]f_3[a(\lambda_2)]}. \quad (3.13)$$

In this formulation, triple reflectance ratio is expressed as function of $a(\lambda_2)$ only.

Provided that regional or global relationships between $a(\lambda_1)$, $a(\lambda_2)$ and $a(\lambda_3)$ can be found, we can use relation (3.13) to invert R_{rs3} to determine the absorption coefficient at λ_2 .

Any functional form for the spectral absorption coefficient can be utilized in relation (3.13), including separating the absorption coefficient into its respective components (i.e., water, particles, yellow matter). Most semianalytical remote-sensing algorithms provide for these functional relationships in terms of the individual components of the absorption coefficient [*Roesler and Perry, 1995; Lee et al., 1996; Garver and Siegel, 1997*]. However, our interest is not in determining the most accurate method of inversion, but rather to demonstrate how this algorithm minimizes the uncertainty involved in estimating the parameters that are most difficult to measure, namely the f/Q and the b_b component. Therefore in this paper we present simplistic absorption coefficient functionalities to provide an example of how the model can be used for inversion to obtain the spectral absorption coefficient.

In a recent paper by *Barnard et al. [1998]* it was shown that over a wide range of oceanic environments, simple linear relationships exist between the 443- and 555-nm and the 490-nm absorption coefficients. However, in their paper the linear relationships of the absorption coefficient did not include the contribution by

pure water. If consistent linear relationships of the total absorption coefficient (including pure water) exist between these wavelengths from the 70 profiles used in this study, such that

$$\begin{aligned} f_1[a(490)] &= [a(443)] = A[a(490)] + B, \\ f_3[a(490)] &= [a(555)] = C[a(490)] + D, \end{aligned}$$

then we can substitute these functional forms into relation (3.13) and solve for the absorption coefficient at 490 nm. In this method, as opposed to the presentation given in *Barnard et al.* [1998], we include the offsets B and D in our models to account for the spectral dependence of the absorption coefficient by pure water. Again, we emphasize that simplistic linear functionalities are not likely to be the most accurate way of modeling the spectral absorption coefficient, especially when considering regionalized data sets. However, for our purposes, we utilize them to demonstrate how relation (13) can be used to invert the remotely sensed radiance. Also, substitution of these simple linear models into relation (3.13) produces the following quadratic equation for the absorption coefficient at 490 nm, which can be solved easily for given *in situ* measurements of the remotely sensed reflectance:

$$a(490) = \frac{-(AD + BC) \pm \left[(AD + BC)^2 - 4 \left(AC - \frac{b_{br3}}{R_{rs3}} \right) (BD) \right]^{1/2}}{2 \left(AC - \frac{b_{br3}}{R_{rs3}} \right)}. \quad (3.14)$$

3.4 DATA AND MEASUREMENTS

3.4.1 Data Sets

Data from six separate research cruises were used to test relation (3.12) for closure. Four research cruises were carried out in the Gulf of California during the fall of 1995, 1996, and 1997 and the spring of 1998. Optical property data were also collected during the coastal mixing and optics experiment off the Northeast Atlantic Shelf during the fall of 1996 and the spring of 1997. IOP profiles on all cruises were collected by use of the slow descent rate optics platform. This platform typically carries two spectral absorption and attenuation meters, a CTD, and a WET Labs, Inc. modular ocean data and power system to integrate the data streams. Profiles of E_d and L_u and the IOP made within 120 minutes of each other were selected to minimize temporal and horizontal translation. From these six cruises, 70 temporally and spatially varying profiles of E_d , L_u , and the IOP were used to test relation (3.12) for closure. The locations and dates for each data set are shown in Table 3.1.

Table 3.1. Data set locations and dates consisting of 70 IOP and AOP profiles^a.

Location Description	Date Range	Latitude (°N) Range	Longitude (°W) Range	Number of Profiles
Gulf of California	1-3 Dec. 1995	27.69-27.95	110.96-111.40	6
	31 Oct.-7 Nov. 1996	26.81-28.11	110.13-112.11	18
	16-29 Oct. 1997	24.82-30.22	109.50-114.28	11
	6-16 Mar. 1998	25.57-31.13	110.57-114.52	8
Northeast Atlantic Shelf	18 Aug.-6 Sept. 1996	40.33-40.52	70.47-70.52	23
	26-30 Apr. 1997	40.5	70.49	4

^aProfiles are separated by less than 120 min.

3.4.2 Remote-Sensing Reflectance

We measured profiles of spectral E_d and L_u during both the coastal mixing and the optics experiment cruises and during the 1996 Gulf of California cruise by using a Satlantic SeaWiFS Profiling Multichannel Radiometer (SPMR). A Biospherical profiling reflectance radiometer (PRR-600) was used to collect the irradiance and radiance data during the 1995, 1997, and 1998 Gulf of California cruises. The SPMR and the profiling reflectance radiometer measure downwelling irradiance and upwelling radiance at seven wavelengths. For this study the wavelengths of interest are 443, 490, and 555 nm. The remotely sensed reflectance was computed from the profiles of E_d and L_u as in Equation (3.2).

3.4.3 Inherent Optical Properties

We made profiles of the IOP by using a WET Labs, Inc. ac-9 meter, which measures the absorption and beam attenuation coefficients at nine wavelengths. Details on the calibration, deployment, and processing procedures of the absorption data are provided in *Barnard et al.* [1998], *Twardowski et al.* [1999] and WET Labs, Inc. (www.wetlabs.com). The absorption coefficients for pure water [*Pope and Fry*, 1997] were added to the ac-9 measurements to derive the total absorption coefficient. The particulate scattering coefficient was derived from the difference of the beam attenuation and absorption coefficient measurements. The scattering coefficients for pure water utilized in Equation (11) were obtained from *Morel* [1974]. The wavelengths of interest in this study are the 440-, 488-, and 555-nm bands. Because the ac-9 absorption measurements are determined by use of filters with a 10-nm bandwidth, we assume that these wavelengths are sufficiently similar to the irradiance and radiance wavelengths for comparison.

3.4.4 Optical Weighting of Profiles

Both the IOP and the E_d and L_u data were binned to 1-m resolution. Because we are interested in determining if the model achieves closure, we have made no effort to extrapolate the radiance and irradiance measurements to just above the sea surface (i.e., 0+). Instead, we computed R_{rs} at the shallowest radiance or irradiance measurement, and then correspondingly adjusted the IOP profiles such

that the E_d , L_u , and IOP profiles are measured over the same depth range. One good reason for doing this is to avoid the possible uncertainty involved in extrapolating the irradiance and radiance measurements to the surface.

To test the model for closure, we must first address the issue of scales. In Equation (3.2) the remote-sensing reflectance was defined to be the ratio of the upwelling radiance to the downwelling irradiance as a function of depth. Therefore the right-hand side of Equation (3.2) must be integrated such that it represents an optically weighted absorption measurement for the same water column. We follow the method presented by *Zaneveld and Pegau [1998]*, in which the water column is divided into N layers, the optical properties in each layer are homogeneous, and each layer has a light attenuation coefficient H_n that describes the round-trip attenuation of the upwelling and downwelling irradiance through the layer. For each of the corresponding profiles, we computed the optically weighted total absorption coefficient at each of the three wavelengths using

$$\langle a \rangle = \frac{\sum_{n=1}^N H_n a_n}{\sum_{n=1}^N H_n}, \text{ with } H_n = \frac{L_{u_{n-1}} E_{d_{n-1}} - L_{u_n} E_{d_n}}{L_{u_{n_0}} E_{d_{n_0}}}. \quad (3.15)$$

In our convention, each n layer is 1 m thick, a_n is the average absorption coefficient within each 1-m-thick layer, and L_{u_n} and E_{d_n} are the upwelling radiance and downwelling irradiance at the bottom of the each 1-m layer. The subscript 0 is the shallowest AOP sample depth for a given profile. The depth of the 90% light

attenuation level at a given wavelength was used as the bottom of the last layer ($n=N$) for each profile. The modeled profiles of the backscattering coefficient were optically weighted in the same manner as the absorption coefficient.

3.5 RESULTS

3.5.1 *In situ* Measurement Closure: Constant b_{br3} Case

Figure 3.2 shows R_{rs3} versus the triple ratio of the absorption coefficient for the 70 profiles used in this study. Assuming that there are no biases in the model, then the slope of the linear regression of this data would indicate the mean value of b_{br3} for these 70 profiles. The results indicate that the model does achieve closure with a $R^2 = 0.928$, and a standard error of 0.051. The 95% confidence interval on the y intercept of the regression (0.025 ± 0.046) indicates that it is not significantly different from zero. The slope of the linear regression is 0.985 with the 95% confidence interval of ± 0.067 . Based on the results given in Figure 3.1, this value for b_{br3} is well within the expected range. Given that the profiles of the absorption coefficient and R_{rs} were not made concurrently, we expect that the regression would not be perfect because of the temporal and spatial differences between the profiles. Also note that in testing the algorithm for closure, nine *in situ* measurements are used (three wavelengths each of upwelling radiance, downwelling irradiance and absorption). Inaccuracies in calibration of each of these measurements may significantly increase the error of the model, especially if the spectral shape of one

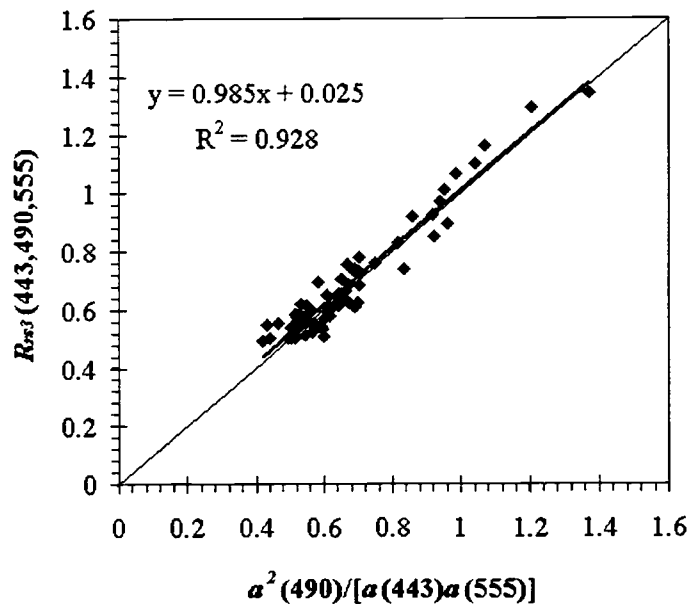


Figure 3.2. Triple ratio of the remote-sensing reflectance at 443, 490, and 555 nm determined from *in situ* radiometer measurements versus the triple ratio of the absorption coefficient at 443, 490, and 555 nm determined from *in situ* ac-9 measurements.

or more of these parameters is incorrect. Given the good relationship between R_{rs3} and the triple ratio of the absorption coefficient and that the slope of this relationship is well within the expected range of b_{br3} , we conclude that closure between the *in situ* determinations of R_{rs} and the absorption coefficient has been demonstrated.

3.5.2 Variable b_{br3} Comparison

Because we demonstrated closure between the *in situ* measurements of remotely sensed reflectance and the absorption coefficient using relation (3.12), it is of interest to examine the error associated with estimating the value of b_{br3} using *in situ* b_p measurements. In Figure 3.1 it was shown that the value of b_{br3} is between 0.93 and 1.02 for most oceanic environments. Recall that the spectral dependence of the backscattering coefficient by particles is known to range from λ^0 for most phytoplankton cells [Bricaud *et al.*, 1983; Ahn *et al.*, 1992] to λ^{-2} for the very small particles (0.2-0.5 μm) [Stramski and Kiefer, 1991]. Because our data set contains a mixture of both oceanic and near-coastal stations, a λ^{-1} dependence for the backscattering coefficient by particles was assumed.

In the 70 profiles used in this study, the scattering coefficient by particles at 490 nm ranges from 0.103 to 1.344 m^{-1} . Assuming that b_{bp} is 1% of b_p , then the observed range of b_{bw}/b_{bp} would be expected to range between 0.1 and 1.25. Thus from Figure 3.1 the value of b_{br3} for our data should range from approximately 0.95 to 1.02, with a center value near 0.985. The mean value for all 70 profiles of the b_{br3} ratio computed using the backscattering coefficient model in Equation (3.11) is 1.015 with a standard deviation of 0.027. The modeled backscattering b_{br3} values range from 0.96 to 1.08, with 41% of the values being greater than the highest expected value of b_{br3} (1.02). The possible causes for these high values of b_{br3} include an inaccurate choice for \tilde{b}_b (1%) and instrumental measurement errors of

the b_p . This emphasizes the difficulty in modeling the backscattering component. However, it is interesting to note that even with these possible errors, the difference between the value of b_{br3} returned from the regression shown in Figure 3.2 and in the modeled b_{br3} is only 0.03.

3.5.3 Inversion to Obtain the Absorption Coefficient

To invert relation (3.12) to obtain the absorption coefficient at 490 nm, we must provide for the spectral dependence of the absorption coefficient. Figure 3.3 shows the absorption coefficient at 490 nm for the 70 profiles used in this study versus the absorption coefficient at 443 and 555 nm. It is evident that simple linear relationships exist between the total absorption coefficient at 490 nm and at 443 and 555 nm, with the coefficient of variation equal to 0.98 and 0.60, respectively. The lower coefficient of variation at 555 nm is most likely due to narrow range of variability in the absorption at 555 nm as compared with the range observed at 490 nm. These functional relationships of the absorption coefficient were used to invert relation (3.13) to predict the absorption coefficient at 490 nm based on the measured remote-sensing reflectance, assuming a constant b_{br3} value of 0.985. Again, we emphasize that the functional form of these relationships does not necessarily require that they be linear, nor do we expect these relationships to be the most accurate models for the spectral absorption coefficient. However, using linear relationships greatly simplifies the inversion to obtain total absorption coefficient

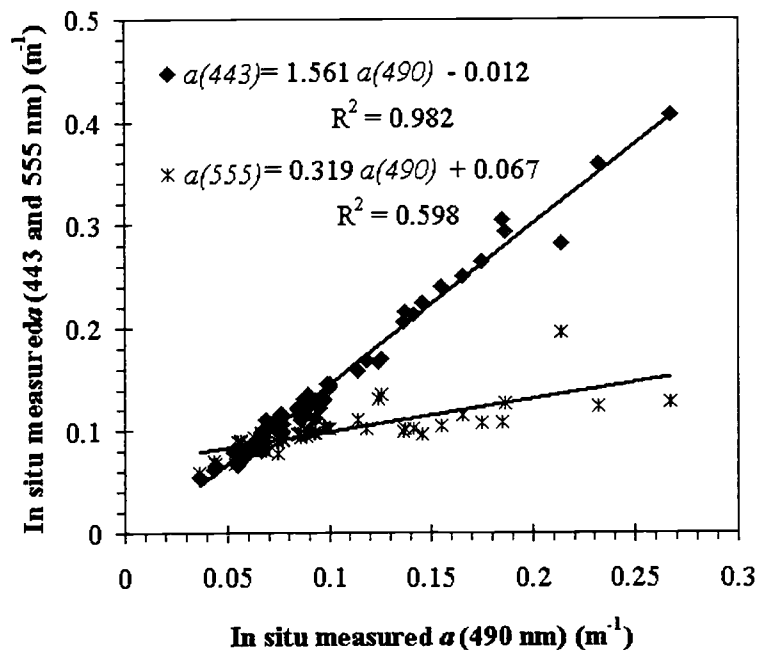


Figure 3.3. Optically weighted absorption coefficient at 490 nm versus the optically weighted absorption coefficient at 443 nm (filled diamonds) and 555 nm (asterisks) determined from ac-9 measurements. The linear regressions for each wavelength are also shown.

and provides an example of how relation (3.13) can be used for inversions.

Although this is not an independent test of the model because the functional relationships of the absorption coefficient were derived from the same data set used to test the model for closure, it can provide insight on the influence of b_{br3} on predicting the absorption coefficient.

The results of the inversion model in predicting the spectral absorption coefficient are plotted in Figure 3.4, with the associated statistics given in Table 3.2, and can be summarized as follows. The absorption coefficient at 443 and 490

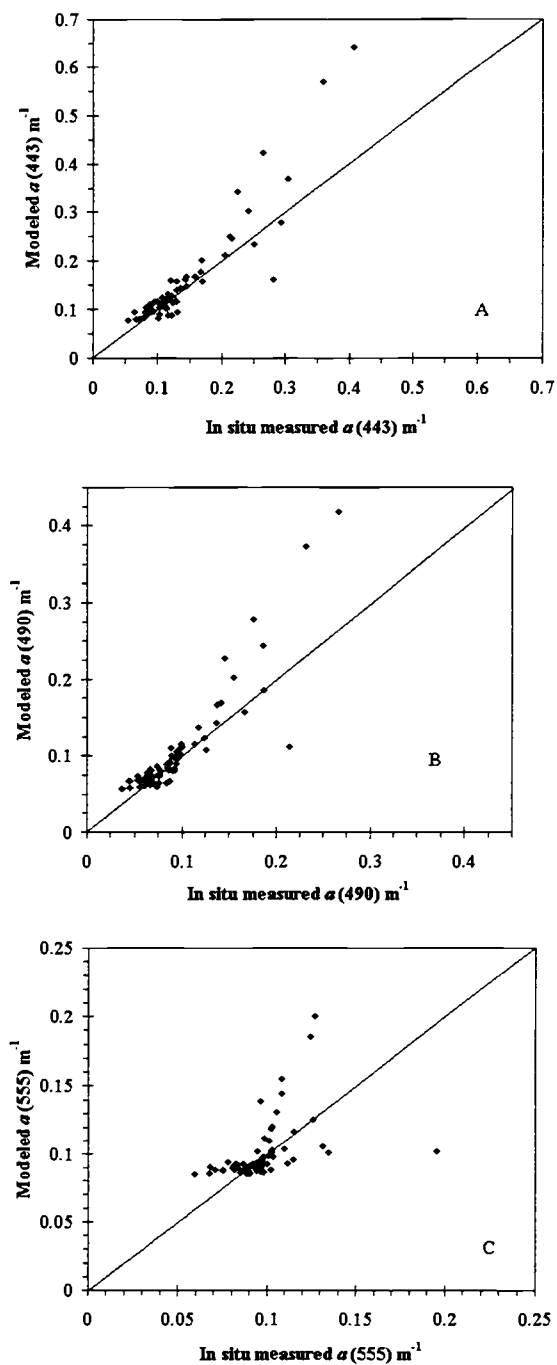


Figure 3.4. Predicted absorption coefficient at 443 (panel A), 490 (panel B), and 555 nm (panel C) based on the remote-sensing reflectance triple ratio and the absorption relationships at 443 and 555 nm (see Fig. 3.3 and Equation 14) versus the *in situ* measured absorption coefficient at each of the respective wavelengths.

Table 3.2. Regression results of the *in situ* measured and modeled absorption coefficients^a.

Predicted versus Measured Parameter	Slope	Offset	R^2	Standard Error	95% Confidence Limits	
					Slope	Offset
$a(490)$	1.336	-0.021	0.809	0.030	0.157	0.016
$a(443)$	1.359	-0.031	0.852	0.041	0.137	0.021
$a(555)$	0.538	0.048	0.222	0.019	0.246	0.024
Lee et al., [1998]						
$a(440)$ three-band	2.449	-0.136	0.794	0.090	0.301	0.049
$a(440)$ two-band	2.408	-0.132	0.818	0.082	0.274	0.042

^aComputed by use of the inversion of Eq. (3.14) and the relationships provided in Figure 3.2. Also shown are the regression results between *in situ* absorption coefficient and those predicted by use of three-band and two-band nonlinear remote-sensing reflectance models given by Lee *et al.*, [1998].

nm can be predicted reasonably well with a general tendency to overpredict the absorption values. However, the predictability of the 555-nm absorption coefficient is poor, which is most likely due to the uncertainty in the 555-490-nm absorption relationship (see Figure 3.2). The predictability of the absorption coefficient at all three wavelengths is lowest at the higher absorption coefficient values, where the predicted value can be as great as a factor of 2 different from the measured value.

In the paper by *Barnard et al.* [1998] it was noted that the linear relationships between the 443 and 555 nm and the absorption coefficient at 490 nm changes when the absorption coefficient at 490 nm is greater than 0.225 m^{-1} . The change in the relationships was found to occur when the absorption by particles dominated the absorption by dissolved materials. Indeed, in examining Figure 3.3 more closely, it can be seen that for absorption coefficients at 490 nm greater than

0.15 m^{-1} , the predicted values can be different from the measured ones by a factor of 2. Because our linear models of the spectral absorption coefficient do not provide for the change in the relationships with the increase in the absorption values, the error in the prediction of the absorption coefficient increases at these higher values. In fact, when considering absorption coefficients at 490 nm less than 0.15 m^{-1} , the model's ability to predict the absorption coefficient is improved (a standard error of 0.014 m^{-1}). These results emphasize that the major error in inversions to obtain the absorption coefficient is due to the assumption of the spectral dependencies of the absorption coefficient.

Linear relationships are obviously the simplest method to model the spectral dependence of the absorption coefficient. Use of more-sophisticated models that account for the individual components of the water (i.e., phytoplankton, detritus, and colored dissolved organic material) are likely to improve inversions. However, as mentioned above, our goal was not to determine the most accurate method of inverting the remotely sensed reflectance to obtain the absorption coefficient, but rather to minimize the error involved with estimating the parameters that are difficult to measure, namely, the f/Q and the b_b components.

Nevertheless, it is of interest to see how this inversion algorithm compares with other algorithms based on remotely sensed reflectance ratios. Two such algorithms are provided by *Lee et al.* [1998; see their Equations (3.14) and (3.16)] based on empirically derived nonlinear relationships between the absorption coefficient at 440 nm and a combination of the $R_{rs}(440/555)$ and $(490/555)$ ratios

and the $R_{rs}(490/555)$ ratio only. The *in situ* measurements of R_{rs} of the 70 profiles of in this study were used as inputs to the two models given in *Lee et al.* [1998]. The results show that both of these nonlinear models overpredict the absorption coefficient at 443 nm to a much greater extent than the simple linear models of this paper (Table 3.2) and show large biases. As was found in the predicted versus measured comparisons of our inversion models, the error in the prediction of the absorption coefficient at 443 nm based on these nonlinear models was the greatest at the higher values. These results emphasize that the highest errors associated with inversion are due to the uncertainties in the spectral dependence of the absorption coefficient.

3.6 DISCUSSION AND CONCLUSIONS

With the development of *in situ* spectrophotometers [*Moore et al.*, 1992; *Zaneveld et al.*, 1994] it is now possible to obtain absorption spectra with a high degree of accuracy (typically 0.005 m^{-1}). The accuracy of *in situ* absorption measurements and their use in radiative transfer studies and remote-sensing inversions is demonstrated in closure algorithms that compare absorption and reflectance values. We have provided a model that minimizes the dependence of the backscattering on the remote-sensing reflectance by using ratios of three wavelengths. It was shown that IOP data derived from ac-9 measurements was well correlated with the remote-sensing reflectance triple ratio from radiance and

irradiance data obtained using Satlantic and Biospherical radiometers. Closure between these disparate devices has thus been demonstrated, and we have shown that radiative transfer works to within instrument accuracy.

In applications where routine instrument calibrations are limited, such as mooring deployments, this algorithm provides a method that can be used to verify or intercalibrate *in situ* IOP and AOP measurements. Remote-sensing reflectance measurements are dependent on the geometry of the incoming light field, which often makes inter-comparison of AOP and IOP measurements difficult. Furthermore, the angular dependency of the backscattering coefficient is currently not well understood. The triple reflectance algorithm reduces the dependence of closure algorithms on the incoming light field and the backscattering coefficient, allowing for the intercalibration of *in situ* data that are to be used in studies of radiative transfer and remote-sensing inversions. Note that the triple reflectance algorithm is not limited to the three wavelengths used in this study. Any combination of the three wavelengths can be used provided that the spectral dependence of the backscattering coefficient of particles and the f/Q parameter is nearly linear over the wavelengths of interest. Inversion may also be possible provided the spectral dependence of the absorption coefficient can be modeled accurately.

Nearly all semianalytical inversions of the remotely sensed reflectance require *a priori* knowledge of the backscattering and absorption properties of the water as well as the shape of the *in situ* light field. These models typically assume

some spectral dependence of the backscattering and absorption coefficients as well as the shape of the underwater light field based on parameters such as the solar zenith angle, wind speed, and chlorophyll concentration. The focus of the current research is to minimize the number of assumptions or models needed in order to obtain closure between the measurements of the remotely sensed reflectance and the measured absorption coefficient. The major result of this paper is the theoretical and experimental demonstration of the equivalency of the radiometric property R_{rs3} and the IOP, the triple ratio of the absorption coefficient.

Other researchers have demonstrated the value of using reflectance ratios. *Campbell and Esaias* [1983] showed that use of a triple ratio of reflectance removed some of the extraneous variability in the water-leaving radiance by removing most of the dependence on geometry. In fact, the use of a triple ratio algorithm may also aid in removing errors associated with atmospheric correction, assuming they have nearly linear dependencies with wavelength. Our method shows utility in closure and in inversion and only assumes that the f/Q wavelength dependence is nearly linear and that the particle backscattering has a λ^{-n} dependence. By using information about the local IOP (backscattering or absorption) relationships, the inversion is possible.

Most semianalytic inversions of the remotely sensed reflectance depends on models of the spectral absorption [*Roesler and Perry*, 1995; *Lee et al.*, 1996; *Garver and Siegel*, 1997]. These inversions usually provide models for the individual absorption components (i.e., detritus, pigment, and colored dissolved

organic material). These models can be used with relation (3.13), and the reflectance can be inverted by minimization to obtain the absorption coefficient. Inversion to obtain the spectral absorption coefficient was demonstrated by use of simple linear relationships based on *in situ* observations. The results of the algorithm were compared with inversions of empirically derived nonlinear models based on remote-sensing reflectance ratios. Although the inversion algorithm provided in this study was shown to more accurately predict the absorption coefficient at 443 nm, it was noted that the largest error in both methods was due to the uncertainty of the spectral absorption relationships, especially in highly absorbing regimes. Improved or more-sophisticated models of the absorption coefficient are needed to obtain more-accurate inversions of the model. Use of such models should be investigated further.

3.7 REFERENCES

- Ahn, Y., A. Bricaud, and A. Morel, Light backscattering efficiency and related properties of some phytoplankters, *Deep-Sea Res.*, 39, 1835-1855, 1992.
- Barnard, A. H., J. R. V. Zaneveld, and W. S. Pegau, Global relationships of the inherent optical properties of the ocean, *J. Geophys. Res.*, 103, 24,955-24,968, 1998.
- Bricaud, A., A. Morel, and L. Prieur, Optical efficiency factors of some phytoplankters, *Limnol. Oceanogr.*, 28, 816-832, 1983.
- Campbell, J. W. and W. E. Esaias, Basis for spectral curvature algorithms in remote sensing of chlorophyll, *Appl. Opt.*, 22, 1084-1093, 1983.

- Garver, S. A. and D. A. Siegel, Inherent optical property inversion of ocean color spectra and its biogeochemical interpretation. 1. Time series from the Sargasso Sea, *J. Geophys. Res.*, 102, 18,607-18,625, 1997.
- Gordon, H. R., O. B. Brown, R. H. Evans, J. W. Brown, R. C. Smith, K. S. Baker, and D. K. Clark, A semianalytic radiance model of ocean color, *J. Geophys. Res.*, 93, 10,909-10,924, 1988.
- Lee, Z. P., K. L. Carder, T. G. Peacock, C. O. Davis, and J. L. Mueller, A method to derive ocean absorption coefficients from remote-sensing reflectance, *Appl. Opt.*, 35, 453-462, 1996.
- Lee, Z. P., K. L. Carder, R. G. Steward, T. G. Peacock, C. O. Davis, and J. S. Patch, An empirical algorithm for light absorption by ocean water based on color, *J. Geophys. Res.*, 103, 27,967-27,978, 1998.
- Maffione, R. A. and D. R. Dana, Instruments and methods for measuring the backward-scattering coefficient of ocean waters, *Appl. Opt.*, 36, 6057-6067, 1997.
- Moore, C., J. R. V. Zaneveld, and J. C. Kitchen, Preliminary results from an *in situ* spectral absorption meter, in *Ocean Optics XI*, G. D. Gilbert, ed., Proc. SPIE **1750**, 330-337, 1992.
- Morel, A., Optical properties of pure water and pure sea water, in *Optical Aspects of Oceanography*, N.G. Jerlov and E.S. Nielsen, eds., Academic Press, New York, pp. 1-24, 1974.
- Morel, A. and L. Prieur, Analysis of variations in ocean color, *Limnol. Oceanogr.*, 22, 709-722, 1977.
- Morel, A., Optical modeling of the upper ocean in relation to its biogenous matter content (case I waters), *J. Geophys. Res.*, 93, 10,749-10,768, 1988.
- Morel, A. and B. Gentili, Diffuse reflectance of oceanic waters. II. Bidirectional aspects, *Appl. Opt.*, 32, 6864-6879, 1993.
- Morel, A., K. J. Voss, and B. Gentili, Bidirectional reflectance of oceanic waters: a comparison of modeled and measured upward radiance fields, *J. Geophys. Res.*, 100, 13,143-13,151, 1995.

- Morel, A. and B. Gentili, Diffuse reflectance of oceanic waters. III. Implication of bidirectionality for the remote sensing problem, *Appl. Opt.*, 35, 4850-4862, 1996.
- Pegau, W. S., J. R. V. Zaneveld, and K. J. Voss, Toward closure of the inherent optical properties of natural waters, *J. Geophys. Res.*, 100, 13,193-13,199, 1995a.
- Pegau, W. S., J. S. Cleveland, W. Doss, C. D. Kennedy, R. A. Maffione, J. L. Mueller, R. Stone, C. C. Trees, A. D. Weidemann, W. H. Wells, and J. R. V. Zaneveld, A comparison of methods for the measurement of the absorption coefficient in natural waters, *J. Geophys. Res.*, 100, 13,201-13,220, 1995b.
- Pope, R. M. and E. S. Fry, Absorption spectrum (380-700 nm) of pure water. II. Integrating cavity measurements, *Appl. Opt.*, 36, 8710-8723, 1997.
- Preisendorfer, R. W., *Hydrologic Optics* (U.S. Dept. of Commerce, Washington, D. C., 1976), Vol. 4.
- Roesler, C. S. and M. J. Perry, *In situ* phytoplankton absorption, fluorescence emission, and particulate backscattering spectra determined from reflectance, *J. Geophys. Res.*, 100, 13,279-13,294, 1995.
- Smith, R. C. and K. S. Baker, Optical properties of the clearest natural waters, *Appl. Opt.*, 20, 177-184, 1981.
- Stramski, D. and D. A. Kiefer, Light scattering by microorganisms in the open ocean, *Prog. Oceanogr.*, 28, 343-383, 1991.
- Twardowski, M. S., J. M. Sullivan, P. L. Donaghy, and J. R. V. Zaneveld, Microscale quantification of the absorption by dissolved and particulate material in coastal waters with an ac-9, *J. Atmo. Ocean. Tech.*, 16(6), 691-707, 1999.
- Zaneveld, J. R. V., Remotely sensed reflectance and its dependence on vertical structure: a theoretical derivation, *Appl. Opt.*, 21, 4146-4150, 1982.
- Zaneveld, J. R. V., J. C. Kitchen, and C. C. Moore, Scattering error correction of reflecting tube absorption meters, in *Ocean Optics XIII*, J. S. Jaffe, ed., Proc. SPIE 2258, 44-55, 1994.

Zaneveld, J. R. V., A theoretical derivation of the dependence of the remotely sensed reflectance of the ocean on the inherent optical properties, *J. Geophys. Res.*, 100, 13,135-13,142, 1995.

Zaneveld, J. R. V. and W. S. Pegau, A model for the reflectance of thin layers, fronts, and internal waves and its inversion, *Oceanography*, 11, 44-47, 1998.

CHAPTER 4

DETECTION AND CHARACTERIZATION OF INTERNAL WAVES IN A
COASTAL ENVIRONMENT FROM HIGH SPATIAL RESOLUTION VISIBLE
REMOTE SENSING IMAGERY.

Andrew H. Barnard, J. Ronald V. Zaneveld, Emmanuel Boss, Alan
Weidemann, W. Scott Pegau, Jack A. Barth, and W. Joseph Rhea.

Manuscript to be submitted to *Journal of Geophysical Research*

4.1 ABSTRACT

A series of bright and dark bands of radiance were detected in high spatial resolution, visible, remote sensing imagery obtained on August 11, 1998 over East Sound, WA. These lineal features of contrast were located in the lee of a shallow water sill near the entrance to the Sound, suggesting an internal wave as the causal mechanism. A two-layer model based on the spatial contrast within the image was developed to determine the amplitude of the oscillations in the thermocline. The depth fluctuations of the thermocline observed in the in situ profiles of temperature, and predicted using the water leaving radiance imagery, showed the amplitude of the internal wave to range from 1.25 to 2 m, with vertical displacements as great as 3 m in relation to the upstream depth of the thermocline. The largest increase in the water leaving radiance and the deepest fluctuation in the amplitude occurred near shallowest side of the sill. The results of the model indicated that the thermocline initially deepened upon crossing the sill, while on the eastern side of the Sound, the internal wave oscillated around the thermocline depth upstream of the sill. The wavelength of the internal wave ranged from 24 to 48 m moving west to east across the sill. These results were used to provide a physical interpretation of the spatial distribution and generating mechanism of the internal wave.

4.2 INTRODUCTION

Vertical stratification of the bio-optical constituents of the surface oceans is often the result of the interaction between the physical and biogeochemical processes. For example, physical processes such as horizontal intrusions, internal waves, and Langmuir circulation can lead to localized mixing and re-distribution of water masses thereby affecting the vertical stratification of the bio-optical properties. Understanding the interplay between the physical and biogeochemical processes is thus necessary for interpreting the observed spatial patterns in the bio-optical properties. In this paper, we examine how spatial information provided by remote sensing observations can be utilized to understand the physical processes affecting the spatial variability in the bio-optical properties.

Internal waves are common features of the coastal environment. In semi-enclosed coastal regions dominated by the tides, variations in bottom topography often serve as a generation site for internal waves [Apel *et al.*, 1975; Witman *et al.*, 1993]. In these regions, internal waves are of interest as a possible mixing mechanism and re-distribution site for various biogeochemical constituents of the upper water column. Farmer and Armi [1999a and b] present an excellent discussion of the spatial and temporal evolution of a topographically generated internal wave. In addition to topography, the stability of the water column and the strength of the tidal flow are important factors in the development and generation of an internal wave. The combination of these factors determines the degree to

which internal waves affect the physical and biological structure of the water column.

Internal waves have frequently been observed from active remote sensing imaging systems such as synthetic aperture radar [e.g., *Hughes and Gower, 1983; Alpers 1985; Ouchi et al., 1997*]. However, microwave imaging systems are only able to detect changes in the surface roughness created by the hydrodynamic interaction of the surface waves with the circulation induced by the internal waves. Radar signatures of internal waves are dependent on local wind speed and surface film tension [*da Silva et al., 2000*] and thus contain very little information about the waveform and the depth of the internal waves, or to the possible bio-optical variations associated with an internal wave.

Detecting subsurface structure using visible remote sensing techniques has been investigated by a variety of authors [*Gordon, 1992; Zaneveld and Pegau, 1998; Haltrin, 1999; Weidemann et al., 2000*]. The water leaving radiance in the visible portion of the spectrum is dependent on the inherent optical properties of the oceans as well as the input light field. Visible remote sensing radiometers measure the water leaving radiance and thus contain information on the optical properties of the surface ocean once the atmospheric path radiance and surface reflections have been accounted for. A common parameterization used in visible remote sensing is the remote sensing reflectance ratio defined as

$$R_{rs}(\lambda) = \frac{L_w(\lambda)}{E_s(\lambda)} \cong G \frac{b_b(\lambda)}{a(\lambda)}, \quad (4.1)$$

where L_w is the water leaving radiance, E_s is surface downwelling irradiance, G is a factor to account for the shape of the light field and the phase function, b_b is the backscattering coefficient, and a is the absorption coefficient where all parameters are a function of wavelength λ . In a vertically stratified water column, the remote sensing reflectance received by the sensor is dependent on the vertical structure of the b_b/a in an exponentially decreasing manner with increasing depth [Gordon, 1992; Zaneveld *et al.*, 1998].

Zaneveld and Pegau [1998] investigated the necessary conditions for detecting an internal wave using spatial information provided in visible remote sensing imagery. First, the vertical contrast in the b_b/a structure must be associated with the variability in the physical structure of the internal wave. Second, the internal wave must reside sufficiently close to the surface in order for subsurface modulations in the b_b/a structure to contribute to the remotely sensed signal. Provided these two conditions are met, they showed how spatial contrast observed in the remotely sensed imagery can be used to predict the amplitude of an internal wave.

Recent work by Weidemann *et al.*, [2000] has shown that internal waves can be detected in visible remote sensing imagery. In their study, variations in the thickness of the turbid bottom layer caused by the deformation of the pycnocline by the internal wave passage resulted in a change in the above water reflectance in the visible wavelengths. These subsurface oscillations in the optical properties caused by the internal wave resulted in banded features of high and low contrast in the

visible imagery obtained by aircraft. Using in situ profiles of the optical properties obtained concurrently with the imagery as inputs to a radiative transfer model, they were able to simulate these lineal features of reflectance contrast. The results of *Weidemann et al.*, [2000] provide further evidence that subsurface modulations in the optical properties due to internal wave passage can be detected using visible remote sensing imagery. As the authors pointed out, the advantage of using visible remote sensing as opposed to radar imagery, is the information it can provide on the wave train characteristics. However, prediction of the speed and amplitude of the internal wave was not possible in the study of *Weidemann et al.*, [2000] due to the limited spatial resolution of the remote sensing imager.

Similar lineal features of high and low radiance contrast were observed during an experiment of combined in situ optical and physical measurements and visible remote sensing over East Sound, Washington. The location of these lineal features suggested a topographically generated internal wave as the causal mechanism. It is the purpose of this paper to show that subsurface variations in the optical properties associated with an internal wave can be detected in the upwelled radiance of visible remote sensing imagery. Furthermore, we demonstrate how the wave train characteristics of an internal wave can be predicted using the spatial information contained in the remote sensing imagery. Finally, in combination with the in situ data collected in this region, we show how the imagery is useful in providing a physical interpretation of the causal mechanisms of the internal wave.

4.3 EXPERIMENTAL SITE AND MEASUREMENTS

East Sound is a productive fjord located within Orcas Island, in the San Juan Islands, WA (Figure 4.1). The average depth of the water column is 30 m with a sloping sill extending from the western edge of the opening of the Sound at a depth of 12 m. A deep-water channel is located east of the sill measuring 44 m in depth. The width of the Sound at the entrance is approximately 2 km. The flow throughout the Sound is strongly influenced by the semi-diurnal tides with a maximum tidal range of approximately 3.5 m. Surface flow is dependent on the local winds, which are predominantly from the south-southeast. A detailed description of the general circulation and meteorological conditions within East Sound is given in *Deksheniaks et al.*, [2000].

A full suite of optical and physical parameters was measured concurrent with the acquisition of aircraft-borne radiometric imagery on August 11, 1998. The location of the in situ sampling stations and the area imaged by the airborne radiometer is shown in Figure 4.1. Station A was located north of the sill, while stations B and C were located on the sill in water column depths of 10 and 13 m respectively. Vertical profiles of the in situ parameters were collected between 10:30 and 11:58 am Pacific Daylight Time. The aircraft-borne radiometric data was obtained at approximately 10:33 am. Surface winds throughout the sampling period were light (less than 3 m s^{-1}) and variable, and sky conditions were clear with high visibility. All sampling occurred during the middle of the strongest spring ebb tide. Current velocities below the surface layer are predominately to the

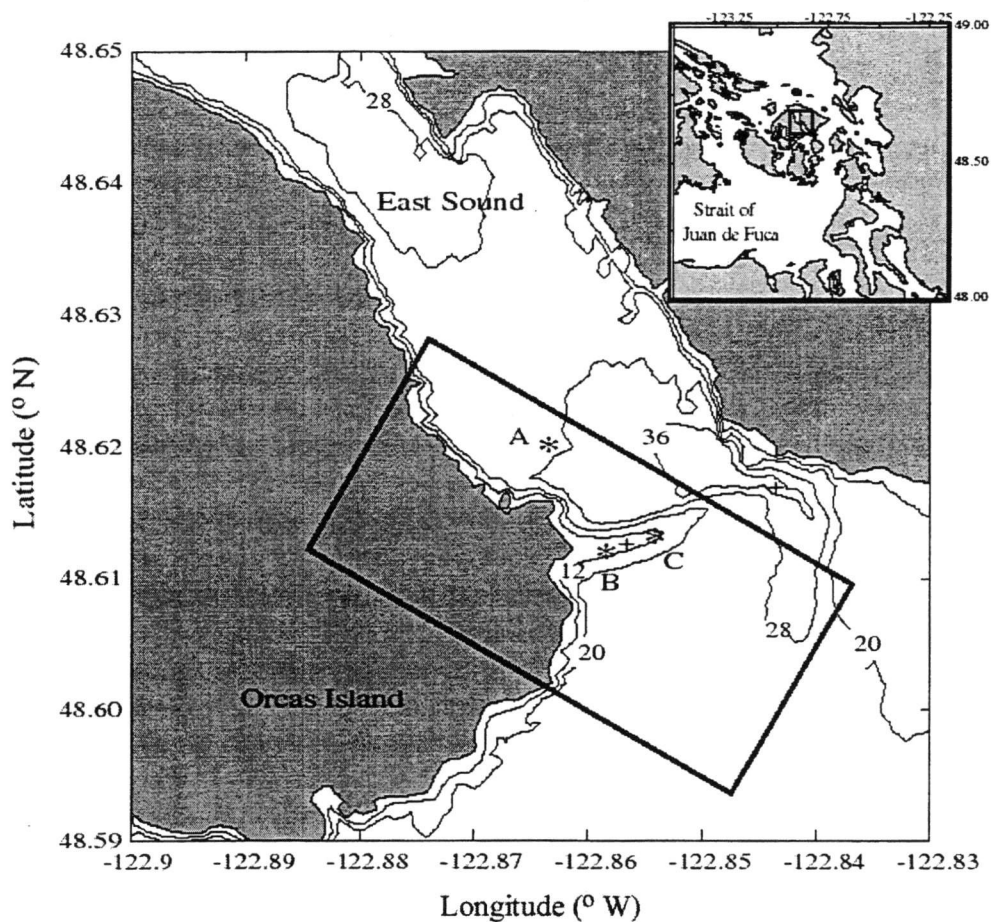


Figure 4.1. Small inset: East Sound, Orcas Island, Washington, located between the Strait of Juan de Fuca and the Strait of Georgia. Main chart: Chart of East Sound with contours of bathymetry (m). The in situ sampling locations conducted on August 11, 1998 are shown as asterisks, labeled as stations A, B, and C. The locations of the bottom moored ADCP's are shown as plus symbols. The area of the aircraft imagery is shown as the rectangle.

south (out of the Sound) during the ebb tide, with the maximum velocities occurring on the western edge of the Sound [Dekshenieks *et al.*, 2000].

Vertical profiles of hydrographic and inherent optical properties (IOP) were measured simultaneously using a free-falling sampling platform. A detailed description of the deployment and instrument configuration of the optical platform in addition to the data integration and processing methods used are given in *Barnard et al.*, [1998] and *Twardowski et al.*, [1999]. The spectral absorption and beam attenuation coefficients were measured using a field calibrated WET Labs ac-9 meter. The backscattering coefficient was measured using a HOBI Labs Hydroscat-6. A SeaBird CTD was used to provide measurements of temperature, conductivity, and pressure. Chlorophyll fluorescence was measured using a WET Labs WetStar fluorometer. The vertical resolution in the optical and physical parameters after post-processing procedures were performed was 0.25 m. The profiling system did not resolve the structure in the upper 1 to 2 meters of the water column since the intakes for the CTD and optical instruments were on the leading edge of the profiling package.

The in situ radiometric properties were measured at stations A and B in addition to the IOP and hydrographic profiles. Profiles of the spectral downwelling irradiance and upwelling radiance were made using a Satlantic Inc. SPMR radiometer system. Above water reflectance spectra were measured using an Analytical Spectral Devices, Inc. portable spectrometer. Reflectance measured from a gray Spectralon plaque was used to scale the digital counts to water reflectance. Above water radiance spectra were derived using the surface and sky reflection correction techniques for case 2 waters provided by *Gould et al.*, [1998].

Spatial imagery of the upwelling radiance spectrum was obtained using the Navy's Portable Hyperspectral Imager for Low-Light Spectroscopy (PHILLS) sensor mounted on a small aircraft. Details of the PHILLS sensor are provided in *Kappus and Davis* [1998]. The direction of the flight path and the sampling time were chosen in order to minimize the effects of sun glint. The spatial area of the imagery used in this study is approximately 3.5 km long and 1.5 km wide and took approximately two minutes to acquire (Figure 4.1). The approximate spatial resolution of each pixel within the imagery is 6 m. Unfortunately, no accurate calibration of the airborne spectrometer was available. Furthermore, atmospheric and surface reflection effects were not removed from the data. We employed an empirical line calibration technique to force the imagery to match the above water upwelling radiance spectra measured at stations A and B using the ENVI® software package. While this technique does provide a method to remove the solar irradiance and the atmospheric path radiance, it does not however, correct for surface reflectance variations. However, as surface winds were light (< 0.2 m) and wave heights were minimal during the period of image acquisition, we have assumed that the spatial variability within the imagery due to surface effects (i.e. glint and roughness) is negligible.

4.4 INITIAL OBSERVATIONS

A series of alternating bright and dark lines located to the south of the sill were visible in selected bands of the aircraft imagery (Figure 4.2). These lines

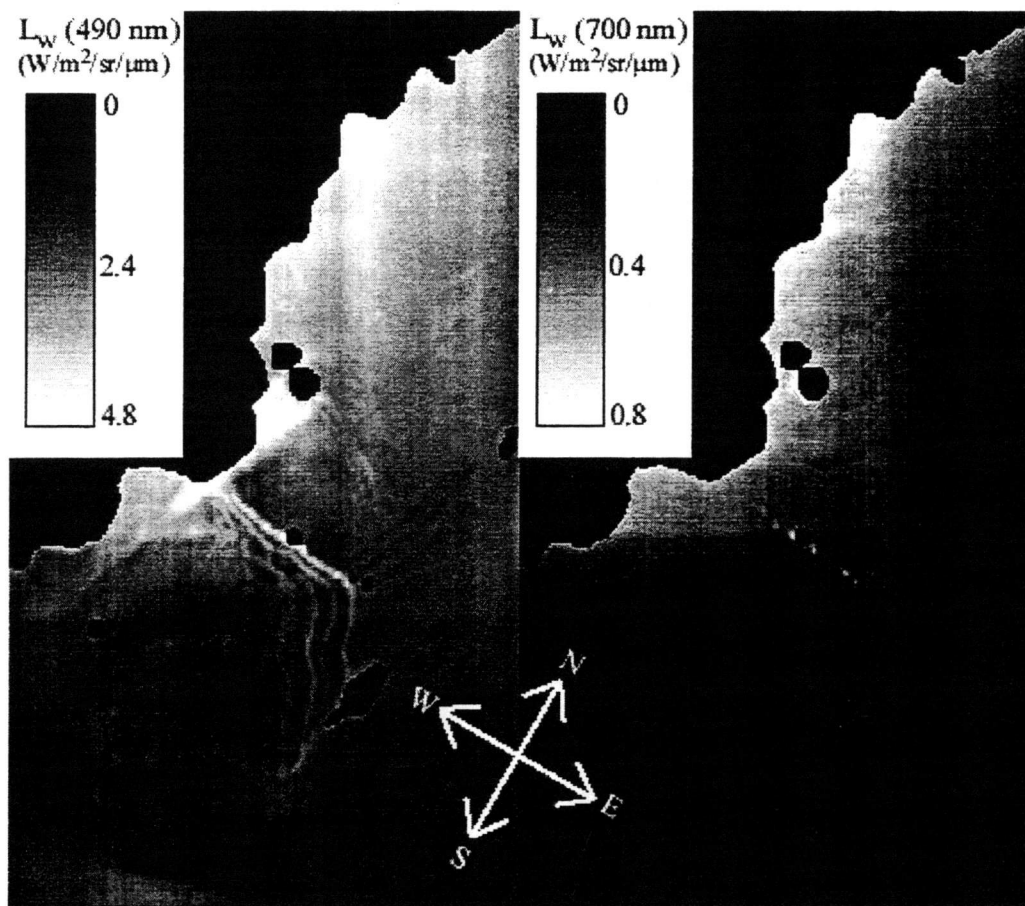


Figure 4.2. The empirically calibrated values of water leaving radiance at the 490 nm (left panel) and the 700 nm (right panel) wavelengths as measured by the PHILLS radiometer over East Sound on August 11, 1998. Note the bright radiance lines that extend eastward, just to the south of the shallow sill in the imagery at the 490 nm wavelength. These bands are not discernable in the water leaving radiance at the 700 nm wavelength. Ships and islands within the sound have been masked as black patches.

were oriented parallel to the main axis of the sill on the western side of the Sound, and at an angle to the sill in the deeper central portion of the Sound. If the banding patterns were caused by changes in the surface roughness associated with the hydraulic interaction of the internal wave and the surface waves, one would expect

these features to be apparent throughout the visible and near-infrared spectrum. However, only the northernmost bright line was faintly discernable in the 700 nm wavelength imagery (Figure 4.2), which was coincident with a surface accumulation of organic matter observed from the ship. The fact that the lineal bands of contrast are not apparent at the longer wavelengths suggests that these features are due to changes in the water leaving radiance rather than changes in the horizontal surface roughness.

The radiance contrast between these bright and dark lineal features was highest in the 440 to 550 nm wavelengths of the aircraft imagery. As shown in Equation 4.1, the water-leaving component of the upwelling radiance is dependent on the vertical structure of the inherent optical properties of the water, more specifically the backscattering to absorption ratio b_b/a . The magnitude of the backscattering and absorption coefficients at 490 nm is dependent on the particle concentration and composition. Variations in the optical properties at this wavelength will thus affect the water leaving radiance. We therefore chose to use the water leaving radiance imagery collected at 490 nm wavelength for our analyses. The parallel nature and the proximity of the lineal features in relation to the location of the sill suggest that the causal mechanism of these features is related to the change in the bathymetry. In order to elucidate the causal mechanism for the features in the 490 nm radiance imagery, we examined the vertical profiles of hydrographic and optical properties obtained within the imaged area.

The physical structure at each of the in situ sampling stations was similar, with a warm, less saline surface layer overlying a colder, saltier bottom layer (Figure 4.3). The density structure depends primarily on temperature, with a 5° C difference between the upper and lower layers (~0.3 PSU salinity difference), resulting in a $\sim 1.11 \text{ kg m}^{-3}$ density difference between the two layers. The base of

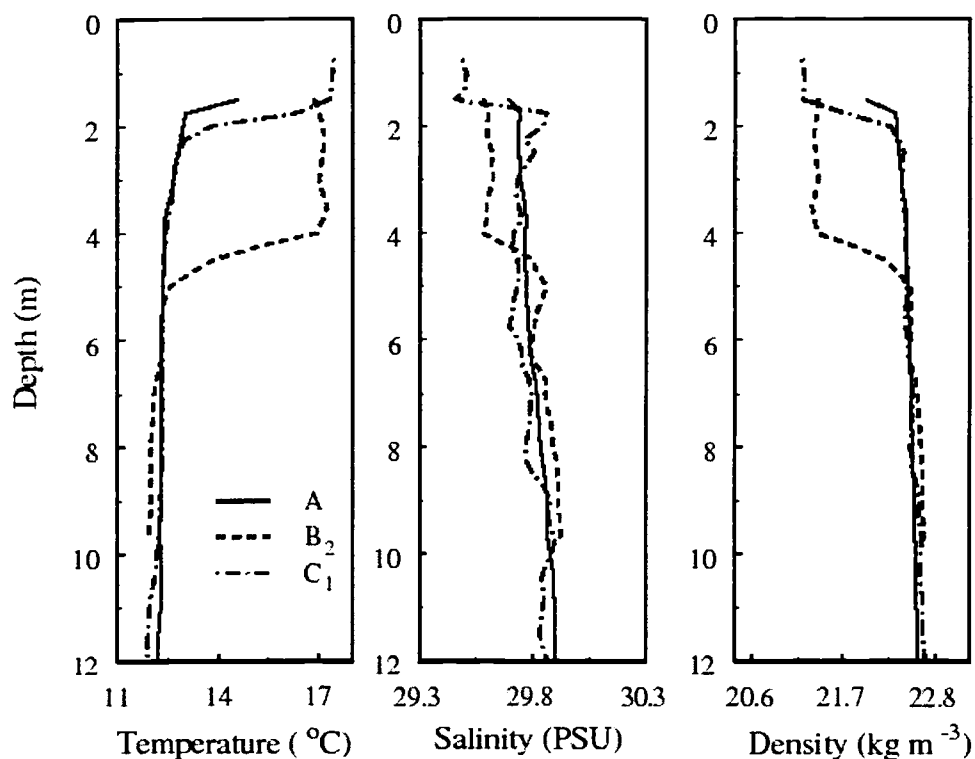


Figure 4.3. Vertical profiles of temperature (left panel), salinity (middle panel), and density anomaly (right panel) in the upper 12 m at stations A (solid line), B (dashed line), and C (dot-dashed line) shown in figure 4.1. The subscripts denote which profile in each series is plotted (see figure 4.4) for stations B and C.

the thermocline (pycnocline) is located in the upper 2.5 m of the water column north of the sill (station A) and on the eastern side of the sill (station C). On the western side of the sill (station B), the base of the thermocline is at approximately 5 m. Although the shallow temperature structure is not fully resolved at the upstream (station A) location, the base of the thermocline appears to be at approximately 1.75 m, the shallowest depth of the three stations.

At stations B and C, a series of three profiles was obtained within 8 minutes of each other, with each profile located slightly further to the southeast due to the ship drift. On the western side of the sill (station B), the base of the thermocline varied between 3 and 5 m, while on the eastern edge of the sill (station C), the base of the thermocline varied from 2.5 to 4 m (Figure 4.4). Our data show that the amplitude of the thermocline vertical oscillation was approximately 2 and 1.5 m on the western and eastern sides of the sill, respectively. Rapid fluctuations in the depth of the thermocline such as those observed at stations B and C, are characteristic of high-frequency internal waves. High-frequency oscillations in the depth of isotherms were frequently observed in thermistor chain data recorded earlier in the summer in the northern part of East Sound [T. J. Cowles, personal communication]. Note that in comparison to the depth of the thermocline upstream at station A, the thermocline is displaced approximately 3.25 and 2.25 m on the western and eastern sides of the Sound respectively.

While the in situ observations of the physical parameters reveal some spatial and temporal variability in the displacement of the thermocline, the limited

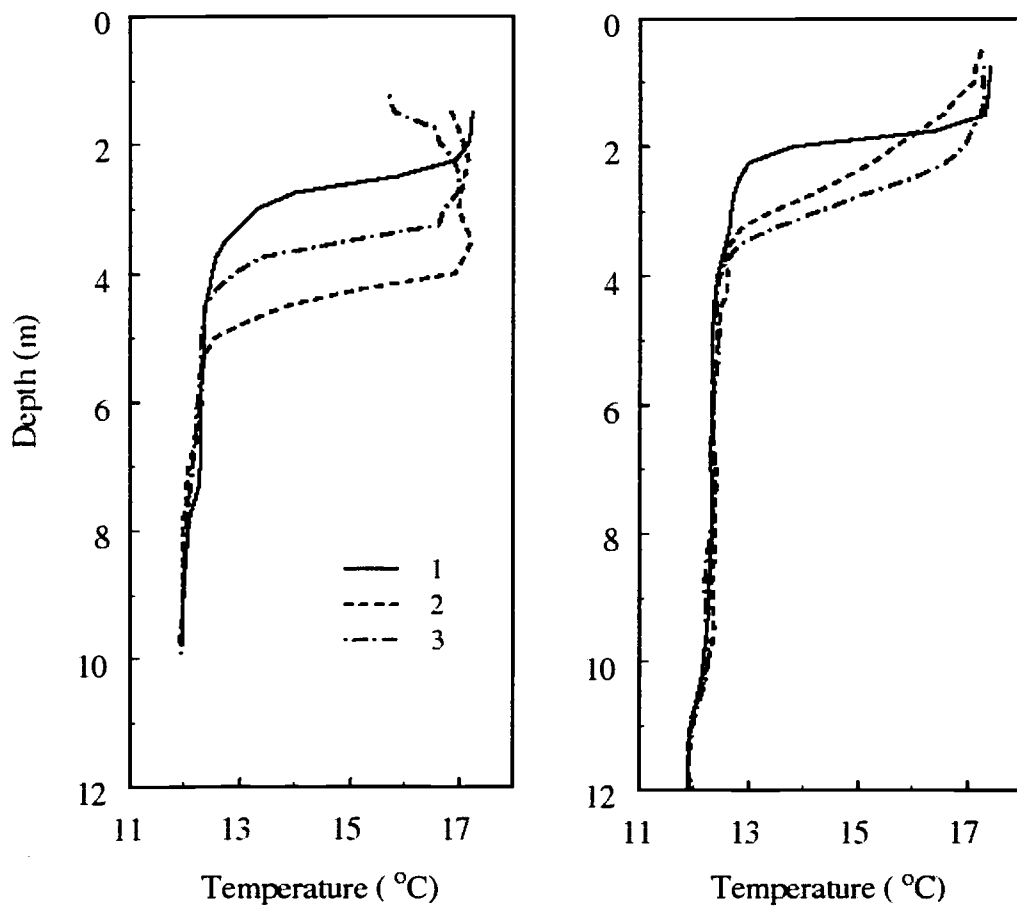


Figure 4.4. Profiles of temperature at stations B (left panel) and C (right panel) on August 11, 1998. The profiles are numbered in the order in which they were made.

number of profiles obtained during this one hour interval are not adequate to resolve the internal wave field. Used in conjunction with the high spatial resolution PHILLS imagery, however, these in situ data can be applied to determine the internal wave characteristics.

4.5 REMOTE SENSING OF INTERNAL WAVES

Recall that the remotely sensed radiance is proportional to the exponentially weighted backscattering to absorption ratio in the upper water column. Three conditions are necessary in order to be able to characterize an internal wave based on the spatial variability in the remote sensing reflectance. First, vertical structure in the b_p/a ratio must exist. More specifically, the reflectance above the pycnocline must be distinctly different from the reflectance below the pycnocline [Zaneveld and Pegau, 1998]. Second, the depth of the pycnocline must be located sufficiently close to the surface in order for the vertical variations in the optical structure to contribute significantly to the remotely sensed signal. Finally, the spatial resolution of the remote sensing imagery must be smaller than one half of the wavelength of the internal wave in order to resolve the wave train. We examine each of these conditions in the following sections.

The in situ profiles of the absorption coefficient at 490 nm at station B showed a surface layer with low absorption overlying a layer with greater absorption (Figure 4.5). Similar vertical structure in the absorption coefficient at 490 nm was observed at station C. The depth of the optical gradient oscillated between 3.5 to 5 m, similar to the oscillations observed in the depth of the thermocline (Figure 4.5). The vertical structure of the absorption coefficient at 490 nm co-varied with the chlorophyll fluorescence (not shown) indicating that the increase in absorption below the thermocline is associated with an increase in phytoplankton pigments.

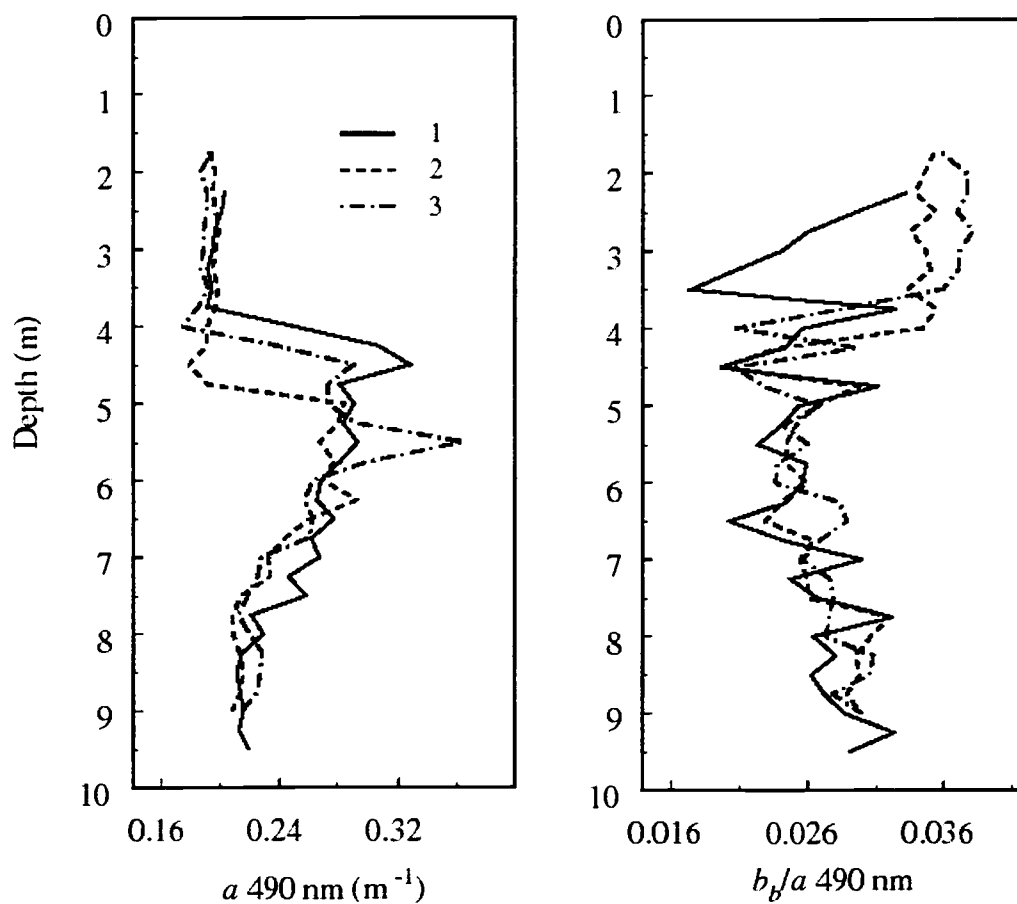


Figure 4.5. The profiles of the absorption coefficient at 490 nm (left panel) and the backscattering to absorption ratio at 490 nm (right panel) at station B. The numbers indicate the order in which the profiles were made.

Figure 4.5 shows the vertical profiles of the backscattering to absorption ratio for the same three profiles at station B. The profiles show that the waters above the thermocline had a larger b_v/a ratio as compared to the waters below the thermocline. Thus, the upper layer was more reflecting compared to the lower layer. The vertical boundary between these two layers varied in depth by approximately 1.5 m over the sampling period of these profiles. The cause of the

vertical contrast in b_p/a ratio was due primarily to the non-covariance of the backscattering and the absorption coefficient of phytoplankton particles [Kitchen and Zaneveld, 1990]. Below the thermocline, the absorption coefficient disproportionately increased relative to the increase in the backscattering thereby decreasing the b_p/a ratio of the lower layer. The sharp contrast in b_p/a (nearly a factor of 2) between the two layers was a key factor in resolving the internal wave in the visible remote sensing imagery.

In order to resolve the subsurface contrast in the b_p/a structure in the water leaving radiance, the boundary between these two layers must reside sufficiently close to the surface in order for the bottom layer to contribute to the water leaving signal. We used the penetration depth [Gordon and McCluney, 1975] to examine the contribution of the b_p/a vertical structure on the water leaving radiance. The penetration depth, or e-folding depth, is the depth above which 90% of the water leaving reflectance originates. Thus, for an internal wave to be fully resolved in the imagery of the water leaving radiance, the penetration depth must be greater than the depth of the trough of the internal wave. We estimated the penetration depth to be the depth at which the downwelling irradiance at the 490 nm wavelength was attenuated to 10% of the surface value. The penetration depth varied between 6 and 7 m based on the in situ profiles of the downwelling irradiance at station B. As this depth is greater than the depth of the thermocline observed in all of the profiles, we conclude that the vertical fluctuations in the structure of the b_p/a ratio do contribute to the remotely sensed signal at 490 nm.

To discern the waveform of the internal wave, the spatial resolution of the imagery must be less than one half of the wavelength of the internal wave. The approximate spatial resolution of the imagery was 6 m, thus limiting detection of internal waveforms to those with wavelengths greater than 12 m. As we show below, the lineal features of bright and dark radiance were 20-50 m apart, thus permitting use of the imagery to resolve the wavelength.

4.6 MODEL PREDICTIONS OF INTERNAL WAVE CHARACTERISTICS

A two-stream radiative transfer model to determine the amplitude of an internal wave based on the spatial contrast in the irradiance reflectance R , was developed by *Zaneveld and Pegau* [1998]. In their formulation, the water column is modeled as a two-layer system, where the optical properties of each layer are different and are separated by the pycnocline. The amplitude of the modeled internal wave alters the height or thickness of each optical layer, resulting in changes in the reflectance. Three reflectance measurements are needed for this model; the reflectance upper layer alone $R_{\infty 1}$, the reflectance where the internal wave is at its crest $R(x_1)$, and the reflectance at the trough of the internal wave $R(x_2)$. The amplitude A , can then be determined based on the irradiance reflectance R at each of these three locations using

$$2Ag_1 = -0.5 \ln \left[\frac{R(x_2) - R_{\infty 1}}{R(x_1) - R_{\infty 1}} \right], \quad (4.2)$$

where g_l is the diffuse attenuation coefficient that describes the round trip attenuation of the upwelling and downwelling irradiance [Zaneveld and Pegau, 1998]. Although the original derivation of the model was given in irradiance reflectance, the mathematical formulation is identical when using the remote sensing reflectance.

To apply this model, one must identify a spatial location within an image where the observed reflectance is entirely due to the optical properties of the upper layer. Typically, a priori knowledge of the vertical structure of the optical properties within an image is not available, and thus identifying a region where the reflectance is due solely to the optical properties of the upper layer is not often possible. Thus, we would like to derive a model based on the reflectance contrast within the imagery that makes few assumptions about the optical properties and the vertical structure of the water column. In the case of the imagery obtained over East Sound, we would like to determine the vertical displacement of the pycnocline upon crossing the sill in order to resolve the amplitude of the internal wave.

We chose to develop the following model using the remote sensing reflectance R_{rs} . The reader is reminded that we assumed the surface downwelling irradiance is constant and therefore the remote sensing reflectance is directly proportional to the water leaving radiance at the time of image acquisition on August 11, 1998. We assumed a simple two-layer system, where the optical properties of the upper layer are different from the lower layer, and the reflectance of the upper layer is different from the lower layer. Furthermore, as with the

Zaneveld and Pegau [1998] derivation, we assumed that over the area of interest, the IOP of the upper and lower layers are different but constant, and that only the depth of boundary between these two layers changes. The remotely sensed reflectance is therefore only dependent on the thickness of the upper layer and the contrast between the two optical layers. It can be shown that the difference in the thickness of the upper layer between two spatial locations $H(x_2) - H(x_1)$, can be determined by referencing the reflectance to a third location (x_3) using,

$$H(x_2) - H(x_1) = \frac{1}{2g_1} \ln \left[\frac{R_{rs}(x_1) - R_{rs}(x_3)}{R_{rs}(x_2) - R_{rs}(x_3)} \right], \quad (4.3)$$

where H is the height or thickness of the upper layer. This model requires that the reflectance at the reference location x_3 , is different than the reflectance at both of the other two spatial locations.

To apply this model, we extracted three linear transects of water leaving radiance at 490 nm from the aircraft imagery, where each line was oriented perpendicular to the bright reflecting radiance features (Figure 4.6). $R_{rs}(x_1)$ locations were selected upstream (north) of the first bright reflectance line, representing the case where the pycnocline is at its undisturbed depth. Reference locations $R_{rs}(x_3)$, were selected as the lowest radiance value downstream and along axis of the extracted lines. As the in situ profiles showed the bottom layer to be the least reflecting (lowest b_p/a), we assumed that the lowest reflectance represented the case when the lower layer was at or very near surface. The change in the thickness of the upper layer relative to the upstream depth was then computed along the extracted lines of the radiance data $R_{rs}(x_2)$.

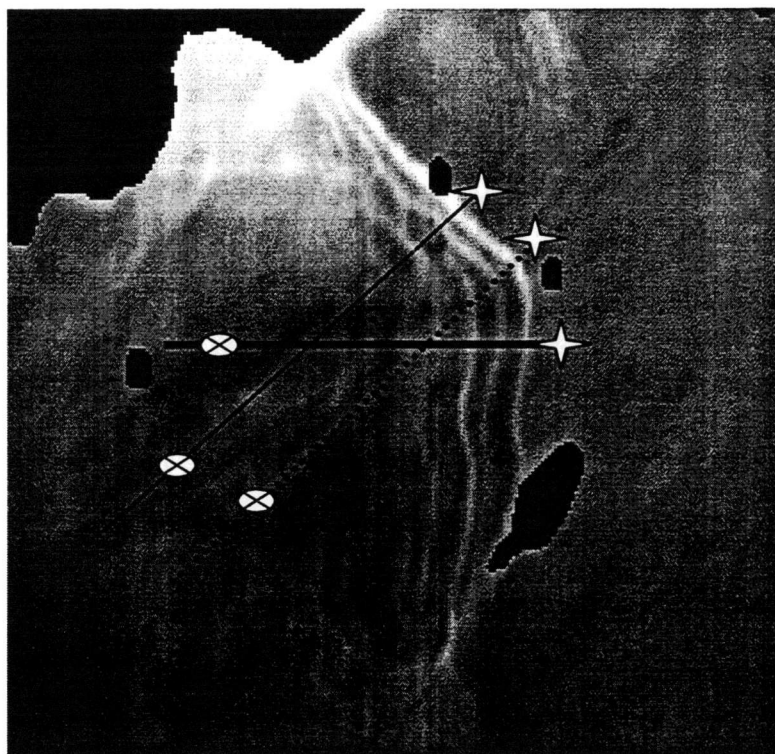


Figure 4.6. Locations of the three transects of the 490 nm water leaving radiance extracted from the aircraft imagery along which the internal wave amplitude was computed (x_2 locations). The x_1 locations for each line are shown as stars, and the x_3 locations are shown as ellipses with crosses. The solid line shows the location of the transect on the western side of the sound, the dashed line shows the location of the transect line in the central portion of the sound, and the location of the easternmost transect is shown as a thick solid line.

The two-way diffuse attenuation of the upper layer g_1 must be estimated to use this model. *Maritorena et al.*, [1994] showed that g_1 ranges between 1.01 to 1.33 of the diffuse attenuation coefficient K_d , depending on the irradiance distribution and the inherent optical properties. By choosing to use the average, $g_1 = 1.16 K_d$, an error no greater than 15% is possible in the prediction of the

displacement depth. A model to estimate K_d at 490 nm based on the ratio of the upwelling radiance at the 490 and 555 nm wavelengths was provided by *Mueller* [2000]. We used the PHILLS radiance data at 490 and 555 nm wavelengths to estimate K_d over East Sound. K_d estimated in this manner ranged from 0.17 to 0.22 m^{-1} over most the image. However, the model requires that the diffuse attenuation coefficient be determined only by the optical properties of the upper layer. As we have no a priori way of determining K_d in the upper layer only from the imagery, we chose to use the average K_d equal to 0.20 m^{-1} . The diffuse attenuation coefficient was calculated from the in water profiles of the downwelling irradiance at 490 nm obtained at stations A and B. The upper water column averaged diffuse attenuation coefficient at these stations was $0.21 \pm 0.05 \text{ m}^{-1}$, which compares well with the K_d estimated using the PHILLS radiance data. For the purpose of the model, we chose to use $K_d = 0.20 \text{ m}^{-1}$, and $g_I = 1.16 K_d = 0.232 \text{ (m}^{-1}\text{)}$. Using these values and the model we inverted the water leaving radiance data to obtain the depth of the interface as a function of spatial location.

The water leaving radiance and the vertical displacement along each of the extracted lines are shown in Figure 4.7. The model results show an inverse relationship between water leaving radiance and vertical displacement, where an increase in the water leaving radiance corresponds to a deepening of the thermocline. A deepening of the thermocline at the trough of the internal wave caused an increase in the reflectance due to the stretching of the upper, more reflecting layer. Immediately upon crossing the sill, the thermocline initially

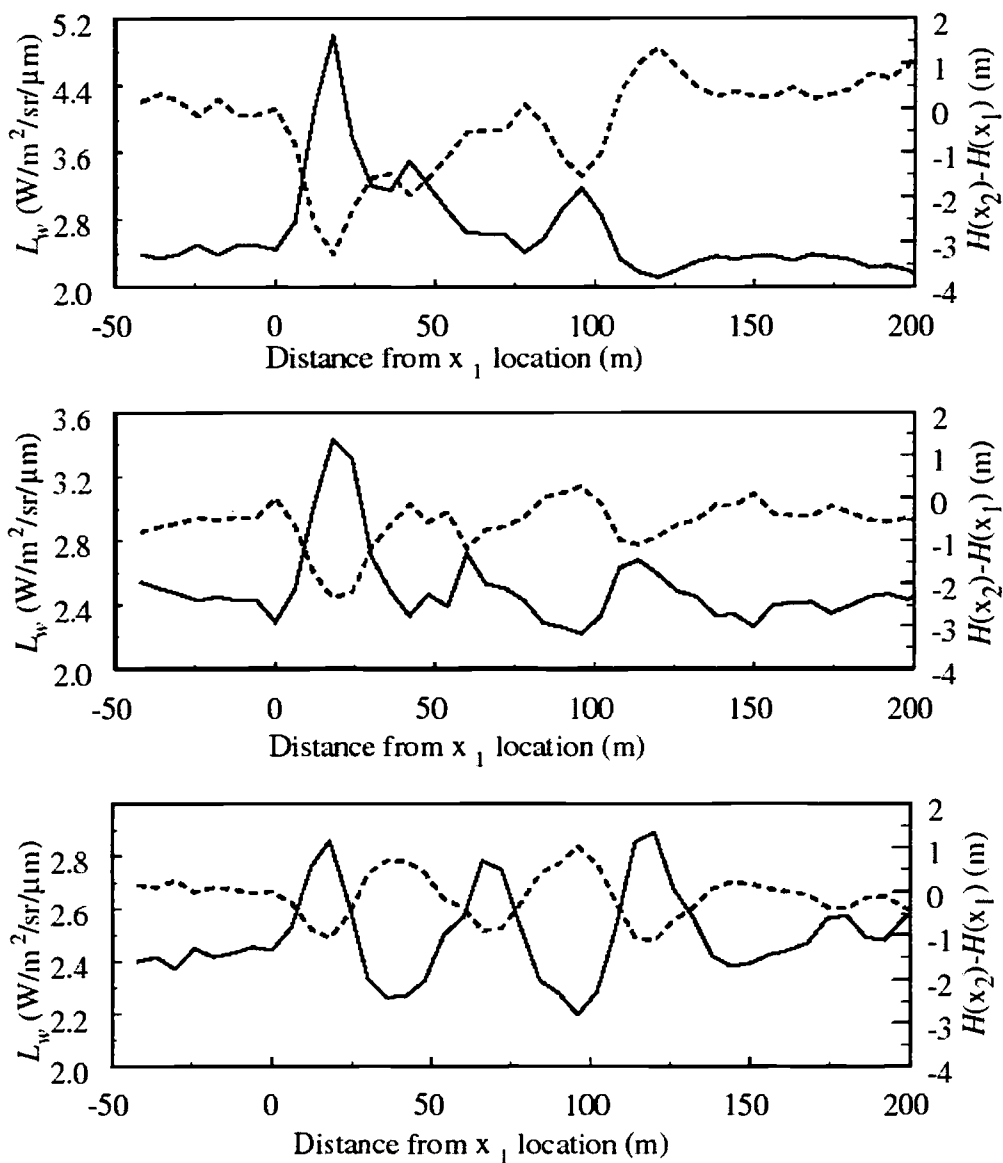


Figure 4.7. The water leaving radiance at 490 nm wavelength (solid lines) versus distance from the x_1 location is shown for the western (top panel), central (middle panel), and eastern (bottom panel) transect lines (see figure 4.6). Also plotted is the change in the depth of the pycnocline relative to the depth at the x_1 location using the model given in the text for each of the three transect lines (dashed line).

deepened to its maximum depth relative to the upstream location. The amplitude of the initial deepening was the largest on the western side of the sill, deepening by over 3 m, while along the next transect further to the east, the thermocline deepened by 2.25 m. Further downstream the thermocline continues to oscillate, gradually rising until it reaches its upstream depth by 140 m downstream. The absolute amplitude along the easternmost line is approximately 2 m. However, note that in this wave train the thermocline oscillates around the upstream depth rather than undergoing an initial deepening as seen in the other two lines. The amplitudes calculated along all three stations are similar to the thermocline oscillations observed in the in situ profiles. Given the inaccuracies in the calibration of the imagery and the assumptions of the model, we find it remarkable that the model predictions based on the aircraft imagery compared so well with the in situ observations.

The wavelength of the internal wave can be estimated by measuring the spacing between the water leaving maxima (or between H_2-H_1 minima) from the transects shown in Figure 4.7. Over the first 60 m downstream of the sill, the wavelength of the internal wave increases from approximately 24 m to 48 m moving west to east across the Sound. About 140 m downstream of the sill, at all three locations, the interface has returned to the upstream depth and shows little evidence of depth fluctuations.

4.7 DISCUSSION

We have demonstrated that subsurface changes in optical properties associated with the hydrographic stratification can be detected using visible remote sensing techniques. The reflectance pattern observed in the imagery in relation to the location of the sill indicated an internal wave as the causal mechanism. A model was developed to estimate the change in the depth of the thermocline that utilized the spatial contrast in the water leaving radiance of the aircraft imagery without a priori knowledge of the optical properties of water column using the K_d estimated using the imagery. The results of the model showed that the depth of the pycnocline was initially displaced over 3 m from its upstream depth on the western side of the Sound and then oscillated in depth finally reaching its upstream depth by 140 m downstream. On the eastern side of the Sound, the pycnocline oscillated around its original upstream depth with an amplitude of nearly 2 m. The wavelength of the internal wave was also seen to increase from 24 m on the western side of the Sound to 48 m on the eastern side.

The spatial and temporal evolution of stratified flow over a sill was studied in detail by *Farmer and Armi* [1999a] in Knight Inlet, British Columbia. Although the water column depth and the density gradient observed in Knight Inlet was larger than in East Sound, it does provide a useful context in which to compare the physical conditions between the two systems. Some hydrodynamic definitions are useful before providing a brief summary of their results. The Froude number F , is

the ratio between the velocity of the flow, and the phase speed of the internal wave (c_0). The phase speed of the internal wave in a two layered system is defined as

$$c_0 = \sqrt{g' \frac{h_1 h_2}{h_1 + h_2}}, \quad (4.4)$$

where g' is the reduced gravitational acceleration, h_1 is the thickness of the water column above the pycnocline, and h_2 is the thickness below the pycnocline. When the phase speed is greater than the current velocity, termed subcritical conditions ($F < 1$), the internal wave can propagate within the advecting current. However, in conditions termed supercritical, where the current velocity is greater than the phase speed ($F > 1$), the internal wave is unable to propagate as the hydrological structure is controlled by the current velocity. These conditions are similar to a plane travelling at Mach speed, where the plane's speed is faster than the speed of sound. In this case a shock wave forms in front of the plane due to the compression of the sound waves as the plane travels faster than the sound.

Our observations in East Sound can be evaluated in the context of *Farmer and Armi's* [1999a] interpretations of internal waves during ebb tide flow in Knight Inlet. The sill (75 m deep) extends fully across the width of Knight Inlet, shallowing from over 150 m up- and down-stream of the sill. During the beginning of the ebb tide, there is an initial acceleration of the flow beneath the pycnocline over the sill. This generates a velocity shear across the pycnocline in response to the subcritical conditions. As the ebb tide continues, internal waves develop near the crest of the sill, become unstable, and result in entrainment and mixing. The

entrainment produces a weakly stratified stagnant layer of fluid in the lee of the sill, which thickens and extends downstream. Eventually, fully established hydraulic flow is developed which is controlled at the sill crest where conditions change from subcritical to supercritical. When this control is established, the internal wave phase speed is less than the accelerated flow over the sill, and the internal wave becomes spatially locked to the crest of the sill. As the ebb tide continues, the internal waves are unable to propagate upstream against the rapid flow of the tidal current, and thus congregate in the lee of the sill. This results in a rapid depression of the thermocline in the lee of the sill. The stronger the tidal flow relative to the internal wave speed, the deeper the displacement of the thermocline. This results in an increase in the amplitude of the internal wave along with a decrease in the wavelength.

We found that the wavelength of the internal wave immediately downstream of the sill in East Sound was approximately 24 m along the westernmost edge of the Sound and increased to approximately 48 m on the eastern side of the Sound. The results of the two-stream reflectance model showed that the amplitude of the internal waves was the largest on the western side and the thermocline was also displaced almost 2 m from its upstream location. On the eastern side of the Sound, the internal wave did not induce a deepening of the thermocline.

We computed the phase speed at station B, based on the observed average density difference at stations B and C of 1.11 kg m^{-3} and an average density of

$1021.22 \text{ kg m}^{-3}$. At station B the water depth is approximately 10 m. Based on the upstream (station A) profile of temperature, we took the depth of the thermocline to be 2.5 m. Using these approximations the phase speed of the internal wave was computed using Equation 4.4 to be 0.14 m s^{-1} . If the sill is the generation site for the tidally induced internal wave, and supercritical conditions are established, then the internal waves are locked to the sill on the western side and not on the eastern side. In order for the internal waves to be locked to the sill, the phase speed of the internal wave must be less than the tidal flow.

At some E-W position along the sill, there is a transition from supercritical to subcritical conditions, past which the internal wave can be advected downstream with the tidal flow. Assuming that the change in density between the upper and lower layers is consistent across the sill, then the phase speed of the internal wave is only dependent on the water column depth. Figure 4.8 shows the water leaving radiance at 490 nm extracted along the most upstream bright line progressing from west to east, along with the bathymetry. The water leaving radiance is higher than 3.5 from the western shore to about 350 m to the east, and the water depth is less than 13 m. At 350 m from the western edge, the internal wave pattern bends southward, orienting nearly perpendicular to the axis of the sill. A sharp decrease in the radiance occurs from about 350 m to 550 m along the extracted line, as the water depth increases from about 13 m to 25.5 m. Taking the water column depth where the first bright reflecting lines turns southward as the hinge point or transition point where the conditions change from supercritical to subcritical, we

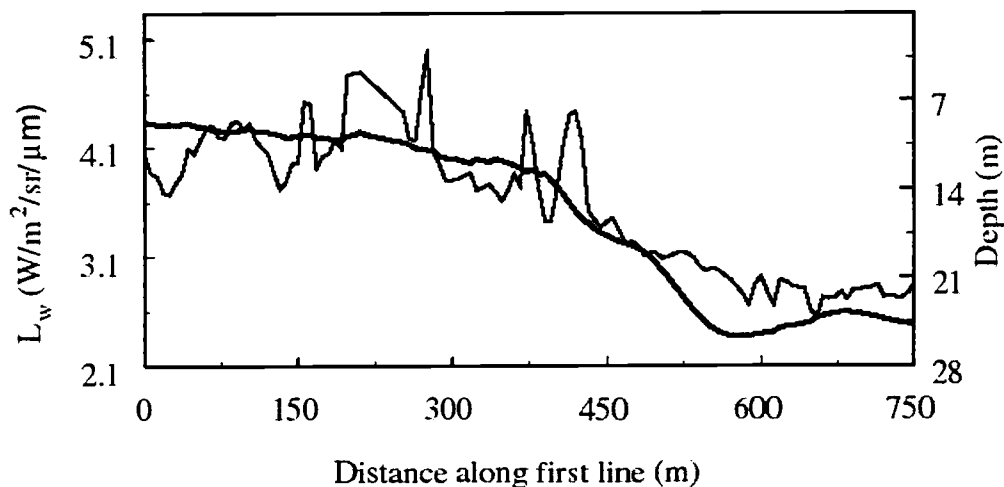


Figure 4.8. The water leaving radiance at 490 nm extracted along the most upstream bright reflecting line, versus distance from the western shore (solid line). Also plotted is the bathymetry along this line (thick line).

can compute the phase speed of the internal wave at this location. For supercritical conditions to exist west of this location, the flow velocities must be greater than the phase speed, while to the east of this point, the flow velocities must be less than the phase speed. Using the upstream water column depth of the thermocline as the height of the upper layer (2 m), and 13 m for the total water column depth at this location, the phase speed of the internal wave is then 0.13 m s^{-1} . Thus the flow velocities west of this location must be greater than 0.13 m s^{-1} , while to the east they must be lower.

Current velocities were measured using a 1500 and 300 kHz upward-looking bottom moored acoustic Doppler current profiler (ADCP) at a station on the sill and in the deep water channel. Unfortunately, the ADCP sampling was terminated on August 8, 1998. However, we can get an idea of the average flow

speeds during the strongest spring ebb tide by looking to the ADCP record on August 8th. Flow throughout most of the water column was mainly to the southeast during this period. Over the sill, flow velocities were greater than 15 cm s^{-1} except near the bottom, while in the deep-water channel east of the sill, the average flow velocities were less than 10 cm s^{-1} . Thus, the flow on the western side meets the criterion for supercritical conditions, which causes the internal wave to be locked to the sill where it appears as a lee or standing wave. The ADCP data from August 8 does not, however, provide confirming information about the transition point (subcritical to supercritical) along the sill.

4.8 SUMMARY

The lineal features of water leaving contrast as resolved in the 490 nm aircraft imagery was shown to be due to subsurface horizontal variability in the vertical stratification associated with an internal wave. The generating mechanism of the internal wave was likely associated with the tidal flow over the shallow partial sill near the opening of East Sound. Using a model based on the spatial contrast of the remote sensing reflectance of the imagery, we were able to estimate the amplitude of the internal wave. This estimate corresponded closely to the vertical variations in the thermocline observed in the in situ temperature profiles. The orientation of the internal wave train pattern was also important in providing a physical interpretation of the flow conditions necessary for the existence of the internal wave.

An important aspect of this analysis is the ability to provide spatial information on a subsurface physical feature from remotely sensed observations. In addition to providing information on the amplitude and the wavelength of the internal wave, we demonstrated how the results of the contrast model are useful in providing an interpretation of the physical dynamics of the internal wave.

4.9 REFERENCES

- Alpers, W. R., Theory of radar imaging of internal waves, *Nature*, 314, 245-247, 1985.
- Apel, J. R., H. M. Byrne, J. R. Proni, and R. L. Charnell, Observations of oceanic internal and surface waves from the Earth Resources Technology Satellite, *J. Geophys. Res.*, 80, 865-881, 1975.
- Barnard, A. H., W. S. Pegau, and J. R. V. Zaneveld, Global relationships of the inherent optical properties of the oceans, *J. Geophys. Res.*, 103, 24,955-24,968, 1998.
- da Silva, J. C. B., S. A. Ermakov, and I. S. Robinson, Role of surface films in ERS SAR signatures of internal waves on the shelf, 3, mode transitions, *J. Geophys. Res.*, 105, 24,089-24,104, 2000.
- Deksheniaks, M. M., T. R. Osborn, P. L. Donaghay, and J. M. Sullivan, Observations of general circulation patterns in East Sound, Washington, submitted to *Estuarine, Coastal and Shelf Science*, 2000.
- Farmer, D.M., & L. Armi, Stratified flow over topography: the role of small scale entrainment and mixing in flow establishment, *Proc. Roy. Soc., Mathematical Physical & Engineering Sciences*, London A, 455, 3221-3258, 1999a.
- Farmer, D.M., & L. Armi, The generation and trapping of internal solitary waves over topography, *Science*, 283, 188-190, 1999b.
- Gordon, H. R., Diffuse reflectance of the ocean: influence of nonuniform phytoplankton pigment profile, *Appl. Opt.*, 31, 2116-2129, 1992.

- Gordon, H. R. and W. R. McCluney, Estimation of the depth of sunlight penetration in the sea for remote sensing, *Appl. Opt.*, 14, 413-416, 1975.
- Gould, R.W., R.A. Arnone, and M. Sydor, Testing a new remote sensing reflectance algorithm to estimate absorption and scattering in case 2 waters, Ocean Optics 14 Conference Papers, Volume 2, Kailua-Kona, HI, November 10-13, 1998.
- Haltrin, V. I., Diffuse reflection coefficient of a stratified sea, *Appl. Opt.*, 38, 932-936, 1999.
- Hughes, B. A. and J. F. R. Gower, SAR imagery and surface truth comparisons of internal waves in Georgia Strait, British Columbia, Canada, *J. Geophys. Res.*, 88, 1809-1824, 1983.
- Kappus, M.E. and C.O. Davis, The challenges of using airborne imaging spectrometers over coastal waters, Ocean Optics XIV Conference Papers, Volume 2, Kailua-Kona, HI, November 10-13, 1998.
- Kitchen, J. C. and J. R. V. Zaneveld, On the noncorrelation of the vertical structure of light scattering and chlorophyll a in case 1 waters, *J. Geophys. Res.*, 95, 20,237-20,246, 1990.
- Maritorena, S., A. Morel, and B. Gentili, Diffuse reflectance of oceanic shallow waters: Influence of water depth and bottom albedo, *Limnol. Oceanogr.*, 39, 1689-1703, 1994.
- Mueller, J. L., SeaWiFS Algorithm for the diffuse attenuation coefficient $K(490)$ using water-leaving radiances at 490 and 555 nm, SeaWiFS Postlaunch Technical Report Series, NASA, 2000.
- Ouchi, K., N. R. Stapleton, and B. C. Barber, Multi-frequency SAR images of ship-generated internal waves, *Int. J. Remote Sensing*, 18(18), 3709-3718, 1997.
- Twardowski, M.S., J.M. Sullivan, P.L. Donaghay, and J.R.V. Zaneveld, Microscale quantification of the absorption by dissolved and particulate material in coastal waters with an ac-9, *J. Atmos. Ocean. Technol.*, 16(12), 691-707, 1999.
- Weidemann, A.D., D.J. Johnson, R.J. Holyer, W.S. Pegau, L.A. Jugan, and J.C. Sandidge, Remote sensing of internal solitons in the coastal ocean, *Remote Sensing of the Environment*, accepted, 2000.

- Witman, J. D., J. J. Leichter, S. J. Genocese, and D. A. Brooks, Pulsed phytoplankton supply to the rocky subtidal zone: Influence of internal waves, *Proc. Natl. Acad. Sci.*, 90, 1686-1690, 1993.
- Zaneveld, J. R. V., A. H. Barnard, W. S. Pegau and E. Boss, An investigation into the appropriate depth average of remotely sensed optical parameters, *Ocean Optics 14 Conference Papers, Volume 2, Kailua-Kona, HI, November 10-13, 1998.*
- Zaneveld, J. R. V., and W. S. Pegau, A model for the reflectance of thin layers, fronts, and internal waves and its inversion, *Oceanography*, 11, 44-47, 1998.

CHAPTER 5

THE DETERMINATION OF PAR LEVELS FROM ABSORPTION
COEFFICIENT PROFILES AT 490 nm

Andrew H. Barnard, J. Ronald V. Zaneveld, W. Scott Pegau, James L. Mueller,
Helmut Maske, Ruben Lara-Lara, Saul Alvarez-Borrego, Rafael Cervantes-Duarte,
Eduardo Valdez-Holguin

Published in *Ciencias Marinas*, 25(4), 487-507, 1999. Copyright by Ciencias
Marinas.

5.1 ABSTRACT

A model is presented that allows the prediction of percent photosynthetically available radiation (PAR) levels from measured profiles of the absorption coefficient at 490 nm in the Gulf of California. Percent PAR levels depend on the diffuse attenuation coefficients of the wavelengths that make up PAR, which in turn depend on the absorption coefficient. The emphasis is on developing a simple but robust model that can be used by researchers to plan deployments of photosynthesis experiments in the Gulf of California.

5.2 INTRODUCTION

In situ primary productivity measurements often require *a priori* knowledge of the structure of the underwater light field (i.e., percent light levels) for ^{14}C incubation bottle deployment. Typically, incubation bottles are deployed prior to sunrise in order to fully integrate over the light reaction cycle of photosynthesis. However, this poses a problem as the vertical structure of the solar photosynthetically available radiation (PAR) can only be measured during the daytime. Furthermore, radiometric measurements, such as PAR, are difficult to interpret near the surface due to waves, ship reflections, varying sky conditions, etc. It is thus useful to have a model for the prediction of percent PAR levels for the next daylight period using measurements made prior to sunrise.

Recent instrument development efforts [Moore *et al.*, 1992; Zaneveld *et al.*, 1992, 1994] have made the *in situ* measurement of the inherent optical properties (IOP) such as the spectral absorption and attenuation coefficients routine. As the IOP are not dependent on the ambient daylight field, and since these parameters can now be measured accurately *in situ*, it is of interest to determine if nighttime measurements of the IOP can be used to predict daytime PAR levels. The connection between the IOP and the apparent optical properties (AOP) is via the equation of radiative transfer, which solves for the radiance distribution as a function of depth when the absorption and scattering properties of the seawater as well as the incident radiance distribution are known. In this paper we develop a method for the prediction of PAR based on the vertical profile of a single parameter, the absorption coefficient at 490 nm. We show that with knowledge of the absorption profile at 490 nm, profiles of PAR relative to surface PAR can be calculated with a high degree of accuracy.

The waters of the Gulf of California have been shown to contain various biogeographic regions [Santamaría-del-Angel *et al.*, 1994] based on a long time-series analysis of ocean color imagery. It is thus an ideal location to investigate how the biological parameters and the IOP are related to the underwater light field. As such, we have been participating in an internationally coordinated measurement program to study the biological and optical properties in the Gulf of California over the past five years. One of the parameters that is being routinely measured during this work in the Gulf of California is ^{14}C estimates of primary production. In this

paper we examine the relationship between the absorption and PAR irradiance profiles and we derive a model to predict percent light levels based on the depth integrated absorption profile at a single wavelength. The intent of this work is to provide a method to estimate the daytime euphotic zone depth using nighttime measurements of the IOP in the Gulf of California.

5.3 METHODS

Three research cruises in the Gulf of California aboard the R/V *Francisco de Ulloa* were carried out during October and November 1996, March 1998 and November 1998. Stations were taken on the shelf near Guaymas, Sonora, in the central Gulf in deep water, on the sill just southwest of the central band of islands, and in the northwest section of the Gulf (Figure 5.1).

The spectral absorption coefficients were determined by means of a WET Labs ac-9 meter mounted on a free-falling profiling platform. The details of this platform are described in *Pegau et al.* [1999]. The ac-9 measures the absorption and the beam attenuation coefficients at nine wavelengths (412, 440, 488, 510, 532, 555, 650, 676 and 715 nm) at 6 Hz. The ac-9 was routinely calibrated in the field to a clean water standard. The absorption data were temperature and salinity corrected following the methods of *Pegau et al.* [1997] using CTD data collected simultaneously on the same profiling system. The absorption profile data were further corrected for scattering errors [*Zaneveld et al.*, 1994; *Moore et al.*, 1996].

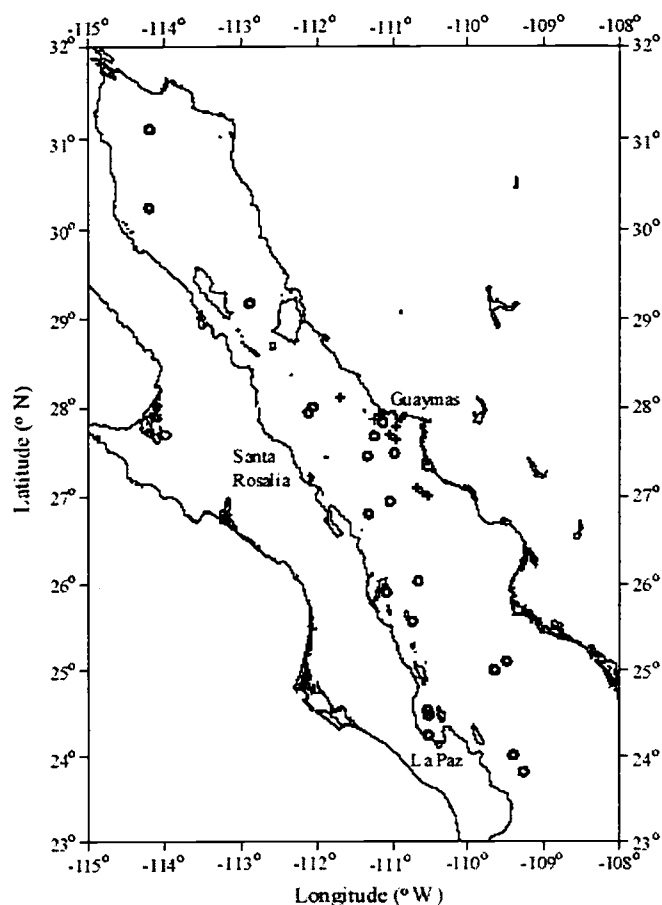


Figure 5.1. Sampling locations in the Gulf of California for the three cruises used in this study. Circles indicate the "clear" water stations and plus signs the "green" water locations.

The spectral absorption coefficients of pure water given by *Pope and Fry* [1997] were added to the measured wavelengths as the ac-9 measures absorption in reference to water.

Profiles of the spectral downwelling irradiance (E_d) were determined by means of a Satlantic SeaWiFS Profiling Multichannel Radiometer (SPMR) sensor. The SPMR sensor measures the downwelling irradiance at seven

wavelengths (412, 444, 490, 533, 556, 590 and 670 nm). PAR levels relative to the surface were obtained by spectral integration of the downwelling irradiance using the algorithm provided in the Satlantic software. In this analysis we extracted the above parameters at the 75, 50, 37, 20, 10, 5, 3 and 1 percent PAR levels relative to the surface. The absorption coefficients were determined using filters with a bandwidth of 10 nm and a central wavelength of 488 nm, whereas the irradiance was determined with a central wavelength of 490 nm. These are sufficiently similar, so that in this paper we use 490 nm for both data in the model development that follows.

Profiles of IOP and AOP were typically made at the same location within an hour of each other. A total of 30 nearly coincident profiles of the total absorption coefficient and irradiance were collected during these three cruises in the Gulf of California.

5.4 SEMI-ANALYTICAL MODEL AND RESULTS

The integration over solid angle of the equation of radiative transfer in plane parallel media without internal sources and inelastic scattering is given by Gershun's equation:

$$\frac{dE(\lambda, z)}{dz} = -a(\lambda, z)E_o(\lambda, z),$$

$$\frac{1}{E(\lambda, z)} \frac{dE(\lambda, z)}{dz} = -a(\lambda, z) \frac{E_o(\lambda, z)}{E(\lambda, z)} = -\frac{a(\lambda, z)}{\bar{\mu}(\lambda, z)}, \text{ where}$$

$$\bar{\mu}(\lambda, z) = \frac{E(\lambda, z)}{E_o(\lambda, z)} \text{ and } K(\lambda, z) = -\frac{dE(\lambda, z)}{E(\lambda, z)dz} = \frac{a(\lambda, z)}{\bar{\mu}(\lambda, z)} \quad (5.1)$$

where λ is wavelength in nm, $E(\lambda, z)$ is the net plane irradiance, $E_o(\lambda, z)$ is the scalar irradiance, $a(\lambda, z)$ is the total absorption coefficient, $K(\lambda, z)$ is the diffuse attenuation coefficient of the irradiance, and $\bar{\mu}(\lambda, z)$ is the average cosine of the light field [Jerlov, 1976]. The parameter that is typically measured by *in situ* radiometers such as the Satlantic SPMR is the downwelling irradiance, $E_d(\lambda, z)$. Using $E_d(\lambda, z)$ rather than $E(\lambda, z)$ is in error by approximately the irradiance reflectance ($R = E_u/E_d$), since $E = E_d(1-R)$. Since the reflectance R is typically a few percent, only a small error is made when using E_d rather than E in equation (5.1). We can thus state that for a given wavelength:

$$E_d(\lambda, z) \cong E_d(\lambda, 0) e^{-\int_0^z \frac{a(\lambda, z') dz'}{\bar{\mu}(\lambda, z')}} \quad (5.2)$$

For measurements of photosynthesis, it is useful to estimate the percent PAR as a fraction of the surface ($0'$) value, to provide an estimate of the amount of light available for photosynthesis as a function of depth. PAR is defined as the integration of irradiance in the visible region, i.e., 400 to 700 nm. Scalar irradiance (E_o) is the best measurement of the availability of light for photosynthesis, as phytoplankton cells can potentially collect photons regardless of the direction of the incoming light, assuming that the cells are randomly oriented. The percent PAR light levels can thus be obtained using:

$$\frac{E_o^{PAR}(z)}{E_o^{PAR}(0^-)} * 100\% = \frac{\int_{400}^{700} E_o(\lambda, z) d\lambda}{\int_{400}^{700} E_o(\lambda, 0^-) d\lambda} * 100\% \quad (5.3)$$

However, as noted above, the parameter that is typically measured is E_d . As scalar irradiance includes the light from all directions, by definition scalar irradiance must always be greater than the downwelling irradiance. The difference between the scalar and downwelling irradiance at a single wavelength is dependent on the ratio of the scattering and absorption coefficients. As the scattering to absorption ratio increases, the light field becomes more diffuse and the difference between the scalar and downwelling irradiance increases. In terms of PAR, Monte Carlo simulations by *Kirk* [1994] showed that the downwelling irradiance estimates of PAR are up to 20% lower than scalar PAR in clear oceanic waters. Thus, using downwelling irradiance instead of the scalar irradiance may underestimate the PAR optical depths by as much as 20% in equation (5.3).

From the above equations, we may define optical depth (τ_E) in the following manner:

$$E(\lambda, z) = E(\lambda, 0^-) e^{-\int_0^z K(\lambda, z') dz'} = E(\lambda, 0^-) e^{-\tau_E(\lambda, z)}, \text{ so that}$$

$$\tau_E(\lambda, z) = \int_0^z \frac{a(\lambda, z')}{\bar{\mu}(\lambda, z')} dz' = -\ln \frac{E_d(\lambda, z)}{E_d(\lambda, 0)} \quad (5.4)$$

for a single wavelength and

$$\tau_{PAR}(z) = -\ln \frac{E_d^{PAR}(z)}{E_d^{PAR}(0^-)} \quad (5.5)$$

for E_d^{PAR} . As we will demonstrate, it is possible to determine percent PAR levels from the downwelling irradiance measurements at a single wavelength. Here we use 490 nm since it is near the wavelength of maximum penetration into clear natural waters and is often used in remote sensing observations.

Figure 5.2 shows the relationship between $\tau_{PAR}(z)$ and $\tau_E(490, z)$ for the 30 profiles used in this study. Upon initial inspection of this relationship, we

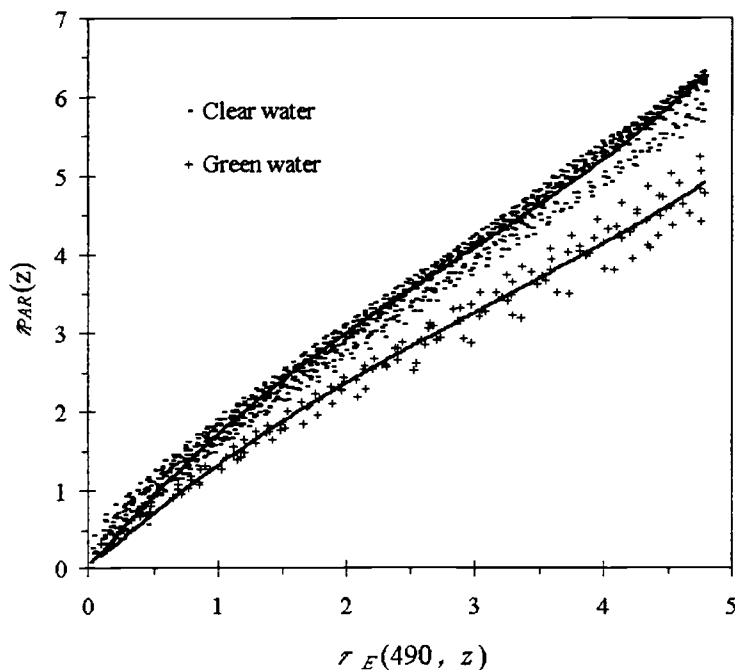


Figure 5.2. $\tau_{PAR}(z)$ versus $\tau_E(490, z)$ for the 30 profiles taken in the Gulf of California. "Clear" water stations are shown as dashes and plus symbols mark the "green" water stations. Also plotted are the 3rd order polynomial fits (see equations 5.6a and 5.6b).

hypothesized that there are two separate relationships for $\tau_{PAR}(z)$ and $\tau_E(490, z)$ based on the water type. Figure 5.3a shows the spectrum of downwelling irradiance transmittance from the surface to 10 m for the 30 profiles obtained in the Gulf of California. Two spectral shapes are apparent: one where the transmittance is relatively high and constant in the blue and green portions of the spectrum, and one where the transmittance is lower and where the transmittance is less in the blue than in the green portion of the spectrum. This is more clearly seen in figure 5.3b, where the spectrum of the irradiance transmittance in the

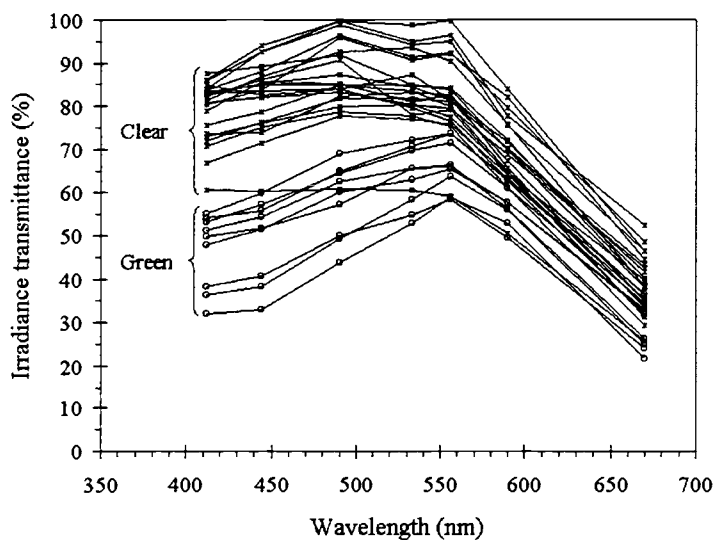


Figure 5.3a. Percent downwelling irradiance transmittance spectra from the surface to approximately 10 m for 30 profiles taken in the Gulf of California. Also shown are the spectra identified as "clear" and "green" water types.

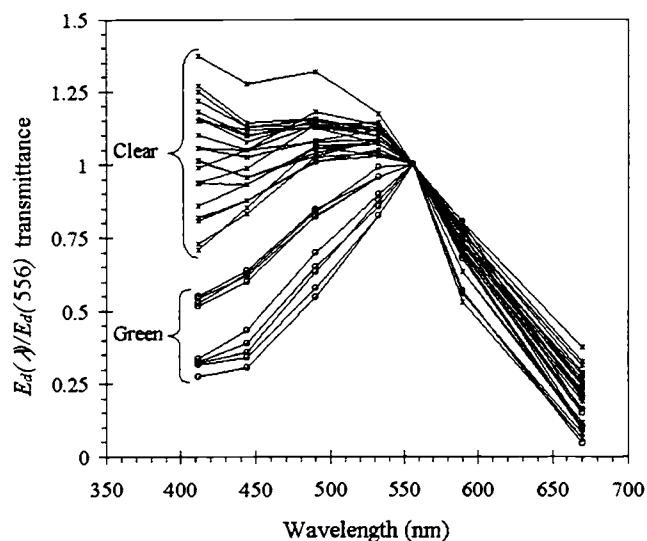


Figure 5.3b. Same as for figure 3a where the irradiance transmittance has been normalized by the 556 nm value.

surface layer has been normalized by the transmittance at 556 nm. These two spectral shapes are due to the composition of the materials in the water, with those that are relatively clear containing lower concentrations of absorbing materials.

The different water type classification can also be clearly seen in the surface average spectra of the absorption coefficient. Figure 5.4 shows the spectra of the total absorption coefficient for the 30 profiles averaged over the surface waters (1-10 m). The two different water types are clearly evident in the absorption spectra: one type with low absorption coefficients in the blue and green portions of the spectrum, and one type with higher values and more steeply sloped absorption spectra in the blue and green regions.

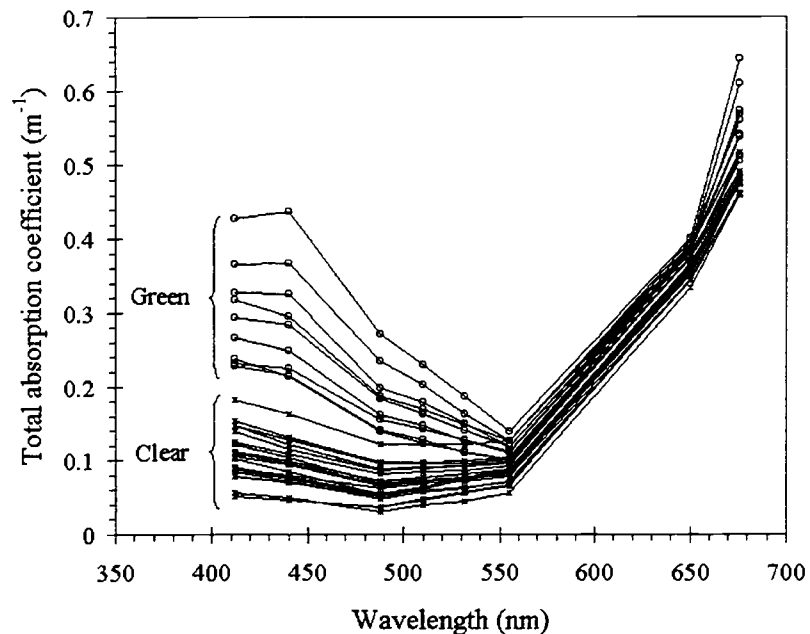


Figure 5.4. Total absorption coefficient spectra averaged over the first 10 m for the 30 profiles taken in the Gulf of California. Also shown are the spectra identified as "clear" and "green" water types.

Jerlov [1976] has classically defined these two water types as oceanic and coastal. Strong coastal upwelling events in the Gulf of California can advect coastal waters well into the center of the gulf, where clearer waters are usually present. As clear oceanic waters can often be found near the coast in the gulf, and as coastal water types can be advected well offshore to the center of the gulf, we chose to rename these two classifications based on the irradiance transmittance and absorption coefficient spectral shapes. Thus, we have chosen to describe *Jerlov's* oceanic water types as "clear" and the coastal water types as "green" to

better delineate water type based on a fundamental property as opposed to one based on location. Of the 30 profiles taken in the Gulf of California, 9 profiles were classified as "green" water type and 21 were "clear" water type. Most of the "green" stations are located near Guaymas and were collected during the 1996 cruise (see Figure 5.1).

Dividing our data set into "clear" and "green" water types, Figure 5.2 shows the relationship between $\tau_{PAR}(z)$ and $\tau_E(490, z)$ for each water type. *Zaneveld et al.* (1993) have examined the relationship between $\tau_{PAR}(z)$ and $\tau_E(490, z)$ for data obtained in the North Pacific. In that paper a piecewise linear relationship was deduced, based on three ranges of optical depth at 490 nm. They found that the rapid attenuation of the longer wavelengths (due to the strong absorption dependency of water in the red) causes an offset in the relationship of $\tau_{PAR}(z)$ and $\tau_E(490, z)$ when $\tau_E(490, z) > 0.2$. For a comparison with their data set we also fit our data to the same linear relationships (Table 5.1). We found a close correspondence between the relationships given by *Zaneveld et al.* [1993] and our "clear" water data set, the slopes being within 0.1 of each other. Note that the offsets of the "clear" water type are greater than those given by *Zaneveld et al.* [1993]. Offsets are due to the composition of the water itself, since more strongly absorbed wavelengths are removed in the upper layers and the weakly absorbed wavelengths penetrate further. The offset difference between our results and *Zaneveld et al.* [1993] indicates that the background concentrations are different between the two locations. Note that the "green" water relationship slopes are

Table 5.1. Piecewise linear relationship between $\tau_{PAR}(z)$ and $\tau_E(490, z)$ reproduced from Zaneveld *et al.* (1993) and for the 30 stations taken in the Gulf of California divided into the "clear" and "green" water types defined in the text.

	Slope	Y intercept	r^2
To 1 optical depth			
Zaneveld <i>et al.</i> (1993)	1.6243	0.0085	0.952
"Clear" water type	1.5285	0.2537	0.9119
"Green" water type	1.1069	0.2401	0.9604
From 1 to 2.3 optical depths			
Zaneveld <i>et al.</i> (1993)	1.2144	0.3175	0.935
"Clear" water type	1.1836	0.5666	0.9265
"Green" water type	0.9973	0.3421	0.9358
From 2.3 to 4.6 optical depths			
Zaneveld <i>et al.</i> (1993)	1.1676	0.3570	0.973
"Clear" water type	1.1622	0.5969	0.9656
"Green" water type	0.8998	0.5551	0.9001

very different from the "clear" water slopes and those given by Zaneveld *et al.* [1993]. This is a consequence of the different absorption spectra as shown in Figure 5.4. The higher absorption coefficient values for the "green" water types attenuate the downwelling light more rapidly, so that differences in the spectral shape of the absorption ultimately cause changes in the PAR integration of irradiance.

While the piecewise model for both the "clear" and "green" water cases fits well, we chose to model the relationship using a 3rd order polynomial with a zero intercept based on two factors. First, we expect that both $\tau_E(490, z)$ and $\tau_{PAR}(z)$ shown in Figure 5.2 should be equal to zero at $z = 0$, and thus that the

intercept should be zero; second, that the ratio of $\tau_E(490, z)$ to $\tau_{PAR}(z)$ is continuous with depth. Using a polynomial to model this relationship allows for the variation in the above relationship to change with depth. The models we used are:

$$\tau_{PAR}(z) = 0.039\tau_E^3(490, z) - 0.331\tau_E^2(490, z) + 2.003\tau_E(490, z) \quad (5.6a)$$

for the "clear" water case and

$$\tau_{PAR}(z) = 0.022\tau_E^3(490, z) - 0.206\tau_E^2(490, z) + 1.506\tau_E(490, z) \quad (5.6b)$$

for the "green" water case. Compared to the piecewise model, the polynomial fit is improved with $r^2 = 0.991$ and 0.982 for the "clear" and "green" models, respectively.

If we apply the mean value theorem to equation (5.4), we see that:

$$\tau_E(\lambda, z) = \frac{1}{\bar{\mu}(\lambda, \zeta)} \int_0^z a(\lambda, z') dz' \quad (5.7)$$

where ζ is some value of z' where $0 \leq z' \leq z$. If we form the "absorption optical depth", τ_a , where

$$\tau_a(\lambda, z) = \int_0^z a(\lambda, z') dz' \quad (5.8)$$

one can readily see that the ratio of $\tau_E(\lambda, z)$ and $\tau_a(\lambda, z)$ will be $[\bar{\mu}(\lambda, \zeta)]^{-1}$. Figure 5.5 shows the relationship between $\tau_E(490, z)$ and $\tau_a(490, z)$ for the 30 profiles in the Gulf of California. Much of the variation in the relationship is due to changes in the average cosine, $\bar{\mu}(490, \zeta)$. However, the figure indicates that optical depth

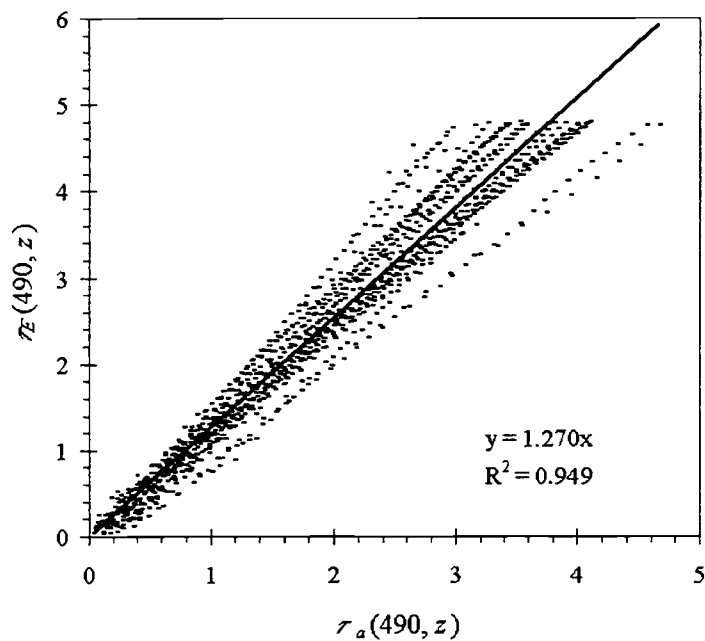


Figure 5.5. $\tau_E(490, z)$ versus $\tau_a(490, z)$ for the 30 profiles taken in the Gulf of California, with the linear regression shown.

can be predicted well from the integrated profiles of absorption at 490 nm using the linear regression:

$$\tau_E(490, z) = 1.270\tau_a(490, z) \quad (5.9)$$

with $r^2 = 0.949$ and standard error = 0.382. Note that the deviation from the regression increases with increasing optical depth. As optical depth is an integration over depth, the deviations, due to variations in the average cosine, increase with depth. Because $\bar{\mu}(490, z)$ has a small range in the vertical [Gordon *et al.*, 1993], it can be argued that the depth dependence of $\bar{\mu}(490, z)$ can be

folded into a functional relationship of $\tau_{PAR}(z)$ and $\tau_a(490, z)$ via $\tau_E(490, z)$.

This should entail little loss of accuracy and avoids the complication of modeling $\bar{\mu}(490, z)$ in stratified media when the input light field (sky conditions) is not known. Also, note that there is no need to delineate between "clear" and "green" water types as we are dealing with a single wavelength.

Since we have shown excellent relationships between $\tau_E(490, z)$ and $\tau_a(490, z)$, on the one hand, and between $\tau_{PAR}(z)$ and $\tau_E(490, z)$ on the other, one would also expect a good relationship between $\tau_{PAR}(z)$ and $\tau_a(490, z)$.

Substituting equation (5.9) into equations (5.6a) and (5.6b), we can estimate the PAR optical depth from the $\tau_a(490, z)$ profile using:

$$\tau_{PAR}(z) = 0.080\tau_a^3(490, z) - 0.534\tau_a^2(490, z) + 2.544\tau_a(490, z) \quad (5.10a)$$

for the "clear" water case, and

$$\tau_{PAR}(z) = 0.045\tau_a^3(490, z) - 0.332\tau_a^2(490, z) + 1.913\tau_a(490, z) \quad (5.10b)$$

for the "green" water case. The euphotic depth for which $\tau_{PAR}(z) = 4.6$ and other PAR depths can then be readily determined from $\tau_a(490, z)$ values, as in Table 5.2.

Figure 5.6 shows the modeled versus the measured $\tau_{PAR}(z)$ relationship for the 30 stations in the Gulf of California, combining both "clear" and "green" water models. In general, the absorption model for predicting the vertical profile of $\tau_{PAR}(z)$ does well when compared with percent PAR depths derived from the

Table 5.2. Percent PAR light level using the "clear" and "green" models (see equations 5.10a and 5.10b) from the integrated absorption coefficient at 490 nm profile. Also shown is the standard error using the models to predict the various percent PAR light level depths.

% PAR light level	$\tau_{PAR}(z)$	"Clear" $\tau_a(490, z)$	"Green" $\tau_a(490, z)$	Standard error (m)
75	0.29	0.105	0.143	0.704
50	0.69	0.275	0.375	1.499
37	1.0	0.420	0.567	1.756
20	1.61	0.25	0.982	2.007
10	2.3	1.119	1.517	2.292
5	3.00	1.576	2.127	2.495
3	3.51	1.945	2.592	3.159
1	4.60	2.745	3.543	4.150

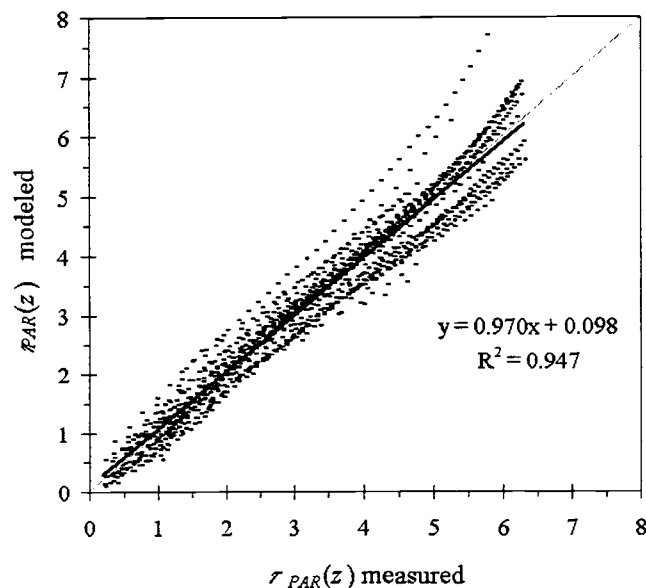


Figure 5.6. Measured $\tau_{PAR}(z)$ determined from *in situ* radiance profiles versus the modeled $\tau_{PAR}(z)$ determined from the *in situ* absorption coefficient at 490 nm profiles for the 30 stations in the Gulf of California (see equations 5.10a and 5.10b), with the linear regression shown.

Satlantic irradiance observations with an $r^2 = 0.947$ and standard error = 0.368.

Table 5.2 shows the percent PAR levels and the corresponding $\tau_a(490, z)$ values derived using the above process. In practice, one could thus integrate the observed absorption coefficient measurement at 490 nm with depth, as in equation (5.8), and use the derived $\tau_a(490, z)$ versus depth plot to obtain the percent PAR depths using Table 5.2.

Using the 75, 50, 37, 20, 10, 5, 3 and 1 percent light levels as inputs to the model, we extracted the depths at which these light levels are estimated by the model and compared them to the measured light level depths. Figure 5.7 shows the comparison of the modeled and measured depth of the above light levels, for both the "clear" and "green" water type models. The models do well, with a general tendency to predict the light levels slightly deeper than the measured depths ($r^2 = 0.965$, slope = 1.027, intercept = 0.534). The standard error using all light levels is 2.425 m. Table 5.2 shows the standard error between the modeled and measured depths at the individual light levels used in this study. The error increases with decreasing light level. This is likely due to the combined effects of variations in the average cosine and the difficulty in measuring the surface PAR value accurately. However, note that the error in predicting the lowest light level (1%), i.e., the euphotic depth, is only 4.15 m. Thus, this model is useful in predicting the PAR light levels to within approximately 4.15 m in the Gulf of California.

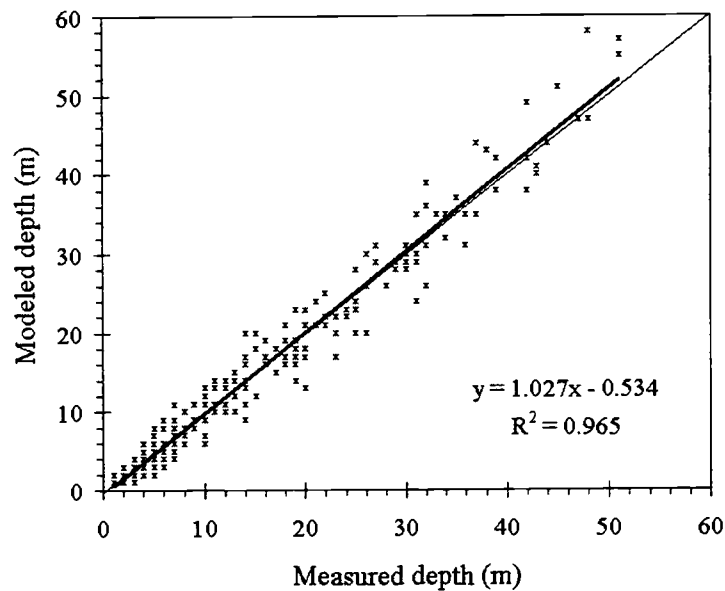


Figure 5.7. The 75, 50, 37, 20, 10, 5, 3 and 1 percent PAR light level depths estimated from *in situ* spectral irradiance profiles versus the corresponding depths estimated from the absorption optical depth model for the 30 profiles in the Gulf of California.

5.5 DISCUSSION

The most straightforward method of determining the percent PAR light levels is to integrate the spectral downwelling irradiance profile. The error in estimating these depths is due solely to using the downwelling irradiance rather than the scalar irradiance. In highly scattering waters, this error can lead to underestimates in the PAR irradiance as much as 20% [Kirk, 1994]. However, in practice, *in situ* measurements of the downwelling irradiance profiles are

frequently complicated by factors such as varying sky conditions, ship shadowing, surface waves, sun angle, etc., especially at the surface. Thus, determinations of the percent PAR light levels relative to the surface value can often be difficult to accurately estimate using *in situ* irradiance measurements. Furthermore, these measurements can only be made during the daylight hours, and thus are not useful for the researcher who is faced with choosing the depths at which to place ^{14}C primary production incubation bottles prior to sunrise. As the inherent optical properties are not dependent on the underwater light field, it is of interest to examine whether these measurements made at night can be useful in predicting daytime percent PAR light levels.

It has been shown by *Zaneveld et al.* [1993] and in this paper that a good relationship exists between $\tau_{\text{PAR}}(z)$ and $\tau_E(490, z)$ depending on the water type (Figure 5.6). Based on the spectrum of the surface downwelling irradiance transmittance and the spectral absorption coefficient, two water types were identified in this paper, corresponding to Jerlov's [1976] classical definition of oceanic and coastal water types. In this paper we have chosen to rename these water types based on the spectrum of the absorption coefficient rather than location, as "clear" water (low absorption coefficients in the blue and green wavelengths) and "green" water (high absorption values and steeply sloped in the blue and green regions). Instead of modeling the relationships between $\tau_{\text{PAR}}(z)$ and $\tau_E(490, z)$ using a piecewise linear fit as done by *Zaneveld et al.* [1993], we chose to use a polynomial function. The polynomial model used in this paper has

the advantage over that given by *Zaneveld et al.* [1993] in that it allows the $\tau_{PAR}(z)$ versus $\tau_E(490, z)$ relationship to be continuous throughout the profile without loss of accuracy. It is interesting to note that the piecewise linear relationships from data taken in the North Pacific are similar to those found in the Gulf of California (Table 5.1), indicating that the "clear" water model given in this study may be generally applicable to other open ocean environments.

Although the relationship between $\tau_E(490, z)$ and $\tau_\alpha(490, z)$ is expected to vary from profile to profile due to the changes in the vertical structure in $[\bar{\mu}(\lambda, z)]^{-1}$, we find that this relationship is remarkably consistent when considering the 30 profiles in the Gulf of California (Figure 5.5). The result of using a simple linear relationship to model $\tau_E(490, z)$ from $\tau_\alpha(490, z)$ is that one assumes that there is some average $[\bar{\mu}(\lambda, \zeta)]^{-1}$ in these 30 profiles. We find that by assuming that there is some average $[\bar{\mu}(\lambda, \zeta)]^{-1}$, there is very little loss of accuracy in using the $\tau_E(490, z)$ versus $\tau_\alpha(490, z)$ linear relationship to predict $\tau_{PAR}(z)$.

Expected daytime $\tau_{PAR}(z)$ depths versus observed depths are very good (Figure 5.6), considering that the irradiance data was usually collected up to one hour before or after the absorption profile. Any discrepancies could thus be ascribed to spatial variations alone. Other sources of error exist, of course, in all approximations. Instrumental errors are also present. Considering these, the results are surprisingly good. This indicates that the expected daytime euphotic

depth and other light levels can be determined with sufficient accuracy to allow appropriate depths to be determined at night, so that samples can be obtained for ^{14}C primary productivity incubations during the following daylight period. The model presented here shows that percent PAR light level depths can be predicted accurately from the IOP using empirical relationships between $\tau_a(490, z)$ and $\tau_{\text{PAR}}(z)$ derived from observations at a single wavelength in the Gulf of California.

The applicability of these models to other regions is dependent on the composition of the absorbing and scattering materials in the water. The simple "clear" and "green" water classifications identified in this paper may not encompass all of the water types found in the oceans. However, we find a close similarity between our "clear" water model in the Gulf of California and the models in the North Pacific given by *Zaneveld et al.* [1993]. We also find that the variations in the average cosine profile may be encompassed in the $\tau_E(490, z)$ and $\tau_a(490, z)$ relationship with little loss of accuracy. Further investigations are necessary in order to determine how applicable these models are to other environments.

5.6 REFERENCES

- Gordon, H. R., K. Dong, and W. Gong, Radiative transfer in the ocean: computations relating to the asymptotic and near-asymptotic daylight field, *Appl. Opt.*, 32(9), 1606-1619, 1993.
- Jerlov, N. G, *Marine Optics*, Elsevier, New York, p. 89, 1976.

- Kirk, J. T. O., *Light and Photosynthesis in Aquatic Ecosystems*, Cambridge University Press, New York, p. 151-153, 1994.
- Moore, C., J. R.V. Zaneveld, and J. C. Kitchen, Preliminary results from an *in situ* spectral absorption meter, Ocean Optics 11, *Proc. SPIE Int. Soc. Opt. Eng.*, 1750, 330-337, 1992.
- Moore, C., E. J. Bruce, W. S. Pegau, and A. D. Weidemann, WET Labs ac-9: Field calibration protocol, deployment techniques, data processing, and design improvements, Ocean Optics 13, *Proc. SPIE Int. Soc. Opt. Eng.*, 2963, 725-730, 1996.
- Pegau, W. S., J. R. V. Zaneveld, and A. H. Barnard, Inherent optical properties in the Gulf of California, *Ciencias Marinas*, 24(4), 469-485, 1999.
- Pegau, W. S., D. Gray, and J. R. V. Zaneveld, Absorption of visible and near-infrared light in water: The dependence on temperature and salinity, *Appl. Opt.*, 36, 6035-6046, 1997.
- Pope, R. M. and E. S. Fry, Absorption spectrum (380-700 nm) of pure water. II. Integrating cavity measurements, *Appl. Opt.*, 26, 8710-8723.
- Santanmaria-del-Angel, E., S. Alvarez-Borrego, and F. E. Muller-Karger, Gulf of California biogeographic regions based on coastal zone color scanner imagery, *J. Geophys. Res.*, 99,7411-7421, 1994.
- Zaneveld, J. R.V., J. C. Kitchen, A. Bricaud and C. Moore, Analysis of *in situ* spectral absorption meter data, Ocean Optics 11, *Proc. SPIE Int. Soc. Opt. Eng.*, 1750, 180-186, 1992.
- Zaneveld, J. R. V., J. C. Kitchen, and J. L. Mueller, The vertical structure of productivity and its vertical integration as derived from remotely sensed observations, *Limnol. Oceanogr.*, 38, 1384-1393, 1993.
- Zaneveld, J. R. V., J. C. Kitchen, and C. Moore, Scattering error correction of reflecting tube absorption meters, Ocean Optics 12, *Proc. SPIE Int. Soc. Opt. Eng.*, 2258, 44-55, 1994.

CHAPTER 6

6. GENERAL CONCLUSIONS

The research in this thesis was motivated by the desire to apply in situ observations of the inherent optical properties (IOP) to critical questions in optical oceanography. The research questions addressed in this thesis focussed on several key processes including the spectral variability in the IOP of the oceans, the relationships between the IOP and the remotely sensed reflectance, the influence of vertical structure in the IOP on the remotely sensed reflectance, and the indirect assessment of light attenuation from the vertical structure of the absorption coefficient. It is the author's hope that this thesis has demonstrated the importance of high spectral and spatial resolution IOP measurements in addressing questions relating to the optical properties and the physical and biogeochemical processes of the oceans.

As much of the work in this thesis was obtained with recently developed instrumentation, it was critical to show that the measurements obtained were unbiased in both time and space. Therefore, a major aspect of the work contained in chapter two focused on the issue of the precision of the WET Labs, Inc. ac-9 meter. We used a large database of the IOP data collected by the ac-9 to show that when the proper maintenance and calibration procedures are performed, the measurements are precise over large time and space scales and thus are suitable for

studies of radiative transfer. Using this data set we investigated the spectral relationships of the dissolved, particulate and total absorption coefficient, the particulate scattering coefficient, and the total beam attenuation coefficient. The results of this research showed that over a diversity of oceanic regimes, there are fundamental spectral relationships in the individual IOP components. In the context of remote sensing applications, these first-order relationships can provide a set of basis vectors that can be used in inversion algorithms when no a priori information on the optical properties is available.

In order to use the IOP measurements provided by the ac-9 meter in studies of radiative transfer, it is also important to show that closure between the radiometric and IOP measurements can be achieved. The issue of instrument closure based on the relationship between the remote sensing reflectance and the IOP was examined in chapter three. In this work, we provided a model that greatly minimized the influence of the angular nature of the underwater light field and the backscattering coefficient on the remotely sensed reflectance. In sampling situations where instrument calibrations are limited, this model provides a method to verify that the radiometric and IOP measurements are consistent. Using a data set of 70 radiometric and IOP profiles as inputs to the model, we demonstrated closure between the IOP and radiometric measurements to within instrument accuracy. This work also showed that if the spectral dependence of the absorption coefficient can be modeled accurately, then it is possible to invert the spectral remote sensing reflectance to obtain the magnitude of the spectral absorption

coefficient. By using simple linear models to describe the spectral relationship of the absorption coefficient (as shown in chapter two), we found that the predictability of this model was similar to other band-ratio algorithms. These results emphasize the need to better understand the causes of the variability in the spectral shape and magnitude of the absorption coefficient.

This thesis also used in situ measurements of the IOP to address two practical problems in oceanography, the remote assessment of physical structure and the indirect assessment of light attenuation. We examined the first problem by relating the horizontal variability in the vertical structure in optical properties to the remotely sensing reflectance, and used this relationship to elucidate subsurface features using visible remote sensing imagery. Based on a two-stream radiative transfer approximation of the reflectance [*Zaneveld and Pegau, 1998*], we developed an simple two-layer remotely sensed reflectance model to predict the amplitude of an internal wave using the spatial variability observed in aircraft imagery. The predicted amplitudes corresponded closely to the vertical variations in the thermocline observed in the in situ temperature profiles. We also showed how the spatial orientation of the internal wave train pattern was important in providing a physical interpretation of the flow conditions necessary for the existence of the internal wave.

We addressed the indirect assessment of vertical light attenuation by using absorption coefficient measurements which are independent of the light field, to predict daytime light levels. In chapter five, we developed an empirical model to

predict the photosynthetically available radiation (PAR) light levels from an absorption coefficient profile at a single wavelength (490 nm). The goal of this research was to provide a method to predict the PAR light level depths from nighttime observations to aid primary productivity experiments planned for early morning. In this work we examined the relationship between the optical depth (τ) of PAR and downwelling irradiance at 490 nm obtained during recent research cruises in the Gulf of California. Based on the irradiance transmittance and total absorption spectra, the data set was divided into two types, a green (high absorption, low irradiance transmittance) data set and a clear (low absorption, high irradiance transmittance) data set. A third order polynomial fit of the optical depth of the downwelling irradiance at 490 nm was used to predict the optical depth of PAR for each water type. By applying the mean value theorem to Gershun's equation, we derived an optical depth based on the total absorption coefficient profile at 490 nm. A simple linear regression model of the optical depth based on the absorption coefficient profile was used predict the optical depth of irradiance at 490 nm. Using these relationships, we showed that the depth of various PAR irradiance light levels could be predicted within 4 m from a single profile of the absorption coefficient at 490 nm.

With the advent of new ocean color sensors, the development of bio-optical algorithms to obtain information on the IOP from ocean color satellite measurements has increased over the past 8 years. Further quantification of the influence of the spatial and temporal variability in the IOP on the remotely sensed

radiance is crucial, particularly as we move from coarse-resolution open-ocean color sensors to those that resolve smaller spatial scales. Small-scale variations in spectral water leaving radiance can only be understood by quantifying the individual contributions of small scale variability in both the water column and boundary layer IOP, and further by exploring the physical and biochemical processes that determine those variations. These effects are especially important in case II environments, where the small-scale horizontal variability is likely to be as large as the vertical variability (see chapter four). Thus, quantification of the causes and effects of the spatial coherence in the upward radiance distribution will yield more accurate algorithms for determining the IOP from remotely sensed ocean color and lead to an increased understanding of the physical and biogeochemical processes occurring in the ocean environment.

BIBLIOGRAPHY

- Ahn, Y., A. Bricaud, and A. Morel, Light backscattering efficiency and related properties of some phytoplankters, *Deep-Sea Res.*, 39, 1835-1855, 1992.
- Alpers, W. R., Theory of radar imaging of internal waves, *Nature*, 314, 245-247, 1985.
- Apel, J. R., H. M. Byrne, J. R. Proni, and R. L. Charnell, Observations of oceanic internal and surface waves from the Earth Resources Technology Satellite, *J. Geophys. Res.*, 80, 865-881, 1975.
- Barnard, A. H., W. S. Pegau, and J. R. V. Zaneveld, Global relationships of the inherent optical properties of the ocean, *J. Geophys. Res.*, 103, 24,955-24,968, 1998.
- Barnard, A. H., J. R. V. Zaneveld, and W. S. Pegau, In situ determination of the remotely sensed reflectance and the absorption coefficient: closure and inversion, *Applied Optics*, 38, 5108-5117, 1999.
- Barnard, A. H., J. R. V. Zaneveld, W. S. Pegau, J. L. Mueller, H. Maske, R. Lara-Lara, S. Alvarez-Borrego, R. Cervantes-Duarte, and E. Valdez-Holguin, The determination of PAR levels from absorption coefficient profiles at 490 nm, *Ciencias Marinas*, 25(4), 487-507, 1999.
- Blough, N. V., O. C. Zafiriou, and J. Bonilla, Optical absorption spectra of waters from the Orinoco River outflow: Terrestrial input of colored organic matter to the Caribbean, *J. Geophys. Res.*, 98, 2271-2278, 1993.
- Bricaud, A., A. Morel, and L. Prieur, Absorption by dissolved organic matter of the sea (yellow substance) in the UV and visible domains, *Limnol. Oceanogr.*, 26, 43-53, 1981.
- Bricaud, A., A. Morel, and L. Prieur, Optical efficiency factors of some phytoplankters, *Limnol. Oceanogr.*, 28, 816-832, 1983.
- Bricaud, A., and D. Stramski, Spectral absorption coefficients of living phytoplankton and nonalgal biogenous matter: A comparison between the Peru upwelling area and the Sargasso Sea, *Limnol. Oceanogr.*, 33, 562-582, 1990.

- Bricaud, A., C. Roesler, and J. R. V. Zaneveld, *In situ* methods for measuring the inherent optical properties of ocean waters, *Limnol. Oceanogr.*, 40, 393-410, 1995a.
- Bricaud, A., M. Babin, A. Morel, and H. Claustre, Variability in the chlorophyll-specific absorption coefficients of natural phytoplankton: Analysis and parameterization, *J. Geophys. Res.*, 100, 13,321-13,332, 1995b.
- Campbell, J. W. and W. E. Esaias, Basis for spectral curvature algorithms in remote sensing of chlorophyll, *Appl. Opt.*, 22, 1084-1093, 1983.
- Carder, K. L., G. R. Harvey, and P. B. Ortner, Marine humic and fulvic acids: Their effects on remote sensing of ocean chlorophyll, *Limnol. Oceanogr.*, 34, 68-81, 1989.
- Carder, K. L., S. K. Hawes, K. S. Baker, R. C. Smith, R. G. Steward, and B. G. Mitchell, Reflectance model for quantifying chlorophyll *a* in the presence of productivity degradation products, *J. Geophys. Res.*, 96, 20,599-20,611, 1991.
- da Silva, J. C. B., S. A. Ermakov, and I. S. Robinson, Role of surface films in ERS SAR signatures of internal waves on the shelf, 3, mode transitions, *J. Geophys. Res.*, 105, 24,089-24,104, 2000.
- Deksheniaks, M. M., T. R. Osborn, P. L. Donaghay, and J. M. Sullivan, Observations of general circulation patterns in East Sound, Washington, submitted to *Estuarine, Coastal and Shelf Science*, 2000.
- Farmer, D.M., & L. Armi, Stratified flow over topography: the role of small scale entrainment and mixing in flow establishment, *Proc. Roy. Soc., Mathematical Physical & Engineering Sciences*, London A, 455, 3221-3258, 1999.
- Farmer, D.M., & L. Armi, The generation and trapping of internal solitary waves over topography, *Science*, 283, 188-190, 1999.
- Garver, S. A. and D. A. Siegel, Inherent optical property inversion of ocean color spectra and its biogeochemical interpretation. 1. Time series from the Sargasso Sea, *J. Geophys. Res.*, 102, 18,607-18,625, 1997.
- Gordon, H. R., Absorption and scattering estimates from irradiance measurements: Monte Carlo simulations, *Limnol. Oceanogr.*, 36, 769-777, 1991.

- Gordon, H. R., Diffuse reflectance of the ocean: influence of nonuniform phytoplankton pigment profile, *Appl. Opt.*, 31, 2116-2129, 1992.
- Gordon, H. R., O. B. Brown, R. H. Evans, J. W. Brown, R. C. Smith, K. S. Baker, and D. K. Clark, A semianalytic radiance model of ocean color, *J. Geophys. Res.*, 93, 10,909-10,924, 1988.
- Gordon, H. R., K. Dong, and W. Gong, Radiative transfer in the ocean: computations relating to the asymptotic and near-asymptotic daylight field, *Appl. Opt.*, 32(9), 1606-1619, 1993.
- Gordon, H. R. and W. R. McCluney, Estimation of the depth of sunlight penetration in the sea for remote sensing, *Appl. Opt.*, 14, 413-416, 1975.
- Gould, R.W., R.A. Arnone, and M. Sydor, Testing a new remote sensing reflectance algorithm to estimate absorption and scattering in case 2 waters, Ocean Optics 14 Conference Papers, Volume 2, Kailua-Kona, HI, November 10-13, 1998.
- Haltrin, V. I., Diffuse reflection coefficient of a stratified sea, *Appl. Opt.*, 38, 932-936, 1999.
- Hoepffner, N., and S. Sathyendranath, Determination of the major groups of phytoplankton pigments from the absorption spectra of total particulate matter, *J. Geophys. Res.*, 98, 22,789-22,803, 1993.
- Hoge, F. E. and P. E. Lyon, Satellite retrieval of inherent optical properties by linear matrix inversion of oceanic radiance models: An analysis of model and radiance measurement errors, *J. Geophys. Res.*, 101, 16,631-16,648, 1996.
- Hoge, F. E., A. Vodacek, and N. V. Blough, Inherent optical properties of the ocean: Retrieval of the absorption coefficient of chromophoric dissolved organic matter from fluorescence measurements, *Limnol. Oceanogr.*, 38, 1394-1402, 1993.
- Hughes, B. A. and J. F. R. Gower, SAR imagery and surface truth comparisons of internal waves in Georgia Strait, British Columbia, Canada, *J. Geophys. Res.*, 88, 1809-1824, 1983.
- Jerlov, N. G, *Marine Optics*, Elsevier, New York, p. 89, 1976.

- Kappus, M.E. and C.O. Davis, The challenges of using airborne imaging spectrometers over coastal waters, Ocean Optics 14 Conference Papers, Volume 2, Kailua-Kona, HI, November 10-13, 1998.
- Kirk, J. T. O., Estimation of the absorption and the scattering coefficients of natural waters by use of the underwater irradiance measurements, *Appl. Opt.*, 33, 3276-3278, 1994.
- Kirk, J. T. O., *Light and Photosynthesis in Aquatic Ecosystems*, Cambridge University Press, New York, p. 151-153, 1994.
- Kishino, M., M. Takahashi, N. Okami, and S. Ichimura, Estimation of the spectral absorption coefficients of phytoplankton in the sea, *Bull. Mar. Sci.*, 37, 634-642, 1985.
- Kitchen, J. C. and J. R. V. Zaneveld, On the noncorrelation of the vertical structure of light scattering and chlorophyll a in case 1 waters, *J. Geophys. Res.*, 95, 20,237-20,246, 1990.
- Lee, Z. P., K. L. Carder, S. K. Hawes, R. G. Steward, T. G. Peacock, and C. O. Davis, Model for the interpretation of hyperspectral remote-sensing reflectance, *Appl. Opt.*, 33, 5721-5732, 1994.
- Lee, Z. P., K. L. Carder, T. G. Peacock, C. O. Davis, and J. L. Mueller, A method to derive ocean absorption coefficients from remote-sensing reflectance, *Appl. Opt.*, 35, 453-462, 1996.
- Lee, Z. P., K. L. Carder, R. G. Steward, T. G. Peacock, C. O. Davis, and J. S. Patch, An empirical algorithm for light absorption by ocean water based on color, *J. Geophys. Res.*, 103, 27,967-27,978, 1998.
- Maffione, R. A. and D. R. Dana, Instruments and methods for measuring the backward-scattering coefficient of ocean waters, *Appl. Opt.*, 36, 6057-6067, 1997.
- Maritorena, S., A. Morel, and B. Gentili, Diffuse reflectance of oceanic shallow waters: Influence of water depth and bottom albedo, *Limnol. Oceanogr.*, 39, 1689-1703, 1994.
- Mitchell, B. G., Algorithms for determining the absorption coefficient of aquatic particulates using quantitative filter technique (QFT), Ocean Optics 10, *Proc. SPIE Int. Soc. Opt. Eng.*, 1302, 137-148, 1990.

- Mitchell, B. G. and D. A. Kiefer, Chlorophyll *a* specific absorption and fluorescence excitation spectra for light limited phytoplankton, *Deep-Sea Res., Part A*, 35, 639-664, 1988.
- Mitchell, B. G. and D. A. Kiefer, Variability in pigment specific particulate fluorescence and absorption spectra in the northeastern Pacific Ocean, *Deep-Sea Res., Part A*, 35, 665-689, 1988.
- Moore, C., J. R. V. Zaneveld, and J. C. Kitchen, Preliminary results from an *in situ* spectral absorption meter, *Ocean Optics* 11, *Proc. SPIE Int. Soc. Opt. Eng.*, 1750, 330-337, 1992.
- Moore, C., E. J. Bruce, W. S. Pegau, and A. D. Weidemann, WET Labs ac-9: Field calibration protocol, deployment techniques, data processing, and design improvements, *Ocean Optics* 13, *Proc. SPIE Int. Soc. Opt. Eng.*, 2963, 725-730, 1996.
- Morel, A., Optical properties of pure water and pure sea water, in *Optical Aspects of Oceanography*, N.G. Jerlov and E.S. Nielsen, eds., Academic Press, New York, pp. 1-24, 1974.
- Morel, A. and L. Prieur, Analysis of variations in ocean color, *Limnol. Oceanogr.*, 22, 709-722, 1977.
- Morel, A., Optical modeling of the upper ocean in relation to its biogenous matter content (case I waters), *J. Geophys. Res.*, 93, 10,749-10,768, 1988.
- Morel, A. and B. Gentili, Diffuse reflectance of oceanic waters. II. Bidirectional aspects, *Appl. Opt.*, 32, 6864-6879, 1993.
- Morel, A., K. J. Voss, and B. Gentili, Bidirectional reflectance of oceanic waters: a comparison of modeled and measured upward radiance fields, *J. Geophys. Res.*, 100, 13,143-13,151, 1995.
- Morel, A. and B. Gentili, Diffuse reflectance of oceanic waters. III. Implication of bidirectionality for the remote sensing problem, *Appl. Opt.*, 35, 4850-4862, 1996.
- Morrow, J. H., W. S. Chamberlin, and D. A. Kiefer, A two-component description of spectral absorption by marine particles, *Limnol. Oceanogr.*, 34, 1500-1509, 1989.

- Mueller, J.L., SeaWiFS Algorithm for the diffuse attenuation coefficient K(490) using water-leaving radiances at 490 and 555 nm, SeaWiFS Postlaunch Technical Report Series, NASA, 2000.
- Ouchi, K., N. R. Stapleton, and B. C. Barber, Multi-frequency SAR images of ship-generated internal waves, *Int. J. Remote Sensing*, 18(18), 3709-3718, 1997.
- Pak, H., D. A. Kiefer, and J. C. Kitchen, Meridional variations in the concentration of chlorophyll and micro-particles in the North Pacific Ocean, *Deep-Sea Res., Part A*, 35, 1151-1171, 1988.
- Pegau, W. S., D. Gray, and J. R. V. Zaneveld, Absorption of visible and near-infrared light in water: the dependence on temperature and salinity, *Appl. Opt.*, 36, 6035-6046, 1997.
- Pegau, W. S., J. S. Cleveland, W. Doss, C. D. Kennedy, R. A. Maffione, J. L. Mueller, R. Stone, C. C. Trees, A. D. Weidemann, W. H. Wells, and J. R. V. Zaneveld, A comparison of methods for the measurement of the absorption coefficient in natural waters, *J. Geophys. Res.*, 100, 13,201-13,220, 1995.
- Pegau, W. S., J. R. V. Zaneveld, and A. H. Barnard, Inherent optical properties in the Gulf of California, *Ciencias Marinas*, 24(4), 469-485, 1999.
- Pegau, W. S., J. R. V. Zaneveld, and K. J. Voss, Toward closure of the inherent optical properties of natural waters, *J. Geophys. Res.*, 100, 13,193-13,199, 1995.
- Petzold, T. and R. Austin, An underwater transmissometer for ocean survey work, in Underwater photo-optical instrument applications, *Proc. SPIE Int. Soc. Eng.*, 12, 133-137, 1968.
- Pope, R. M. and E. S. Fry, Absorption spectrum (380-700 nm) of pure water. II. Integrating cavity measurements, *Appl. Opt.*, 36, 8710-8723, 1997.
- Preisendorfer, R. W., *Hydrologic Optics*, vol. 6, U.S. Department of Commer., Washington, D. C., 1976.
- Prieur, L., and S. Sathyendranath, An optical classification of coastal and oceanic waters based on the specific absorption curves of phytoplankton pigments, dissolved organic matter, and other particulate materials, *Limnol. Oceanogr.*, 26, 671-687, 1981.

- Roesler, C. S. and M. J. Perry, In situ phytoplankton absorption, fluorescence emission, and particulate backscattering spectra determined from reflectance, *J. Geophys. Res.*, 100, 13,279-13,294, 1995.
- Roesler, C. S. and J. R. V. Zaneveld, High resolution vertical profiles of spectral absorption, attenuation, and scattering coefficients in highly stratified waters, *Ocean Optics* 12, *Proc. SPIE Int. Soc. Opt. Eng.*, 2258, 309-318, 1994.
- Roesler, C. S., M. J. Perry, and K. L. Carder, Modeling *in situ* phytoplankton absorption from total absorption spectra in productive inland marine waters, *Limnol. Oceanogr.*, 34, 1510-1523, 1989.
- Santanmaria-del-Angel, E., S. Alvarez-Borrego, and F. E. Muller-Karger, Gulf of California biogeographic regions based on coastal zone color scanner imagery, *J. Geophys. Res.*, 99,7411-7421, 1994.
- Sathyendranath, S., L. Lazzara, and L. Prieur, Variations in the spectral values of the specific absorption of phytoplankton, *Limnol. Oceanogr.*, 32, 403-415, 1989.
- Smith, R. C. and K. S. Baker, Optical properties of the clearest natural waters, *Appl. Opt.*, 20, 177-184, 1981.
- Stramski, D. and D. A. Kiefer, Light scattering by microorganisms in the open ocean, *Prog. Oceanogr.*, 28, 343-383, 1991.
- Trüper, H. G. and C. S. Yentsch, Use of glass fiber filters for the rapid preparation of *in vivo* absorption spectra of photosynthetic bacteria, *J. Bacteriol.*, 94, 1255-1256, 1967.
- Twardowski, M. S., J. M. Sullivan, P. L. Donaghay, and J. R. V. Zaneveld, Quantification of the micro- to finescale *in situ* chromophoric DOM absorption and total absorption in coastal waters with an ac-9, *J. Atmo. Ocean. Tech.*, 16, 691-707, 1999.
- Weidemann, A.D., D.J. Johnson, R.J. Holyer, W.S. Pegau, L.A. Jugan, and J.C. Sandidge, Remote sensing of internal solitons in the coastal ocean, *Remote Sensing of the Environment*, accepted, 2000.
- Witman, J. D., J. J. Leichter, S. J. Genocese, and D. A. Brooks, Pulsed phytoplankton supply to the rocky subtidal zone: Influence of internal waves, *Proc. Natl. Acad. Sci.*, 90, 1686-1690, 1993.

- Voss, K. J., A spectral model of the beam attenuation coefficient in the ocean and coastal areas, *Limnol. Oceanogr.*, 37, 501-509, 1992.
- Zaneveld, J. R. V., Remotely sensed reflectance and its dependence on vertical structure: a theoretical derivation, *Appl. Opt.*, 21, 4146-4150, 1982.
- Zaneveld, J. R. V., An asymptotic closure theory for irradiance in the sea and its inversion to obtain the inherent optical properties, *Limnol. Oceanogr.*, 34, 1442-1452, 1989.
- Zaneveld, J. R. V., A theoretical derivation of the dependence of the remotely sensed reflectance of the ocean on the inherent optical properties, *J. Geophys. Res.*, 100, 13,135-13,142, 1995.
- Zaneveld, J. R. V., A. H. Barnard, W. S. Pegau and E. Boss, An investigation into the appropriate depth average of remotely sensed optical parameters, Ocean Optics 14 Conference Papers, Volume 2, Kailua-Kona, HI, November 10-13, 1998.
- Zaneveld, J. R. V., and J. C. Kitchen, The variation in the inherent optical properties of phytoplankton near an absorption peak as determined by various models of cell structure, *J. Geophys. Res.*, 100, 13,309-13,320, 1995.
- Zaneveld, J. R. V., J. C. Kitchen, A. Bricaud, and C. Moore, Analysis of *in situ* spectral absorption meter data, Ocean Optics 11, *Proc. SPIE Int. Soc. Opt. Eng.*, 1750, 180-186, 1992.
- Zaneveld, J. R. V., J. C. Kitchen, and C. C. Moore, Scattering error correction of reflecting tube absorption meters, Ocean Optics 13, *Proc. SPIE Int. Soc. Opt. Eng.*, 2258, 44-55, 1994.
- Zaneveld, J. R. V., J. C. Kitchen, and J. L. Mueller, The vertical structure of productivity and its vertical integration as derived from remotely sensed observations, *Limnol. Oceanogr.*, 38, 1384-1393, 1993.
- Zaneveld, J. R. V. and W. S. Pegau, A model for the reflectance of thin layers, fronts, and internal waves and its inversion, *Oceanography*, 11, 44-47, 1998.